UNIVERSIDADE FEDERAL DE JUIZ DE FORA

INSTITUTO DE CIÊNCIAS EXATAS / FACULDADE DE ENGENHARIA

PROGRAMA DE PÓS-GRADUAÇÃO EM MODELAGEM COMPUTACIONAL

Gabriel Brandão de Miranda

Improved Parameter Estimation Procedures and Uncertainty Quantification of Foam in Porous Media

Juiz de Fora

2025

Ficha catalográfica elaborada através do Modelo Latex do CDC da UFJF
com os dados fornecidos pelo(a) autor(a)

de Miranda, Gabriel.
Improved Parameter Estimation Procedures and Uncertainty Quantification of Foam in Porous Media / Gabriel Brandão de Miranda. – 2025.
149 f. : il.

Orientador: Bernardo Martins Rocha
Coorientadores: Rodrigo Weber dos Santos & Grigori Chapiro
Tese (Doutorado) – Universidade Federal de Juiz de Fora, Instituto de Ciências Exatas / Faculdade de Engenharia. Programa de Pós-Graduação em Modelagem Computacional, 2025.

1. Quantificação de Incertezas. 2. Espumas. 3. Permeabilidade Relativa. 4. Escoamento trifásico. 5. Inferência Bayesiana. I. Rocha, Bernardo, orient. II. Título.

Gabriel Brandão de Miranda

Improved Parameter Estimation Procedures and Uncertainty Quantification of Foam in Porous Media

Tese apresentada ao Programa de Pós-Graduação em Modelagem Computacional da Universidade Federal de Juiz de Fora, como requisito parcial para obtenção do grau de Doutor em Modelagem Computacional.

Orientador: Bernardo Martins Rocha

Coorientadores: Rodrigo Weber dos Santos & Grigori Chapiro

Juiz de Fora

2025

Gabriel Brandão de Miranda

Improved Parameter Estimation Procedures and Uncertainty Quantification of Foam in Porous Media

Tese apresentada ao Programa de Pós-graduação em Modelagem Computacional da Universidade Federal de Juiz de Fora como requisito parcial à obtenção do título de Doutor em Modelagem Computacional. Área de concentração: Modelagem Computacional.

Aprovada em 29 de setembro de 2025.

BANCA EXAMINADORA

Prof. Dr. Bernardo Martins Rocha - Orientador
Universidade Federal de Juiz de Fora

Prof. Dr. Rodrigo Weber dos Santos - Coorientador
Universidade Federal de Juiz de Fora

Prof. Dr. Grigori Chapiro - Coorientador
Universidade Federal de Juiz de Fora

Prof. Dr. Marcelo Lobosco
Universidade Federal de Juiz de Fora

Dr. Pavel Zenon Sejas Paz
Universidade Federal de Juiz de Fora

Prof. Dr. Marcio Rentes Borges
Laboratório Nacional de Computação Científica

Prof. Dr. Denis Voskov
TU Delft, Países Baixos

Juiz de Fora, 26/09/2025.

Documento assinado eletronicamente por **Bernardo Martins Rocha**, **Professor(a)**, em 10/11/2025, às 10:52, conforme horário oficial de Brasília, com fundamento no § 3º do art. 4º do Decreto nº 10.543, de 13 de novembro de 2020.

Documento assinado eletronicamente por **Marcio Rentes Borges**, **Usuário Externo**, em 10/11/2025, às 10:56, conforme horário oficial de Brasília, com fundamento no § 3º do art. 4º do Decreto nº 10.543, de 13 de novembro de 2020.

Documento assinado eletronicamente por **Grigori Chapiro**, **Professor(a)**, em 10/11/2025, às 11:12, conforme horário oficial de Brasília, com fundamento no § 3º do art. 4º do Decreto nº 10.543, de 13 de novembro de 2020.

Documento assinado eletronicamente por **Pavel Zenon Sejas Paz**, **Usuário Externo**, em 10/11/2025, às 11:23, conforme horário oficial de Brasília, com fundamento no § 3º do art. 4º do Decreto nº 10.543, de 13 de novembro de 2020.

Documento assinado eletronicamente por **Marcelo Lobosco**, **Professor(a)**, em 10/11/2025, às 11:35, conforme horário oficial de Brasília, com fundamento no § 3º do art. 4º do Decreto nº 10.543, de 13 de novembro de 2020.

Documento assinado eletronicamente por **Rodrigo Weber dos Santos**, **Professor(a)**, em 10/11/2025, às 15:00, conforme horário oficial de Brasília, com fundamento no § 3º do art. 4º do Decreto nº 10.543, de 13 de novembro de 2020.

Documento assinado eletronicamente por **Denis Viktorovich Voskov**, **Usuário Externo**, em 10/11/2025, às 15:10, conforme horário oficial de Brasília, com fundamento no § 3º do art. 4º do Decreto nº 10.543, de 13 de novembro de 2020.

A autenticidade deste documento pode ser conferida no Portal do SEI-Ufjf (www2.ufjf.br/SEI) através do ícone Conferência de Documentos, informando o código verificador **2644647** e o código CRC **8963F554**.

ACKNOWLEDGEMENTS

I want to thank my family for their unwavering support, especially my mother, whose constant presence and unconditional love have been invaluable to me throughout my life.

I also thank the Graduate Program professors for their knowledge and patience, as well as all my supervisors for their guidance and support. A special thank you to my primary supervisor for his dedication and patience in listening to my ideas and helping me find the best path. Finally, I would like to thank my lab colleagues for their partnership and friendship.

I thankfully acknowledge the committee members, who greatly contributed to this work through their valuable insights and constructive feedback. Their expertise and thoughtful suggestions were crucial in refining this research and elevating its quality.

I gratefully acknowledge support from Shell Brasil through the project "Avançando na modelagem matemática e computacional para apoiar a implementação da tecnologia 'Foam-assisted WAG' em reservatórios do Pré-sal" (ANP 23518-4) at UFJF and the strategic importance of the support given by ANP through the R&D levy regulation.

I am grateful to the Coordenação de Aperfeiçoamento de Pessoal de Nível Superior (CAPES) for the partial financial support provided through a scholarship, which was essential for the completion of this research.

“Uncertainty is an uncomfortable position. But certainty is an absurd one.”

- VOLTAIRE.

ABSTRACT

Characterization of foam flow in subsurface formations requires protocols capable of managing experimental uncertainties. Existing approaches for mathematical model calibration treat foam properties and multiphase flow functions as independent systems, introducing potential errors in simulations. When considering enhanced oil recovery (EOR), this limitation is compounded by the absence of systematic calibration protocols for water-oil-gas-foam systems, resulting in models with reduced predictive capability.

This thesis presents an uncertainty quantification (UQ) protocol for parameter estimation in foam flow models. The protocol integrates Bayesian inference, surrogate modeling, parametric identifiability assessment, uncertainty propagation, and sensitivity analysis, applied to two-phase and three-phase flow scenarios relevant to foam applications in subsurface modeling.

Three computational contributions constitute the core of the thesis. First, joint estimation of foam and relative permeability parameters in water-gas systems reveals interdependencies masked by sequential calibration procedures. Polynomial chaos-based emulators enable efficient uncertainty propagation, quantifying predictive reliability bounds. Second, extension of the protocol to three-phase systems is performed considering oil-foam destabilization mechanisms. Numerical experiments establish data sufficiency criteria for parameter identifiability and demonstrate that conventional experimental protocols often yield ill-conditioned inverse problems, potentially leading to erroneous predictions. Third, a reformulated mobility reduction factor expression eliminates the need for relative permeability assumptions, connecting mathematical and experimental interpretations of foam resistance and reducing epistemic uncertainties in calibration. Foam quality scan data for different surfactant concentrations validate the approach and delineate requirements for parameter identifiability.

Systematic application of UQ techniques establishes quantitative criteria for parameter estimation reliability and experimental design in foam-enhanced recovery. Inverse UQ defines experimental requirements and model limitations to prevent incorrect characterizations, while forward UQ propagates parametric uncertainties to simulations, connecting laboratory measurements to field-scale predictions. This probabilistic approach incorporates uncertainties in industrial application planning, identifying risks overlooked by traditional deterministic methods and enabling risk-aware decision-making.

Keywords: Uncertainty Quantification. Foam. Relative Permeability. Three-phase flow. Bayesian Inference.

RESUMO

A caracterização do fluxo de espuma em meios porosos exige protocolos capazes de lidar com incertezas experimentais. Abordagens na literatura para calibração de modelos matemáticos tratam propriedades da espuma e funções de fluxo multifásico como sistemas independentes, introduzindo erros potenciais nas simulações. Ao considerar recuperação avançada de petróleo (EOR), esta limitação é agravada pela ausência de protocolos sistemáticos para calibração em sistemas água-óleo-gás-espuma, resultando em modelos com capacidade preditiva reduzida.

Esta tese apresenta um protocolo de quantificação de incertezas (UQ) para estimativa paramétrica em modelos de fluxo de espuma. O protocolo integra inferência Bayesiana, modelagem substituta, avaliação de identificabilidade paramétrica e análise de sensibilidade, aplicado a cenários de fluxo bifásico e trifásico em modelagem de reservatórios.

Três contribuições computacionais constituem o núcleo da tese. Primeiro, a estimativa conjunta de parâmetros da espuma e da permeabilidade relativa em sistemas água-gás revela interdependências mascaradas por procedimentos sequenciais de calibração. Emuladores baseados em caos polinomial viabilizam a propagação eficiente de incertezas, quantificando limites de confiabilidade preditiva. Segundo, a extensão do protocolo para sistemas trifásicos é realizada considerando mecanismos de desestabilização da espuma por óleo. Experimentos numéricos estabelecem critérios de suficiência de dados para identificabilidade paramétrica e demonstram que protocolos experimentais convencionais geram problemas inversos mal-condicionados, que acarretam previsões potencialmente errôneas. Terceiro, uma expressão reformulada para o fator de redução de mobilidade elimina a necessidade de hipóteses sobre permeabilidade relativa, conectando interpretações matemáticas e experimentais de resistência da espuma e reduzindo incertezas epistêmicas na calibração. Dados de varredura de qualidade da espuma para diferentes concentrações de surfactante validam a abordagem e delimitam requisitos para identificabilidade paramétrica.

A aplicação sistemática de técnicas de UQ estabelece critérios quantitativos para a confiabilidade da estimativa paramétrica e do projeto experimental em recuperação avançada com espuma. A UQ inversa define requisitos experimentais e limitações do modelo para prevenir caracterizações incorretas, enquanto a UQ direta propaga incertezas paramétricas para simulações, conectando medições laboratoriais a predições em escala de campo. Esta abordagem probabilística incorpora incertezas no planejamento de aplicações industriais, identificando riscos negligenciados por métodos determinísticos tradicionais e viabilizando a tomada de decisão informada por risco.

Palavras-chave: Quantificação de Incertezas. Espumas. Permeabilidade Relativa. Escoamento trifásico Inferência Bayesiana.

LIST OF FIGURES

LIST OF TABLES

LIST OF ABBREVIATIONS AND ACRONYMS

CCUS	Carbon Capture Usage and Storage
CMG	Computer Modelling Group
CO_2	Carbon Dioxide
DE	Differential Evolution
EOR	Enhanced Oil Recovery
FAWAG	Foam-Assisted Water-Alternating-Gas
FOSSIL	FOam diSplacement SImuLator
GP	Gaussian Process
HMC	Hamiltonian Monte Carlo
MCMC	Markov Chain Monte Carlo
MRF	Mobility Reduction Factor
NUTS	No-U-Turn Sampler
OOIP	Original Oil in Place
PCE	Polynomial Chaos Expansion
PDE	Partial Differential Equations
PDF	Probability Density Function
PV	Pore Volume
QoI	Quantity of Interest
SA	Sensitivity Analysis
SAG	Surfactant-Alternating-Gas
STARS	Steam, Thermal, and Advanced Processes Reservoir Simulator
OpenFOAM	Open source Field Operation And Manipulation
UQ	Uncertainty Quantification
UQTOPUS	Uncertainty Quantification Toolbox for OpenFOAM and Python Unified Simulation
UTCHEM	University of Texas Chemical Compositional Reservoir Simulation Model
WAG	Water-Alternating-Gas

CONTENTS

1 INTRODUCTION

This chapter presents the general context, a brief review of the literature, the motivations, the objectives, and the organization of this work.

1.1 CONTEXT

Subsurface engineering processes that rely on gas injection may face effectiveness issues due to the high mobility of the gas phase. The mobility contrast with resident liquids triggers viscous fingering and gravity override, which in turn yield early breakthrough and poor sweep efficiency. Rock heterogeneity further channels flow through high-permeability pathways, leaving low-permeability zones unswept (Lake, 1989; Shafiei et al., 2024). Foam, a liquid phase trapping dispersed gas stabilized by surfactant, provides a mechanism to mitigate these effects (Tripathi et al., 2024; Wang et al., 2025). It replaces continuous gas with discontinuous bubbles, providing mobility control to divert gas into previously bypassed zones, enhancing volumetric sweep efficiency, and ultimately improving the performance of subsurface operations (Kovscek and Radke, 1994).

Foam flow in porous media has proven useful across a range of applications, including fertilizer delivery in agriculture (Shojaei et al., 2022), soil remediation and groundwater protection in environmental engineering (Rossen, 1996; del Campo Estrada, 2014), and energy production, ranging from well stimulation to enhance permeability or mitigate near-wellbore damage (Cheng et al., 2001; Faroughi et al., 2018; Okere et al., 2020), to geothermal energy extraction (Harshini et al., 2024), and enhanced oil recovery (EOR) (Lake, 1989; Rossen, 1996; Zhang et al., 2009).

Foam-assisted techniques have been recognized as a method for enhancing oil recovery since the 1960s (Fried, 1960; Bernard and Holm, 1964). They provide more uniform displacement of oil within the reservoir, which is especially advantageous in heterogeneous formations, where traditional methods may struggle to achieve desired recovery rates (Sæle et al., 2022). Foam mobilizes residual oil trapped in porous media by altering fluid flow paths, which mitigates issues such as gas channeling, viscous fingering, and gravity override (Rossen, 1996; Zhang et al., 2009; Lotfollahi et al., 2016; Hematpur et al., 2018). Laboratory studies and field applications show that foam-assisted EOR techniques offer improved oil recovery rates compared to conventional gas injection methods (Moradi-Araghi et al., 1997; Zhang et al., 2009; Sæle et al., 2022; Alcorn et al., 2022; Vieira et al., 2024).

In addition to improving recovery rates, the use of foams in EOR can lead to substantial economic benefits by optimizing resource utilization and extending the productive life of mature oil fields. Also, foam's adaptability to reservoir conditions altering

the system, including as CO_2-based, nitrogen-based, and steam-based foams, enhances its applicability in EOR operations (Zhang et al., 2009). Foam flooding in reservoirs, named Foam-Assisted Water-Alternating-Gas (FAWAG), can involve both in situ and pre-generated foam approaches. For in situ foam generation, also named Surfactant-Alternating-Gas (SAG), a surfactant solution and gas are injected alternately into the reservoir, and the foam forms within the reservoir as the gas and surfactant solution mix. On the other hand, in some FAWAG applications, foam is generated at the surface (pre-generated) before being injected into the reservoir along with water and gas. This pre-generated foam approach allows for better control over the foam properties, such as bubble size and stability, before entering the reservoir (de Paula et al., 2024; Paula et al., 2022; Farajzadeh et al., 2015a; Afsharpoor et al., 2010; Li et al., 2010).

As global efforts to reduce atmospheric CO_2 levels intensify, Carbon Capture, Utilization, and Storage (CCUS) has emerged as an opportunity in climate change mitigation. The Sixth Assessment Report by the Intergovernmental Panel on Climate Change (IPCC) states that anthropogenic greenhouse gas emissions, particularly CO_2, are the primary cause of rising global temperatures. The projections indicate that CO_2 emissions are likely to continue increasing in the coming years before any decrease occurs. In this context, foam has attracted increasing attention to support carbon storage technologies and mitigate the impacts of ongoing emissions (Metz et al., 2005; Rognmo et al., 2019; Arias et al., 2021; Orujov et al., 2023; Bello et al., 2023a; Fritis et al., 2025). In this context, foamed gas may reduce the formation of preferential paths by diverting flow into less permeable zones of the formation, thereby addressing challenges in geological CO_2 sequestration and enhancing the efficiency and safety of long-term subsurface storage (Rognmo et al., 2019; Rossen et al., 2024). Therefore, foam-assisted CCUS operations for the oil industry offer a dual benefit of enhancing oil recovery and long-term CO_2 storage in geological formations simultaneously, which makes foam a promising solution in the near future (Rognmo et al., 2019; Orujov et al., 2023; Bello et al., 2023a; Rossen et al., 2024). Figure 1 illustrates the role of foam in EOR operations, where it increases sweep efficiency to enhance oil recovery and controls gas mobility to enable CO_2 sequestration.

The effectiveness of foam injection in EOR depends critically on understanding foam stability under reservoir conditions. Since foam strength depends on various factors such as surfactant concentration, foam quality, and reservoir conditions (Farajzadeh et al., 2015c; Kapetas et al., 2015; Hematpur et al., 2018), it leads to significant uncertainties in performance prediction for field applications. Additionally, foam stability is also influenced by the presence of oil, which alters its dynamics. The presence of oil can significantly impact foam stability through complex physico-chemical interactions, causing foam to lose its strength and reducing its effectiveness in EOR. In this thesis, we investigate the `STARS` (CMG, 2019) foam model in porous media, which incorporates the previously discussed effects of oil on foam.

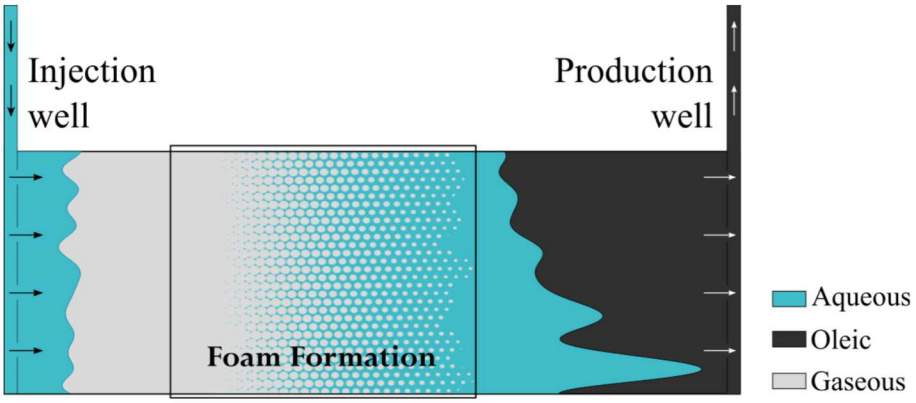

Figure 1 – Schematic representation of cyclical injection of gas and water/surfactant for foam formation. The diagram contrasts the preferential pathways of water fronts (blue) with the more uniform displacement achieved by foamed gas (gray bubbles within a blue network), illustrating foam's dual advantage in enhancing sweep efficiency for oil (black) recovery and blocking gas paths to facilitate CO_2 storage.

1.2 MOTIVATION

Previous studies on uncertainty in foam flow models have focused on analyzing foam properties, neglecting the interactions between important component models that describe the underlying physics of the phenomenon, such as the relative permeabilities (Valdez et al., 2020, 2021; de Miranda et al., 2022b,a). Furthermore, despite its importance for the industry, dedicated uncertainty quantification (UQ) and parameter estimation frameworks for three-phase foam flow are underexplored. Moreover, the limited interpretability of implicit-texture models, non-standardized definitions for foam strength evaluation (Adebayo, 2021), and uncertainty about the minimal experimental data needed for robust parameter estimation pose challenges for calibrating foam simulators for EOR planning.

Inaccurate parameter estimation can lead to significant issues in predictions, causing them to differ substantially from actual field observations, which ultimately impact operational decisions (Ma et al., 2013; Ding et al., 2020a). Without accurate methods for parameter estimation, each additional modeling step can increase uncertainty in the predictions. Moreover, the absence of an uncertainty model complicates risk assessment in foam injection projects, as subsurface modeling often involves complexities that a single best estimate cannot fully encompass (Cushman and Tartakovsky, 2016). Together, these challenges may hinder the adoption of foam-assisted recovery techniques, despite their recognized potential.

Previous studies on foam quality scans using experimental data identified strategies that significantly reduced uncertainties in estimating foam parameters related to only the dry-out effects under the assumption of known relative permeability (de Miranda et al., 2022b; Valdez et al., 2021). However, extending such approaches to other factors that affect foam strength (e.g., surfactant concentration or oil saturation) or to additional model

components (e.g., relative permeability) proved challenging. A single foam quality scan experiment did not provide sufficient data to characterize foam and relative permeability parameters (Ribeiro et al., 2024). The recognition of these experimental difficulties, together with the lack of comprehensive three-phase foam flow studies with a detailed parameter estimation approach (Tang et al., 2016, 2019c; Lyu et al., 2021b), motivates the present investigation. Our focus is on developing improved parameter estimation methods and uncertainty quantification frameworks for multiphase foam systems, which may ultimately support the design of more robust experimental protocols.

1.3 OBJECTIVES

This thesis is based on a comprehensive uncertainty quantification framework for foam flow modeling in porous media, improved and applied with a focus on the implicit-texture foam model. It is designed to address discrepancies between experimental data and predictions from mathematical models.

The primary objective of this thesis is to evaluate how the novel parameter estimation methods proposed herein, developed to consider different effects on foam strength, influence predicted foam performance through uncertainty quantification and sensitivity analysis, thereby guiding potential improvements in experimental design. To achieve this goal, the study addresses the following specific objectives:

- Quantify the influence of experimental uncertainties on calibrating foam flow simulators, particularly the simultaneous determination of relative permeabilities and foam model parameters.
- Extend and validate an uncertainty-quantification and global sensitivity-analysis framework for three-phase foam flow.
- Propose and evaluate enhanced parameter estimation considering three-phase flow in porous media with foam to ensure measurements align with model representations.

1.4 ORGANIZATION

Figure 2 outlines the organization of this thesis, beginning with the introduction and theoretical foundation (Chapters 1–2), followed by three self-contained but interconnected research chapters (Chapters 3–5), and concluding with the synthesis of findings (Chapter 6). Solid arrows illustrate the sequence of reading between chapters, whereas dashed arrows indicate conceptual relationships: the path from Chapter 3 to Chapter 4 incorporates foam-oil interactions; the path from Chapter 3 to Chapter 5 incorporates surfactant effects and removes dependence on relative permeability estimation. Both extensions use the mobility reduction factor to isolate these additional effects.

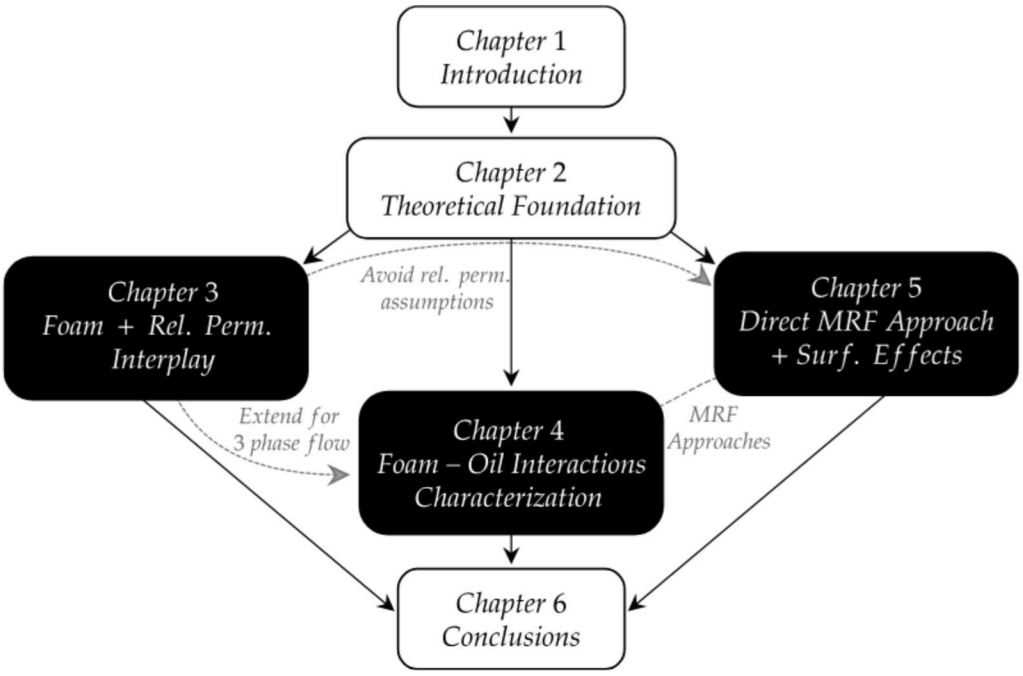

Figure 2 – Thesis structure from introduction (Chapter 1) through theoretical foundation (Chapter 2) to three self-contained chapters (Chapters 3-5, shown in black blocks), concluding with synthesis (Chapter 6). Solid arrows indicate methodological flow; dashed arrows represent conceptual connections between the paper-based chapters.

A brief overview of the content of the following chapters is provided below to orient the reader. Chapter 2 presents the governing equations for multiphase flow in porous media, the implicit-texture model for foam, and the uncertainty quantification framework used throughout, including Bayesian inference, polynomial chaos expansion for surrogate modeling, and Sobol sensitivity analysis, together with its computational implementation. Chapter 3 applies this framework to two-phase foam flow, examining the coupling between relative permeability and foam parameters through steady-state and transient simulations. Chapter 4 extends the analysis to three-phase systems, incorporating foam–oil interactions and identifying experimental data needs for reliable parameter estimation. Chapter 5 introduces a pressure-drop–based method for estimating foam parameters without prior relative permeability characterization, improving identifiability and assessing the influence of surfactant concentration. Chapter 6 synthesizes the main findings and offers recommendations for future research and industrial application of the framework.

2 THEORETICAL FOUNDATION

This chapter covers foam flow modeling in porous media, focusing on the implicit-texture model that adjusts gas mobility using a mobility reduction factor. The chapter also briefly outlines methods for uncertainty quantification and sensitivity analysis, combining Bayesian inference and probabilistic modeling to assess the impact of uncertain parameters.

2.1 MULTI-PHASE FLOW IN POROUS MEDIA

The general mathematical model for the three-phase flow of water, oil, and gas in a porous medium is formulated based on mass conservation, coupled with an extension of Darcy's law for each phase. For incompressible and immiscible phases, ignoring gravity and capillary pressures, the problem is governed by the following equations, where S_α represents saturation of the α phase, and u_α denotes the phase velocity:

$$\phi \frac{\partial S_\alpha}{\partial t} + \nabla \cdot u_\alpha = 0, \quad \text{in } \Omega \times [0, T], \tag{2.1}$$

$$u_\alpha = -\mathrm{K}\, \lambda_\alpha \nabla p_\alpha, \quad \text{in } \Omega, \tag{2.2}$$

with the phase mobility given by

$$\lambda_\alpha = \frac{k_{r\alpha}}{\mu_\alpha}, \tag{2.3}$$

where λ_α, $k_{r\alpha}$, μ_α and p_α are, respectively, the mobility, relative permeability, viscosity and the pressure of the α phase, and K denotes the absolute permeability of the porous medium. In particular, our interest lies in the three-phase flow, where the phase $\alpha = \{w, o, g\}$ denotes water, oil, and gas, respectively.

The fractional flow of a phase is defined as

$$f_\alpha = \frac{|u_\alpha|}{|u_T|}, \tag{2.4}$$

where $|u_T|$ represents the magnitude of the total velocity of the system in the flow direction (Rossen et al., 1999). By prescribing a fixed injection velocity, the pressure difference across the domain becomes constant after a sufficient injection time, thus reaching a steady state. The apparent viscosity μ_{app} is the inverse of the total mobility λ_T. For an assumed homogeneous core sample of length L, this property is determined from the steady-state pressure drop ΔP using the following relation:

$$\mu_{app} = \lambda_T^{-1} = \frac{K}{|u_T|} \frac{\Delta P}{L}, \quad \text{with} \quad |u_T| = \sum_\alpha |u_\alpha| \tag{2.5}$$

Thus, the fractional flow of a phase can be defined as the ratio between the mobility of the phase λ_α and the total mobility, allowing us to obtain an expression for the relative permeability of the phase as

$$f_\alpha = \frac{\lambda_\alpha}{\lambda_T} \quad \Longrightarrow \quad k_{r\alpha} = \frac{\mu_\alpha f_\alpha}{\mu_{app}}. \tag{2.6}$$

2.2 FOAM MODELING

The mathematical approaches to model the behavior of foam in subsurface environments combine fluid dynamics equations with empirical correlations observed. Basically, foam is modeled in the multiphase flows by modifying the gas mobility. Commonly, in the literature, two types of models are presented to represent foam effects: Mechanistic models describe the foam texture (bubble density) transport through a population balance differential equation (Kovscek et al., 1995; Kam, 2008; Ashoori et al., 2010; Zitha and Du, 2010; Chen et al., 2010; Zavala et al., 2024); implicit-texture models assume local equilibrium of foam effects through an algebraic expression directly modifying the gas mobility (Rosman and Kam, 2009; Rossen et al., 1999; Chen et al., 2010; CMG, 2019; Danelon et al., 2024). A detailed review of these models is presented by Hematpur et al. (2018).

Through the application of analytical methods (Lozano et al., 2021; Zavala et al., 2021; Cedro and Chapiro, 2024; Danelon et al., 2024; Fritis et al., 2024) or numerical simulations (Delshad et al., 1996; CMG, 2019; de Paula et al., 2020; Paula et al., 2022; de Paula et al., 2024), researchers can solve these models to gain insights into overall foam process performance and predict foam flow in porous media in realistic scenarios. The quality of analyses and simulation predictions depends on factors such as the precision of input parameters, the suitability of the chosen model for the studied phenomenon, and other factors, including the numerical schemes' resolution (Chen et al., 2006). Validation against experimental data and history matching with field observations are crucial steps in ensuring the reliability of simulation results (Farajzadeh et al., 2015a; Zavala et al., 2021; de Miranda et al., 2022b).

In this work, the foam flow in porous media is described mathematically by assuming that the foam is in a state of local equilibrium, where the rates of bubble generation and destruction are balanced, that is, the so-called implicit-texture or local equilibrium approach (Kovscek et al., 1995; Rossen et al., 1999; Chen et al., 2010). This approach is widely used in foam flow simulators due to its computational efficiency and numerical stability. The model assumes that foam forms instantly when water, gas, surfactant, and appropriate conditions are present. It utilizes a mobility reduction factor (MRF) term to modify gas mobility, representing the resistance caused by foam in porous media without explicitly simulating the texture of foam as an additional partial differential equation (Hematpur et al., 2018; Zhang et al., 2009).

The MRF term, in an experimental context, is defined as the ratio between the pressure drop with and without foam (Rosman and Kam, 2009). However, in mathematical models, it accounts for the gas mobility to alter the apparent viscosity in the presence of

foam:

$$\mu_{app} = \left(\lambda_w + \lambda_o + \frac{\lambda_g}{MRF} \right)^{-1}, \tag{2.7}$$

where $\lambda_w, \lambda_o, \lambda_g$ are the mobilities for water, oil and gas phases (Tang et al., 2016, 2019a).

Several factors can influence the mobility reduction provided by foam, including water and oil saturations, surfactant concentration, and the interfacial tension between phases. The empirical modeling of the mobility reduction factor calculates the combined impact of these different factors into a single value, which is used to control gas mobility. The mathematical model originating from the widely used commercial simulator `STARS` (CMG, 2019) defines the MRF by

$$MRF = 1 + fmmob \prod F_i, \tag{2.8}$$

where the F_i terms capture possible factors influencing mobility reduction, representing the multifaceted interplay of foam with other elements from the porous media model in a simplified approach. The parameter $fmmob$ describes the maximum factor by which foam is expected to reduce gas mobility.

A summarized description of MRF terms is presented in Table 1 with their corresponding mathematical expression and descriptions of their parameters. The following effects are considered: the surfactant concentration effect (F_{surf}), oil saturation (F_{oil}), shear thinning (F_{shear}), foam generation (F_{gen}), oil composition (F_{oilc}), salinity (F_{salt}), absolute permeability (F_{perm}), and foam dry-out (F_{dry}). These factors are modeled in terms of the water saturation (S_w), oil saturation (S_o), capillary number (N_{ca}), surfactant concentration (C_{surf}), oil mole fraction (C_o), salt concentration (C_{salt}) and the average permeability in a discretized block ($perm$).

Earlier versions of the `STARS` included only the terms F_{dry}, F_{oil}, F_{shear}, and F_{surf}. A similar configuration can be found in the `ECLIPSE` simulator (Spirov and Rudyk, 2015). Consequently, researchers in the relevant literature often focus on these terms when modeling foam flow in porous media. At this point, it is worth emphasizing that only a limited number of studies in the literature have addressed parameter estimation of the F_{oil} term in the context of three-phase flow, while most of the works addresses the F_{dry} or F_{shear} terms (de Miranda et al., 2025b; Ma et al., 2013, 2014a; Ribeiro et al., 2024; Valdez et al., 2021, 2022).

2.3 UNCERTAINTY QUANTIFICATION

Simulations of complex phenomena are generally subject to multiple sources of uncertainty arising from limitations in the underlying physics models, numerical approximations, and input parameter values that are assimilated with measurement errors. This is particularly true for simulations involving multiphase flow in porous media, where the

Table 1 – List of STARS terms available to represent specific foam effects and their parameters.

Foam effect term	Parameters
$F_{surf} = \left(\frac{C_{surf}}{fmsurf}\right)^{epsurf}$	*fmsurf*: critical surfactant concentration. *epsurf*: exponent parameter.
$F_{oil} = \left(\frac{(fmoil - S_o)}{(fmoil - floil)}\right)^{epoil}$	*fmoil*: oil saturation point to kill foam. *floil*: oil saturation to destabilize foam. *epoil*: exponent parameter
$F_{shear} = \left(\frac{fmcap}{N_{ca}}\right)^{epcap}$	*fmcap*: reference capillary number. *epcap*: exponent parameter.
$F_{gen} = \left(\frac{(fmgcp - N_{ca})}{fmgcp}\right)^{epgcp}$	*fmgcp*: critical N_{ca} for foam generation. *epgcp*: exponent parameter.
$F_{oilc} = \left(\frac{(fmomf - C_o)}{fmomf}\right)^{epomf}$	*fmomf*: critical oil mole fraction. *epomf*: exponent parameter.
$F_{salt} = \left(\frac{(C_{salt} - fsalt)}{(fmsalt - fsalt)}\right)^{epsalt}$	*fsalt*: lowest salt mole fraction. *fmsalt*: critical salt mole fraction. *epsalt*: exponent parameter.
$F_{perm} = \frac{1}{fmperm1} \ln\left(\frac{perm + fmperm2}{fmperm2}\right)$	*fmperm1*: parameter 1 for permeability. *fmperm2*: parameter 2 for permeability.
$F_{dry} = \frac{1}{2} + \frac{\arctan[epdry(S_w - fmdry)]}{\pi}$	*epdry*/$sfbet$: abruptness of the dry-out effect. *fmdry*/SF: critical water saturation for collapse.

presence of foam adds significant complexity. Accurate characterization and quantification of these uncertainties are crucial for establishing confidence in the predictive capabilities of the models and identifying areas for future improvements.

Uncertainty Quantification (UQ) is a systematic approach to identify, quantify, and reduce these uncertainties. By applying statistical methods to assess the impact of input variations and model assumptions, UQ can evaluate and further enhance the reliability of predictions. This section presents a panorama of the UQ workflow proposed and the techniques employed to assess the representation of foam in a multiphase flow. Figure 3 presents the schematic view of the UQ workflow used in this work. While the specific elements in this figure relate to multiphase flows in porous media, the overall UQ workflow is adaptable to evaluate any model against observational data.

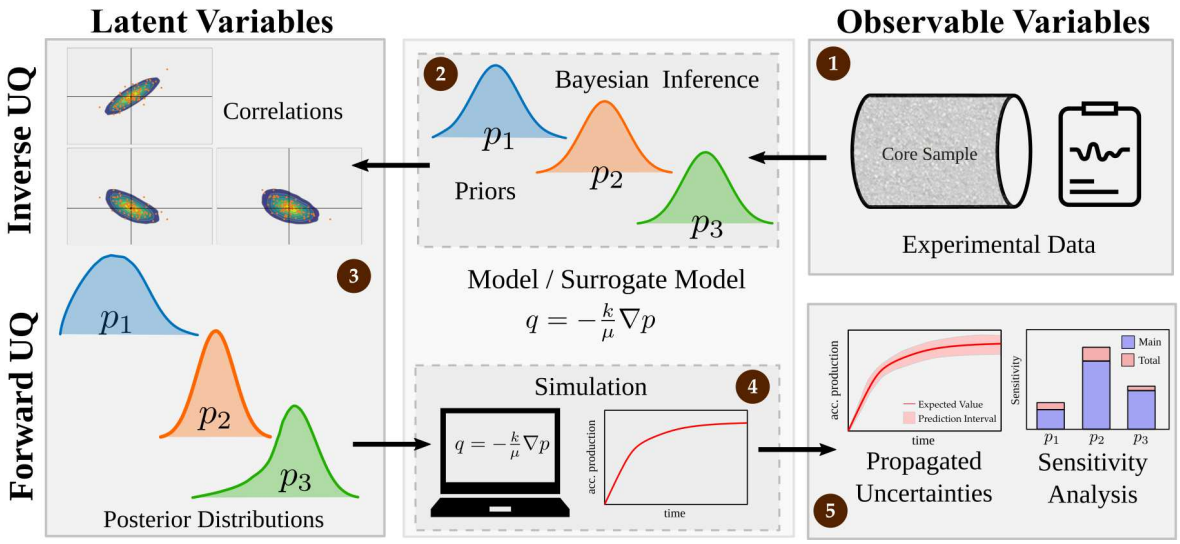

Figure 3 – Workflow for uncertainty quantification of computational models. First row: Inverse uncertainty quantification. Second row: Forward uncertainty quantification. First column: space of the latent/non-observable variables. Last column: Space of the observable/measurable variables.

The following subsections discuss the procedures and methods that are present in each step of the workflow, which is summarized as follows:

1. **Experimental Data Curation and Probabilistic Modeling** of these uncertain data, the input parameters, and their relations to be incorporated into the workflow;
2. **Parameter Inference** over the experimental data (evidence) and initial hypothesis (prior beliefs);
3. **Parameter Characterization** via diagnostics and evaluation of the posterior distributions and techniques to assess identifiability;
4. **Uncertainty Propagation** of posteriors distributions to the model;
5. **Uncertainty and Sensitivity Analysis** of the output led by variations in input variables.

The process displayed in Figure 3 usually progresses in a counter-clockwise direction, as indicated by the steps numbered from 1 to 5. The first column represents the space of latent variables, which are non-observable or non-measurable parameters within the model. In contrast, the last column encompasses the observable quantities, typically outputs of the simulators, that are evaluated against real data. The first row involves conducting the inverse UQ, a step to solve an inverse problem to estimate the latent parameter space given measurements of the observable space. The second row comprehends the forward UQ analysis, which analyzes how the uncertainties observed in the latent reflect uncertainties in the model outputs. Subsequent sections will provide a more detailed discussion of these steps.

2.3.1 Experimental Data Curation and Probabilistic Modeling

Choosing the right experimental data for calibrating and evaluating simulator parameters is vital for ensuring reliable uncertainty quantification. Factors such as experimental conditions, measurement uncertainties, and the completeness of the data must be taken into account. Accurately calibrating a model and reaching precise estimates of parameters and uncertainties requires avoiding irrelevant or inadequate data.

The physical system's probabilistic modeling is conducted by randomizing the studied parameters based on the hypothesis to be tested against data. Bayesian modeling, a fundamental concept in modern Bayesian statistics, integrates submodels or components into a structure and associates them with the data using Bayes' theorem while accounting for any uncertainties (Martin et al., 2021; McElreath, 2020). In recent years, sophisticated computational implementations have been developed to support Bayesian modeling for complex systems (Salvatier et al., 2016).

2.3.2 Parameter Inference

The Bayesian inference provides a method for assessing the credibility of the constructed probabilistic model, considering both the hypotheses and the available data. The foundation of this approach is Bayes' theorem (Martin et al., 2021; McElreath, 2020), which can be expressed mathematically as:

$$\underbrace{\mathbb{P}(\theta|D)}_{\text{posterior}} = \frac{\overbrace{\mathbb{P}(D|\theta)}^{\text{likelihood}}\ \overbrace{\mathbb{P}(\theta)}^{\text{prior}}}{\underbrace{\mathbb{P}(D)}_{\text{marginal likelihood}}}, \tag{2.9}$$

where $\mathbb{P}(\theta)$ represents the prior knowledge of the input parameters θ; $\mathbb{P}(D|\theta)$ is the likelihood function, i.e., how the observed data D is introduced on the model; and $\mathbb{P}(D)$ is the marginal likelihood or evidence, a normalization factor for the posterior distribution, $\mathbb{P}(\theta|D)$.

In Bayesian theory, probability represents the degree of credibility of one event, which can be updated with new information, unlike a fixed value in the frequentist approach (Gelman et al., 1995). This uncertainty may be based on prior knowledge about the event, such as results from previous experiments or personal belief in the event (McElreath, 2020). Bayesian inference involves updating beliefs to integrate new evidence (Gelman et al., 1995) using Bayes' theorem.

The prior distribution $\mathbb{P}(\theta)$ translates the notion one has on that event θ, in a sense that it represents the uncertainty about an event before observing the data[1]. When little

[1] The Bayesian uncertainty formulation makes no distinction between epistemic and aleatoric uncertainties (Martin et al., 2021; Soize, 2017).

is known about an event, it is common to use a uniform prior over a conservative support space, as per the principle of insufficient reason, to prevent bias. However, for parameters without clear physical interpretations, defining a trustworthy range can be challenging, thereby introducing strong bias in parameter selection when adopting a uniform prior. Other alternative strategies are also explored in the literature to decide which prior is employed (McElreath, 2020; Martin and Wiecki, 2018; Caticha and Preuss, 2004).

To link the observed data D to the unknown parameters θ, the likelihood function, $\mathbb{P}(D|\theta) = \mathcal{L}(\theta \mid D)$, measures the probability of observing data D given the parameters θ. For a continuous case with an observed dataset D, the likelihood is the product of the PDF parameterized by θ for all data $d_i \in D$:

$$\mathcal{L}(\theta \mid D) = \prod_{i=1}^{n} f_\theta(d_i), \tag{2.10}$$

where $f_\theta(d_i)$ is the PDF of θ evaluate at d_i. The likelihood function is central to many iterative algorithms when working with observed data, as it provides a measure of how well the current parameter estimates explain the observed data.

In practice, when working with observed data, Bayes' theorem is often expressed as a proportionality:

$$\underbrace{\mathbb{P}(\theta|D)}_{\text{posterior}} \propto \overbrace{\mathbb{P}(D|\theta)}^{\text{likelihood}} \overbrace{\mathbb{P}(\theta)}^{\text{prior}}. \tag{2.11}$$

This formulation is useful because the marginal likelihood $\mathbb{P}(D)$ often serves as a normalization constant and can be difficult to compute directly.

Modern Bayesian statistics leverages increasing computational power to enable iterative algorithms that were not possible decades ago. Computational tools have emerged to facilitate the development of probability models working with computational representations of random variables (Martin et al., 2021). Markov Chain Monte Carlo (MCMC) methods, such as the Metropolis algorithm, are commonly implemented in these tools to generate numerical approximations and draw samples from complex probability density functions (PDF) (Hastings, 1970). These methods often rely on evaluating the likelihood function at each iteration to update the parameter estimates. Figure 4 illustrates the iterative process of the Metropolis algorithm, demonstrating the evolution from a uniform prior to a Gaussian-shaped posterior distribution, which agrees with the Central Limit Theorem and properties of well-designed MCMC methods (Geyer, 1992).

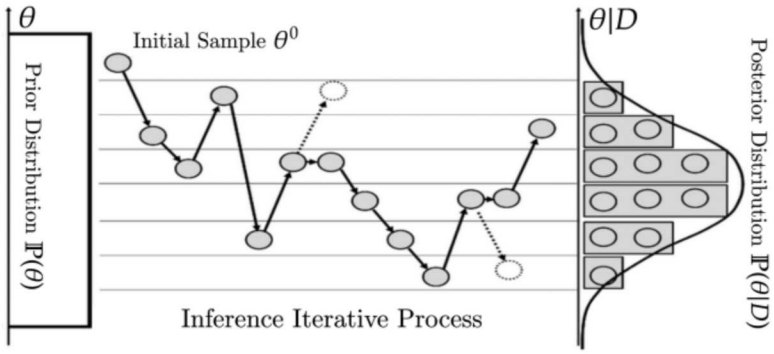

Figure 4 – Illustration of the iterative process in the classical MCMC algorithm, Metropolis. The prior hypothesis is updated to a Gaussian. Adapted from (Lee et al., 2015)

2.3.3 Parameter Characterization

The third step of the workflow we used (Figure 3, column 1) involves critically analyzing the estimated uncertainties of parameters, many of which are latent variables in petroleum reservoir characterization. This analysis aims to define appropriate probability distributions or ranges for these uncertain parameters, an important step for reliable sensitivity analysis and uncertainty propagation (Smith, 2013).

2.3.4 Uncertainty Propagation

The fourth step of the workflow illustrated in Figure 3 focuses on propagating input parameter uncertainties through the model to quantify output uncertainties. Monte Carlo (MC) sampling methods (Metropolis and Ulam, 1949) are commonly used for this purpose, relying on random sampling from the input probability distributions to generate an ensemble of input parameters. For each sample, the model is evaluated to obtain the corresponding outputs. This process is repeated many times to build statistical representations of the output distributions induced by input uncertainties. Input probability distributions are based on available data, expert knowledge, and physical constraints.

Methods based on MC rely on random sampling to achieve a numerical result. In the context of UQ, MC methods can be employed to sample from posterior distributions and achieve a prediction interval (PI) for a quantity of interest (QoI). With sufficient MC samples, statistical summaries such as means and quantiles can be obtained for the output distributions, thereby quantifying overall uncertainties and enabling risk assessments. While the concept is straightforward, MC can be computationally expensive for complex models with high-dimensional parameter spaces. It's worth noting that MC methods typically exhibit a convergence rate of $O(N^{-1/2})$ independent of dimension, where N is the number of samples, a very robust method but also slow (Caflisch, 1998). While robust and straightforward conceptually, MC can be computationally expensive for complex models.

In this context, more efficient sampling strategies and surrogate modeling techniques can be employed to improve computational efficiency (Xiu, 2010).

2.3.4.1 Surrogate Modeling

In cases where it is computationally expensive to solve the model to evaluate some QoIs, an interesting approach is to use surrogate models (also known as emulators). These statistical tools seek to approximate the output of complex physical systems at a much lower computational cost (Gramacy, 2020). Some examples of techniques commonly used for uncertainty quantification are the polynomial chaos expansion (PCE) (Xiu and Karniadakis, 2002; Ghanem and Spanos, 1991; Wiener, 1938) and the Gaussian process (GP) emulators (Gramacy, 2020).

The PCE is a particularly useful surrogate modeling technique for uncertainty quantification. It works by mapping the random input variables onto a basis of orthogonal polynomials, allowing the construction of a surrogate model that approximates the original model outputs as a polynomial function of the input variables. The key advantage of PCE is its ability to achieve accurate approximations with relatively fewer simulator evaluations compared to other techniques, such as the classical MC method, making it computationally efficient for uncertainty propagation. Figure 5 illustrates the process of constructing and using a PCE emulator. In the training phase, a set of sample input parameter values is used to evaluate the original simulator or model, and these input-output pairs are then used to compute the PCE coefficients through regression techniques. Once trained, the PCE emulator can rapidly evaluate the surrogate model for any new set of input parameter values during the usage phase, providing an inexpensive approximation of the model outputs without the need to run the full simulator.

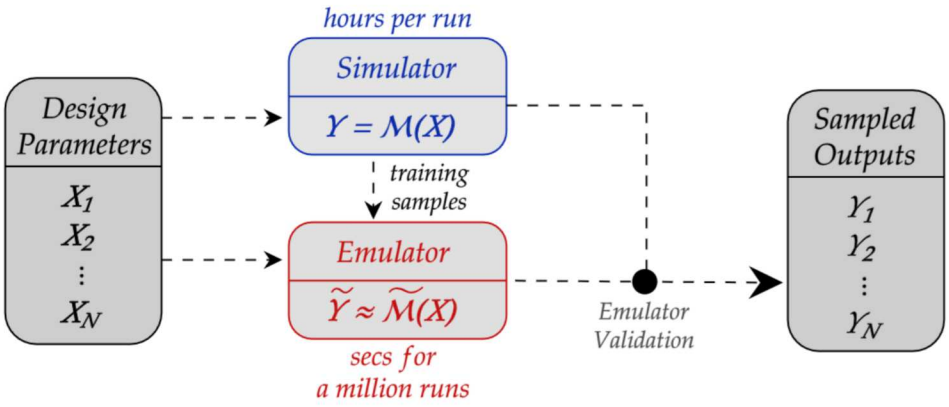

Figure 5 – Illustration of the training and usage phases for constructing and deploying a polynomial chaos expansion (PCE) surrogate model.

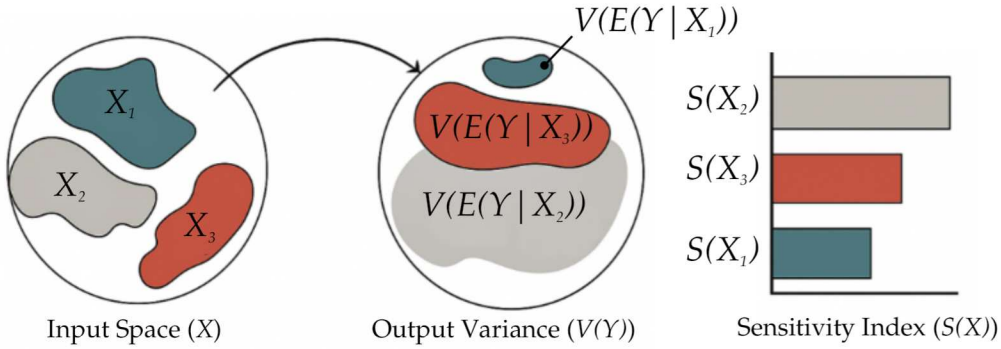

Figure 6 – Illustration of the sensitivity analysis identifying key parameters affecting model outputs and revealing areas of unnecessary complexity or needing refinement.

2.3.5 Uncertainty and Sensitivity Analysis

In the context of uncertainty quantification, sensitivity analysis (SA) (step 5 in the workflow in Figure 3) serves as a crucial tool for assessing the impact of input parameter uncertainties on model predictions and enhancing interpretability. While uncertainty quantification examines the complete propagation of input uncertainties through the model, SA aims to identify the dominant drivers of output uncertainty among the input parameters. This knowledge can be helpful for guiding model refinements to reduce model output uncertainties and/or for focusing efforts on carefully measuring specific data (Iooss and Lemaître, 2015; Saltelli, 2002; Saltelli et al., 2008).

As illustrated in Figure 6, the analysis identifies parameters with significant variations but minimal impact on the model output, potentially indicating unnecessary complexity. Conversely, it also identifies parameters with small variations that significantly influence the model output, suggesting regions in the parameter space that require refinement in the model description or in the data measurement. This aims to enhance stability and simplify models. Additionally, sensitivity analysis can help identify uncertain parameters that lead to desired or unexpected outputs, thereby enhancing the decision-making process. Overall, SA assists in understanding the impact of uncertain input parameters on output uncertainty and can guide efforts to gather more data for influential parameters or improve the precision of underlying physics models for key processes (Iooss and Lemaître, 2015; Wagener and Pianosi, 2019; Saltelli et al., 2008).

2.3.5.1 Sobol Indices

A widely used SA technique is the Sobol indices, also known as variance-based sensitivity analysis, which are metrics derived from statistical analysis of variance (ANOVA) methods. It is used to quantify the relative importance of the input parameters on the output via a decomposition of the model output's variance into fractions which can be attributed to inputs or sets of inputs (Sobol', 1990; Sobol, 2001; Saltelli et al., 2008). More specifically, the first-order Sobol index (or main Sobol index) evaluates the influence

of a given input parameter $\theta_i \in \Theta$ independently of the output. The total Sobol index evaluates the direct contribution and interactions among parameters to the variance of a given output $\mathcal{Y}$. The following expressions describe the main and total Sobol indices:

$$\mathcal{S}_{1_i} = \frac{\mathbb{V}[\mathbb{E}[\mathcal{Y}|\theta_i]]}{\mathbb{V}[\mathcal{Y}]}, \quad \text{and} \quad \mathcal{S}_{T_i} = 1 - \frac{\mathbb{V}[\mathbb{E}[\mathcal{Y}|\theta_{-i}]]}{\mathbb{V}[\mathcal{Y}]}, \tag{2.12}$$

where $\mathbb{V}[\cdot]$ is the variance, $\mathbb{E}[\cdot]$ the expected value, and θ_{-i} denotes the set of all input parameters except the θ_i parameter.

2.3.5.2 SHAP Values for Directional Sensitivity Analysis

The SHAP (SHapley Additive exPlanations) method extends sensitivity analysis by providing signed contributions that indicate the direction of parameter effects (Lundberg and Lee, 2017). For a model f with an input parameter vector $\boldsymbol{\theta} \in \mathbb{R}^M$, where M is the total number of parameters, SHAP values decompose a specific prediction $f(\boldsymbol{\theta})$ into additive contributions:

$$f(\boldsymbol{\theta}) = \phi_0 + \sum_{i=1}^{M} \phi_i(\theta_i), \tag{2.13}$$

where $\phi_0 = E[f(\boldsymbol{\theta})]$ is the baseline prediction (the expected value of the model output over the training data), and ϕ_i is the SHAP value for parameter θ_i. This value quantifies how the parameter increases or decreases the model's output relative to the baseline.

The SHAP value for parameter i is calculated by averaging its marginal contribution across all possible parameter subsets:

$$\phi_i = \sum_{S \subseteq \{1,\ldots,M\} \setminus \{i\}} \frac{|S|!(M - |S| - 1)!}{d!} \left[f_{S\cup\{i\}}(\theta_{S\cup\{i\}}) - f_S(\theta_S) \right], \tag{2.14}$$

where S represents parameter subsets, f_S is a surrogate model trained considering this subset, and θ_S represents the values of the subset S. Unlike variance-based methods, SHAP values reveal whether increasing or decreasing parameters enhance or reduce a QoI, providing directional sensitivity information for understanding foam parameter impacts on key outputs in EOR.

2.3.6 An Implementation of the UQ Framework for Porous Media Simulators

The framework for UQ described in Figure 3 is general and may be used in different fields for scientific and/or engineering applications (Eck et al., 2016). Here, we detail a particular implementation developed in this work tailored for conducting UQ & SA studies using porous media flow simulators such as `FOSSIL` (de Paula et al., 2020; Paula et al., 2022; de Paula et al., 2024), `UTCHEM` (Pope and Nelson, 1978; Delshad et al., 1996), `STARS` (CMG, 2019), and `OpenFOAM` (Horgue et al., 2015).

The `UTCHEM` simulator, developed at the University of Texas at Austin, is one of the pioneering simulators for foam flow in porous media. Developed in `FORTRAN`, it

was among the first to incorporate comprehensive foam modeling capabilities within a chemical flooding simulator (Pope and Nelson, 1978; Delshad et al., 1996). The `STARS` (Steam, Thermal, and Advanced Processes Reservoir Simulator) simulator, developed by the Computer Modelling Group (CMG), is a widely used commercial simulator for modeling foam flow in porous media. Developed in `C++`, it offers advanced thermal and compositional modeling, including sophisticated foam simulation features (CMG, 2019). In contrast, `FOSSIL` (FOam diSplacement SImuLator) is an in-house software developed at LAMAP from UFJF that implements a stable and conservative numerical algorithm with reduced numerical diffusion (de Paula et al., 2020; Paula et al., 2022; de Paula et al., 2024). These simulators, among others, provide researchers and engineers with tools to investigate foam behavior in various porous media applications.

To leverage the capabilities of foam simulators, we developed a tool that interfaces with a given simulator and automates its execution over a prescribed experimental design (defined as a set of parameter combinations to be evaluated) for UQ and/or SA studies. As illustrated in Figure 7, the tool treats the simulator as a black box, agnostic to its internal solution method. The experimental design, represented as a table with each row corresponding to a unique parameter combination, is generated and passed to the framework's wrapper component.

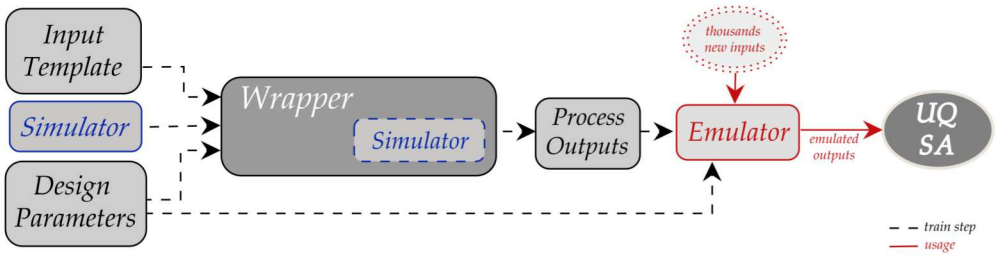

Figure 7 – Illustration of the simulator wrapper together with the emulator enabling efficient exploration of the parameter space for uncertainty quantification and sensitivity analysis.

The wrapper utilizes a templating engine to interface with the simulator, which requires a single input file in a specific format and syntax tailored to the chosen simulator. So, a template file with placeholders for input parameters is provided to the wrapper, and the placeholders are replaced with the corresponding values from the experimental design table. Automated input file generation allows seamless integration with existing simulators, as the generated files can be directly consumed without modifying the simulator's internal code.

By automating the process of generating input files and executing simulations across the experimental design, the framework enables efficient exploration of the parameter space and quantification of the resulting uncertainties. The decoupling from the simula-

tor's internal structure promotes modularity and extensibility, while the templates can accommodate various input file formats, enhancing compatibility with different simulators.

While the framework handles simulation execution, custom output processing codes are often necessary for analysis tasks specific to each simulator. Codes have been developed for our in-house simulator, `FOSSIL` (de Paula et al., 2020; Paula et al., 2022; de Paula et al., 2024), and `UTCHEM` (Pope and Nelson, 1978; Delshad et al., 1996). It is important to highlight that another in-house foam flow simulator, currently under development and based on `OpenFOAM` (Horgue et al., 2015), is also being integrated into this framework, with output processing tools tailored to its specific data structures and formats. These codes incorporate techniques like sensitivity analysis, uncertainty quantification, or surrogate modeling, enabling insights into the impact of input parameter variations on quantities of interest.

Additionally, as shown in Figure 7, the framework integrates with surrogate modeling techniques, such as polynomial chaos expansion (PCE), to create computationally efficient emulators. These emulators can rapidly approximate simulator outputs, further enhancing the efficiency of uncertainty quantification and sensitivity analysis workflows.

The framework has been implemented as a Python package, named `UQTOPUS` (Uncertainty Quantification Toolbox for `OpenFOAM` and Python Unified Simulation), providing an end-to-end uncertainty quantification workflow with pluggable sampling strategies, parallel execution support, and extensible hooks for surrogate model integration. For accessibility, the package is distributed via the Python Package Index (PyPI) and installed with the command: `pip install uqtopus`. The framework was applied to computational fluid dynamics problems using standard `OpenFOAM` tutorial cases, validating its effectiveness beyond specialized porous media simulators. The source code, along with examples and tutorials, is available at the following repository: `https://github.com/GBdeMiranda/UQTOPUS`.

3 RELATIVE PERMEABILITY AND FOAM PARAMETERS

This chapter presents the paper de Miranda et al. (2024) published in Transport in Porous Media, entitled "*Uncertainty Quantification on Foam Modeling: The Interplay of Relative Permeability and Implicit-Texture Foam Parameters*", which handles the simultaneous estimation of foam and relative permeability parameters, along with an analysis of their correlations and associated uncertainties.

3.1 INTRODUCTION

Foam has been extensively used in various applications to improve fluid flow in porous media due to its unique properties, such as its high viscosity, low density, and the ability to reduce gas mobility. In well stimulation, the introduction of foam acid diversion facilitates the creation of fractures within reservoirs, thereby augmenting permeability and stimulating well productivity (Cheng et al., 2001; Okere et al., 2020). Foam also finds its usage in delivering liquid fertilizer (Shojaei et al., 2022), which enables a uniform distribution and enhanced soil penetration, crucial for successful agricultural applications. Moreover, foam improves the transportation and distribution of remediation agents throughout the contaminated zones (del Campo Estrada, 2014). Furthermore, foam-assisted techniques in Enhanced Oil Recovery (EOR) have been shown to improve sweep efficiency and mitigate gas channeling due to reservoir heterogeneities, viscous fingering, or gravity override (Rossen, 1996; Zhang et al., 2009; Lotfollahi et al., 2016; Hematpur et al., 2018). In the context of EOR, foam has also been used to improve sweeping efficiency in steam flooding processes (Patzek and Myhill, 1989; Patzek, 1996), as well as in numerous other pilots, as recently reported by Rossen et al. (2024).

When simulating a multi-phase flow phenomenon, such as foam displacement, it is essential to carefully design the complete mathematical model, the underlying hypothesis, and components such as relative permeability, viscosity, capillary pressure, and others, to describe the correct physics (Ranade, 2002; Bear and Bachmat, 2012). However, these components are also subject to strong interactions and uncertainties that affect the model's overall response. Therefore, selecting and parameterizing these components is essential to carefully create a comprehensive and reliable fluid flow model that can replicate the complexities of real-world porous media systems and make accurate predictions. In this context, the fractional flow theory (Pope, 1980; Ding et al., 2020b) describes the fractional contribution of a displacing phase to the total flow rate in the reservoir, offering crucial insights into the mechanisms driving recovery (Zhou and Rossen, 1995; Dholkawala et al., 2007; de Miranda et al., 2022a). Adjusting a model to incorporate new techniques for foam representation in fluid displacement introduces elements of uncertainty into the mathematical formulation. To enhance the reliability of multi-phase flow simulations, it is

essential to quantify the uncertainty and identify its influential parameters accurately.

In the context of determining relative permeability for multi-phase flow in porous media, Valdez et al. (2020) utilized two datasets to explore the effects of uncertainties in input parameters from relative permeability models on the outputs of a water-oil flow, using an approach based on Bayesian inference and surrogate modeling. Berg et al. (2021b) addressed the uncertainties of relative permeabilities by employing Bayesian inference with synthetic and experimental core flooding data. Their work highlighted the considerable impact of different relative permeability models on saturation profiles, pressure drop, and relative permeabilities. Both works indicated that the choice of relative permeability models and their parameters significantly influences the accuracy of model predictions, a factor of paramount importance in a range of practical applications. In particular, for the case of foam flow for EOR, a series of works (Lotfollahi et al., 2016; Ma et al., 2014a; Valdez et al., 2021; de Miranda et al., 2022b,a) have investigated the uncertainties arising from the implicit-texture description of foam (Osterloh and Jante, 1992) in terms of the foam strength. Specifically, Valdez et al. (2021) evaluated the ability of two foam models, the one used in the `STARS` simulator (CMG, 2019) and the Linear Kinetic model (Ashoori et al., 2010), to represent the experimental data, providing insights for enhancing foam-assisted EOR processes. Focusing on the parameter estimation and their uncertainties in foam displacement models, Valdez et al. (2022) explored the utilization of different objective functions. In contrast, de Miranda et al. (2022b) introduced the measured variations in experimental data as a weighting factor to the objective function. Berg et al. (2024) presents an inverse modeling approach for the simultaneous determination of relative permeability and capillary pressure–saturation functions using a synthetic dataset. According to a recent study conducted by Ribeiro et al. (2024), it is not feasible to accurately determine both the relative permeability and foam representation using a dataset that only consists of observations of foam quality and apparent viscosity in a steady state.

In situations where models are governed by complex equations, such as partial differential equations (PDEs), the challenges associated with uncertainty quantification and sensitivity analysis become even more pronounced. In these cases, emulators come into play to enable analysis due to the lower cost of evaluating an approximation of the model. Within this context, methods such as Polynomial Chaos Expansion (PCE) and Gaussian Process (GP) gain prominence. Global sensitivity analysis is crucial for understanding the complex interdependencies between various parameters that affect flow dynamics. Sochala and Maî, L. tre (2013) delved into the impact of uncertainty in hydrological laws on subsurface flows, as modeled by Richards' equation. Their study utilizes PCEs to efficiently quantify the effects of hydrological parameter uncertainties on the behavior of the wetting front. It demonstrates that second-order PC expansions are adequate for capturing the output quantities of interest. This approach significantly enhanced the

efficiency of simulation processes compared to traditional Monte-Carlo methods by using a non-intrusive spectral projection to obtain PC decomposition coefficients. Their findings, across three test cases with different hydrological laws, revealed that second-order PCE suffices for capturing the quantities of interest due to the smooth dependencies of the considered problems. Bazargan et al. (2015) employed PCE to approximate the outputs of reservoir models, providing a more nuanced approach to uncertainty quantification. Similarly, Kim et al. (2022) leveraged surrogate PCE alongside Global Sensitivity Analysis for multi-phase, multi-component numerical simulators in soil remediation scenarios. These advanced techniques demonstrate their efficacy in delivering reliable predictions and addressing the inherent challenges in environmental and reservoir models.

However, while previous studies on foam flow have made significant advances in examining uncertainties in implicit-texture models, none of these works have explored the intrinsic interactions among the components of relative permeability and foam parameters, thereby limiting the scope of the analyses. Also, previous works on uncertainty quantification on foam models have been limited to steady-state foam models without solving the governing PDEs and analyzing their outputs. The present work addresses these gaps by conducting an uncertainty quantification and sensitivity analysis of a foam implicit-texture model based on the `STARS` formulation (CMG, 2019) and the Corey relative permeability model (Corey, 1954; Brooks and Corey, 1963) to better understand the interactions between these two components. Inverse uncertainty quantification, which characterizes model parameters and their associated uncertainty, relies on Bayesian techniques that utilize improved prior distributions. To propagate uncertainties through the governing partial differential equations of foam flow, we utilized an in-house foam displacement simulator, aided by a surrogate model based on PCE, to carry out further uncertainty quantification.

The remaining of this chapter is organized as follows: Section 3.2 outlines the fundamental equations and theories governing two-phase flow in porous media, particularly discussing the fractional flow theory for water and gas flow in the presence of foam; Section 3.3 delves into inverse and forward uncertainty quantification based on Bayesian techniques and Sobol Indices, which are used for model calibration and sensitivity analysis, respectively; Section 3.5 applies the discussed methods to estimate parameters in the `STARS` mathematical model for foam flow in porous media. Finally, Sections 3.6 and 3.7 discuss the results, highlighting possible future steps for research and synthesizing the findings of this work.

3.2 MATHEMATICAL MODEL

Many mathematical models have been developed to analyze the two-phase flow of water and gas in the presence of foam in a porous medium. In this work, we focus on analyzing a water-gas flow with foam in a one-dimensional domain Ω representing

a saturated porous medium, where the aqueous and gaseous phases are represented by $\alpha = \{w, g\}$. The mathematical model for this problem is based on the principle of mass conservation for each phase, where the saturation and velocity of each phase are denoted by S_α and u_α, respectively. Assuming incompressible and immiscible phases, a saturated system is represented as $S_w + S_g = 1$. The Darcy law determines the rate of fluid flow for a given phase, expressed as a function of the pressure of each phase, denoted by p_α, and its mobility, denoted by λ_α.

The governing equations for two-phase flow are given by:

$$\phi \frac{\partial}{\partial t} S_\alpha + \frac{\partial}{\partial x} u_\alpha = 0, \qquad \text{in } \Omega \times [0, T], \tag{3.1}$$

$$u_\alpha = -\lambda_\alpha \frac{\partial}{\partial x} p_\alpha, \qquad \text{in } \Omega, \tag{3.2}$$

with ϕ denoting the porosity and T representing the final time.

The mobility of phase α is a function of the relative permeability $k_{r,\alpha}$ and viscosity μ_α, and is given by

$$\lambda_\alpha = \frac{k_{r,\alpha}}{\mu_\alpha}. \tag{3.3}$$

The Corey-Brooks equations describe water and gas relative permeability for two-phase flow in porous media (Corey, 1954; Brooks and Corey, 1963). These equations assume that the relative permeabilities of each phase are functions of their saturations and can be defined for water and gas as:

$$k_{rw} = k_{rw}^0 \left(\frac{S_w - S_{wc}}{1 - S_{wc} - S_{gr}} \right)^{n_w}, \quad \text{and} \quad k_{rg} = k_{rg}^0 \left(\frac{S_g - S_{gr}}{1 - S_{wc} - S_{gr}} \right)^{n_g}. \tag{3.4}$$

The parameters k_{rw}^0 and k_{rg}^0 denote the end-point relative permeabilities, while S_{wc} and S_{gr} are the residual saturations for water and gas. The exponents n_w and n_g, often called Corey's exponents, describe the curvature or shape of the relative permeability curves for water and gas. These parameters are often determined using experimental data from core flooding experiments in laboratories (Berg et al., 2021b,a; Valdez et al., 2020).

The fractional flow theory for gas-water flow is a mathematical framework to describe the multi-phase flow in porous media (Dholkawala et al., 2007; Rossen et al., 1999; Zhou and Rossen, 1995; Larson, 1978). The fractional flow of a given phase, denoted by f_α, represents the volumetric displacement fraction in a specific direction dominated by phase $\alpha = \{w, g\}$ and can be written as

$$f_\alpha = \frac{\lambda_\alpha}{\lambda_T}, \tag{3.5}$$

where total mobility is $\lambda_T = \sum_\alpha \lambda_\alpha$.

From Darcy's law for the total velocity, a direct relation between the apparent viscosity μ_{app} and the pressure difference ΔP across the core sample can be written as

$$u_T = \frac{K}{\mu_{app}} \frac{\Delta P}{L}, \tag{3.6}$$

where K is the absolute permeability of the porous medium, u_T is the magnitude of the superficial velocity, and L is the length of the core sample. This relationship is commonly utilized in experimental settings to assess fluid flow characteristics in porous media.

3.2.1 Foam modeling

Modeling foam flow in porous media presents a significant challenge due to the complex interplay of foam properties, porous media characteristics, and flow dynamics. Early attempts to model foam flow relied on population balance equations, pioneered by Falls et al. (1988) and Patzek (1988). This approach incorporates a conservation equation for the number density of foam bubbles, treating foam as a component of the gas phase. The bubble population balance equation is analogous to mass and energy balances commonly used in reservoir simulations.

These models explicitly track bubble generation and coalescence through rate expressions dependent on saturations and surfactant concentration, as well as lamella mobilization. The apparent viscosity of the gas phase is modified based on the texture of foam bubbles, capturing the non-Newtonian behavior of foam. However, while offering a detailed representation of foam texture evolution, these population balance models may be computationally expensive (Kovscek et al., 1997; Rossen et al., 1994; Bertin et al., 1999; Chen et al., 2010; Lozano et al., 2021).

The implicit-texture model is frequently used to describe how foam affects flow in porous media, assuming that foam is in local equilibrium; that is, the rates of bubble generation and destruction are equal. Implicit-texture models offer computational efficiency and are easily implemented in foam flow simulators. The principle behind the implicit-texture model lies in representing the foam's intricate structure and effects on fluid flow without explicitly simulating foam texture as an additional partial differential equation (Hematpur et al., 2018; Zhang et al., 2009; Falls et al., 1988; Patzek, 1988). An example is the `STARS` simulator (CMG, 2019), which uses a mobility reduction factor (MRF) term instead of evaluating bubble density. Many factors affect mobility reduction, such as water and oil saturations, surfactant concentration, interfacial tension between phases, and others. The MRF term, the mobility reduction factor, calculates the combined impact of these factors into a single value, which is used to control gas movement (Boeije and Rossen, 2013; Kapetas et al., 2015).

The modified gas mobility in the presence of foam is used to alter the apparent

viscosity, and therefore, the apparent viscosity is given by:

$$\mu_{app} = \left(\lambda_w + \frac{\lambda_g}{MRF}\right)^{-1}. \tag{3.7}$$

In an experimental context, the mobility reduction factor MRF is defined as the ratio between the pressure drop with and without foam (Rosman and Kam, 2009), that is, $\Delta P_{foam}/\Delta P$. In the `STARS` mathematical model, the mobility reduction factor is defined by

$$MRF = 1 + fmmob \prod F_i, \tag{3.8}$$

where the F_i terms capture possible factors influencing mobility, representing the multi-faceted interplay of foam with other elements from the porous media model. The parameter *fmmob* describes the maximum factor by which foam is expected to reduce fluid mobility.

In this work, we follow Ma et al. (2014a) and consider only the factor F_{dry} that describes how water saturation impacts the mobility reduction, which is given by:

$$F_{dry} = \frac{1}{2} + \frac{1}{\pi}\text{arctg}\left(sfbet(S_w - SF)\right). \tag{3.9}$$

where SF indicates an approximation for the critical water saturation above which foam collapses, and *sfbet* represents the sharpness of the transition between the low- and high-quality regimes. Figure 8 depicts these regimes in steady-state pressure gradients, illustrating how the transitional gas fraction f_g^* distinguishes these regimes, which are characterized as:

- High-quality regime (dry): Characterized by bubble coalescence at a limiting capillary pressure, this regime is independent of gas and liquid flow rates. The pressure gradient in this regime is almost independent of the velocity of the gas phase (Afsharpoor et al., 2010);
- Low-quality regime (wet): This regime features a fixed bubble size and exhibits variations in water saturation depending on the flow rates. In contrast to the strong foam regime, the pressure gradient in the weak foam regime is almost independent of the liquid phase's velocity. The weak foam regime is governed by bubble trapping and mobilization mechanisms.

3.3 METHODS FOR UNCERTAINTY QUANTIFICATION

In this section, we describe the methods and the workflow used for uncertainty quantification of the foam flow and relative permeability models. The first step is to carry out the inverse uncertainty quantification using experimental (or synthetic) data to characterize the parameters and their uncertainty. The second step consists of propagating

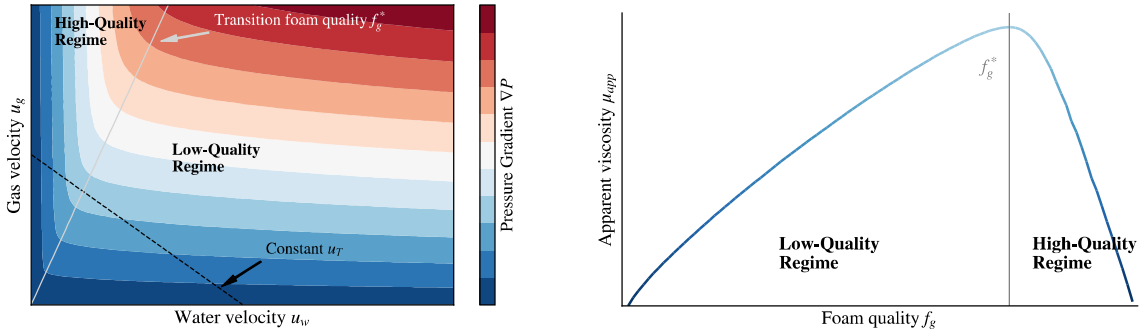

Figure 8 – Schematic representation of the foam quality regimes. The panel relates the foam quality regimes from (a) the representation presented by Osterloh and Jante (1992) of the pressure gradient as a function of gas and water superficial velocities, and (b) The apparent viscosity as a function of foam quality in a constant total velocity u_T.

this uncertainty from the input parameters to the model outputs. In particular, this work presents studies carried out for both the `STARS` steady-state model and the PDEs governing foam flow in porous media. A sensitivity analysis was also conducted using the knowledge gained from the parameters in the first step.

3.3.1 Inverse Uncertainty Quantification

Inverse uncertainty quantification (IUQ) is used to infer the model's parameters and their uncertainties from observed data, enabling accurate prediction and characterization of model outcomes. In particular, Bayesian IUQ involves finding a posterior distribution of model parameters that is consistent with both the observed data and prior knowledge about the system.

Bayesian inference involves estimating the posterior distribution of model parameters, denoted here by Θ, given observed data D, utilizing Bayes' theorem:

$$P(\Theta|D) = \frac{P(D|\Theta) \cdot P(\Theta)}{P(D)}, \tag{3.10}$$

where $P(\Theta)$ is the prior distribution representing initial beliefs or prior knowledge about the parameters, $P(D|\Theta)$ is the likelihood function expressing the probability of observing data D given the parameters Θ, and $P(D)$ is the marginal likelihood or evidence. After incorporating the observed data, the posterior distribution $P(\Theta|D)$ summarizes our updated knowledge about the parameters.

Several methods are available within the Bayesian inference framework to obtain the posterior probabilities, including Markov Chain Monte Carlo (MCMC) techniques (Brooks, 1998), Approximate Bayesian Computation (ABC) (Csill'e, ry et al., 2010), and Variational Inference (Blei et al., 2017), each providing different approaches to estimate posterior distributions.

Among the MCMC methods existing in the literature, the Metropolis algorithm (Metropolis et al., 1953) is the classical one and has been successfully employed in many studies. However, a notable disadvantage of the Metropolis is its inefficiency in exploring high-dimensional or strongly correlated parameter spaces. In these cases, the method tends to exhibit poor convergence, making it less suitable for complex models where effective exploration of the parameter space is crucial for accurate inference.

In particular, the Hamiltonian Monte Carlo (HMC) algorithm, a member of the Markov chain Monte Carlo (MCMC) family that is well-suited for sampling from complex probability distributions, particularly those with high dimensionality, was employed in this work. Unlike other MCMC methods that suffer from random walk behavior and sensitivity to correlated parameters, HMC takes steps informed by first-order gradient information. This unique feature enables it to converge faster to high-dimensional target distributions than methods like random walk, Metropolis, or Gibbs sampling. HMC simulates trajectories of these equations using numerical integration techniques, generating new proposed states that effectively explore the posterior distribution. Divergences in the Hamiltonian Monte Carlo arise when the simulation of Hamiltonian dynamics encounters numerical instability or approximation errors, leading to a discrepancy between the proposed and simulated trajectories. These divergences indicate a potential issue with the model's parameterization or the algorithm's tuning and are essential to diagnose and address for reliable inference (Betancourt and Girolami, 2013; Carpenter et al., 2017; Betancourt, 2018)

3.3.1.1 Prior Selection

Selecting a prior distribution is a fundamental step in Bayesian analysis when using the MCMC method. In this work, we selected priors for the parameters based on physical assumptions or using the maximum entropy principle.

Essentially, the maximum entropy principle selects the distribution with the highest entropy from a set of distributions that represent our incomplete information. The principle finds the PDF that maximizes the entropy functional, as mentioned by Soize (2017). Based on the given information about the support and statistical properties of the random variable in question, the maximum entropy principle results in the probability distribution for that variable, ensuring that no unwarranted assumptions are made. Employing the maximum entropy prior in Bayesian inference is justified as it leverages only available information to construct the prior and avoids introducing extraneous data (Neumann et al., 2007; Caticha and Preuss, 2004).

Table 2 shows the corresponding distribution indicated by the maximum entropy principle for two cases where support and constraints are known.

Table 2 – Support and constraints about a random variable and the corresponding distributions given by the maximum entropy principle. Parameters $a, b \in \mathbb{R}$ represent lower and upper limits of the support, and $\mu \in \mathbb{R}^+$ represents the mean value of the random variable X.

Support	**Constraints**	**Distribution**
$a \leq x \leq b$	-	$X \sim \mathcal{U}[a, b]$
$x \geq 0$	$\mathbb{E}[x] = \mu$	$X \sim \text{Exp}(\mu)$

3.3.2 Forward Uncertainty Quantification

Forward UQ employs sampling methods to systematically generate scenarios that vary input parameters according to their prescribed probability distributions. By simulating these scenarios using the predictive model, the extraction of statistics such as means, variances, and quantiles is enabled over a Quantity of Interest (QoI). This approach captures the inherent variability stemming from input uncertainty, providing a way to characterize the range of potential outcomes and assess the reliability of predictions.

There are many available techniques to carry out a forward UQ study, ranging from the classical Monte Carlo method to more efficient approaches based on surrogate modeling, such as the polynomial chaos expansion (PCE) or Gaussian process (GP). For a detailed description, see Eck et al. (2016).

3.3.3 Polynomial Chaos Expansion

Emulation, also referred to as surrogate modeling, is the process of approximating a computationally expensive numerical model with a more efficient surrogate. This approach is particularly useful when the original model requires significant computational resources to be evaluated several times, which is the case in UQ and SA studies (Gramacy, 2020; Luthen et al., 2021). Polynomial Chaos Expansion (PCE) is a widely used technique for constructing a surrogate for a specific QoI. This surrogate model approximation is constructed after a few runs of the forward problem, allowing for a mapping between the input samples and the model's outputs. After its construction, it can be cheaply evaluated to obtain an approximation of the output due to its polynomial nature. The PCE-based surrogate can also be used to obtain statistical moments and sensitivity indices. A brief overview of the PCE's construction for surrogate modeling is presented next. To access a comprehensive and detailed derivation, see Xiu and Karniadakis (2002); Ghanem and Spanos (1991); Wiener (1938); Eck et al. (2016); Ernst et al. (2012); Feinberg and Langtangen (2015); Marelli and Sudret (2015) and Sudret (2008).

Consider a quantity of interest $\mathcal{Y}$ computed by a simulator $\mathcal{M}(\mathbf{Z})$, where $\mathbf{Z}$ denotes the input parameters, which are represented by a random vector with independent components that belongs to $\mathbb{R}^D$ (Ernst et al., 2012). For each $i = 1, \ldots, D$, let f_{Z_i} denote the marginal distribution of Z_i. The joint probability density function (PDF) of $\mathbf{Z}$ is

represented by $f_{\mathbf{Z}}(\mathbf{z}) = \Pi_{i=1}^{D} f_{Z_i}$. Assuming that the model output $\mathcal{Y} = \mathcal{M}(\mathbf{Z})$ has a finite variance,

$$\mathbb{E}\left[\mathcal{Y}^2\right] = \int_{\mathcal{D}_{\boldsymbol{Z}}} \mathcal{M}^2(\boldsymbol{z}) f_{\boldsymbol{Z}}(\boldsymbol{z}) \mathrm{d}\boldsymbol{z} < \infty, \tag{3.11}$$

where $\mathbb{E}[X]$ denotes the mean value of a random variable X with density f_X. The PCE representation for $\mathcal{Y} = \mathcal{M}(\mathbf{Z})$ is defined as:

$$\mathcal{Y} = \mathcal{M}(\mathbf{Z}) = \sum_{\boldsymbol{\alpha} \in \mathbb{N}^D} b_{\boldsymbol{\alpha}} \Psi_{\boldsymbol{\alpha}}(\boldsymbol{Z}), \tag{3.12}$$

where $\Psi_{\boldsymbol{\alpha}}(\boldsymbol{X})$ are multivariate orthonormal polynomials with respect to $f_{\mathbf{Z}}$, $\boldsymbol{\alpha} \in \mathbb{N}^D$ is a multi-index notation used for the identification of the multivariate polynomials $\Psi_{\boldsymbol{\alpha}}$, and $b_{\boldsymbol{\alpha}}$ are the coefficients of the expansion.

In practice, the expansion is truncated at a finite number of terms, and the approximation of $\mathcal{Y}$, obtained by the emulator $\mathcal{M}_{PCE}$ and denoted by $\mathcal{Y}_{PCE}$, can be expressed by:

$$\mathcal{Y} \approx \mathcal{Y}_{PCE} = \mathcal{M}_{PCE}(\mathbf{Z}) = \sum_{j=0}^{N_p - 1} c_j \Psi_j(\mathbf{Z}), \tag{3.13}$$

where c_j are the coefficients of the expansion to be determined and $\Psi_j(\mathbf{Z})$ are the orthogonal polynomials.

The polynomial basis $\Psi_{\boldsymbol{\alpha}}(\boldsymbol{Z})$ is constructed from a set of univariate orthonormal polynomials $\phi_k^{(i)}(z_i)$ of degree p. These orthonormal polynomials satisfy the following equation:

$$\left\langle \phi_j^{(i)}(z_i), \phi_k^{(i)}(z_i) \right\rangle = \int_{\mathcal{D}_{Z_i}} \phi_j^{(i)}(z_i)\, \phi_k^{(i)}(z_i)\, f_{Z_i}(z_i)\, \mathrm{d}z_i = \gamma_j^{(i)} \delta_{jk}, \tag{3.14}$$

where i identifies the input variable, j and k are the polynomial degrees such that $0 \leq j, k \leq p$, and δ_{jk} is the Kronecker delta.

The multivariate polynomials are created by taking the tensor products of their univariate counterparts. This can be represented as:

$$\Psi_{\boldsymbol{\alpha}}(\boldsymbol{z}) = \prod_{i=1}^{D} \Psi_{\alpha_i}^{(i)}(z_i) \tag{3.15}$$

The orthogonality of the univariate polynomials in Eq. (3.14) leads to:

$$\langle \Psi_{\boldsymbol{\alpha}}(\boldsymbol{z}), \Psi_{\boldsymbol{\beta}}(\boldsymbol{z}) \rangle = \delta_{\boldsymbol{\alpha}\boldsymbol{\beta}}, \tag{3.16}$$

One method for creating orthogonal polynomials is the discretized Stieltjes procedure (Feinberg and Langtangen, 2015; Marelli and Sudret, 2015). In the multivariate scenario, components of $\mathbf{Z}$ must be independent. The polynomial expansion of Eq. (3.13) has a degree of p for D input parameters. The number of terms in the polynomial expansion is given by:

$$N_p = \frac{(D+p)!}{D!p!}. \tag{3.17}$$

The surrogate model is built from a total of N_s samples, which can be expressed as $N_s = mN_p$. Here, m is a multiplicative factor typically used.

There are different methods available to calculate coefficients, denoted by c_j, which are used to build an emulator for a specific QoI. In this study, the stochastic collocation method (Xiu and Hesthaven, 2005) was used to determine the coefficients of the PCE. This method results in either an interpolation or regression problem, depending on the choice of the multiplicative factors m and the resulting number of samples N_s. When $m = 1$ (hence, $N_s = N_p$), an interpolation problem occurs. On the other hand, when $m > 1$, a regression problem arises, which can be solved using least squares methods. In all cases studied in this work, the regression approach ($m > 1$) was used for constructing the PCE surrogates.

In the regression case, where $Y = \mathcal{M}(\mathbf{Z})$ and the truncated polynomial chaos expansion was used (as given in Eq. (3.13)), the unknown coefficients were estimated by minimizing the mean square residual error (Marelli and Sudret, 2015), that is

$$\hat{\boldsymbol{c}} = \arg\min \frac{1}{N_s} \sum_{i=1}^{N_s} \left(\mathcal{M}(\boldsymbol{z}_i) - \sum_{\boldsymbol{\alpha} \in \mathbb{N}^D} c_{\boldsymbol{\alpha}} \boldsymbol{\Psi}_{\boldsymbol{\alpha}}(\boldsymbol{z}_i) \right)^2 . \tag{3.18}$$

3.3.4 Sensitivity Analysis via Sobol Indices

Sensitivity analysis assesses how changes in a model's inputs affect its output, providing insight into the parameters that most influence the results. Numerous methods for sensitivity analysis exist, ranging from variance-based techniques, such as Sobol indices, to local methods, including one-factor-at-a-time exploration (OAT) (Daniel, 1973; Hamby, 1994). In particular, the Sobol index is a global sensitivity analysis technique used to study how variability in a model's output can be attributed to different sources of variation in its inputs. Unlike local sensitivity techniques, global sensitivity analysis enables the evaluation of simultaneous changes in all model parameters across their entire range. This tool assesses the contribution of individual input parameters (or their groups) to the output variance, improving the understanding of the model's behavior under uncertainty (Sobol, 2001; Saltelli et al., 2008).

Sobol indices decompose the variance of the model orthogonally with respect to individual variables or groups of variables. The first-order Sobol index $\mathcal{S}_{1_i}$ evaluates the independent influence of a specific input parameter $\theta_i \in \Theta$ on the output $\mathcal{Y}$ of a given model. Conversely, the total Sobol index $\mathcal{S}_{T_i}$ evaluates both the direct contribution (evaluated via the first-order index) and also the interactions among parameters to the variance of $\mathcal{Y}$. The expressions for these indices are given by:

$$\mathcal{S}_{1_i} = \frac{\mathbb{V}[\mathbb{E}[\mathcal{Y} \mid \theta_i]]}{\mathbb{V}[\mathcal{Y}]}, \quad \text{and} \quad \mathcal{S}_{T_i} = 1 - \frac{\mathbb{V}[\mathbb{E}[\mathcal{Y} \mid \theta_{-i}]]}{\mathbb{V}[\mathcal{Y}]}, \tag{3.19}$$

where θ_{-i} represents all input parameters except the θ_i parameter.

In this work, the Sobol indices were calculated using either the surrogate models constructed in this study, as available in the UQLab libraries, or the Saltelli method, as implemented in SALib. The calculations using the surrogate models were employed for the cases solving the PDE models, whereas the latter was used for the simpler steady-state model.

3.4 DATA AND METHODS

Data from relative permeability and foam quality-scan experiments were used to determine parameters and their uncertainties. In particular, the present study utilized synthetic dataset parameters presented by Gassara et al. (2017), which were fitted from experimental data provided by Pedroni (2017).

Next, we provide a brief description of the experimental setting and data. The experimental setup involved foam displacement within a Fontainebleau sandstone core. The gaseous phase employed in the experiment consisted of a mixture composed of 80% carbon dioxide and 20% methane. The aqueous phase consisted of desulphated synthetic seawater (DSW) containing a dissolved surfactant at a concentration of 5 g/L, which facilitated foam generation. The experimental conditions were set at a temperature of 60°C and a pressure of 80 bar. More details can be found in Pedroni (2017).

Table 3 displays the parameters and their corresponding values used to generate the synthetic data used in this work. To simulate uncertainty in observations, a Gaussian noise relative to the maximum observed value for each output ($k_{rg}, k_{rw}, \mu_{app}$) is included.

Table 3 – Parameter values used to generate a synthetic dataset based on the work of Gassara et al. (2017).

Parameter	μ_w	μ_g	S_{wc}	S_{gr}	k^0_{rw}	k^0_{rg}	n_w	n_g	*fmmob*	*SF*	*sfbet*
Value	0.50	0.021	0.2	0.1	0.5	0.6	4.20	1.40	4341	0.3409	424

In this work, the irreducible saturations S_{wc} and S_{gr} were not included as adjustable parameters following many inverse studies from the literature (Borazjani et al., 2021; Hemmati et al., 2024; Lomeland et al., 2005). In addition to this, the irreducible saturations are responsible for high correlations between fitting parameters, as discussed by Berg et al. (2021a,b), due to the coupling between them and the endpoint permeabilities. Therefore, their inclusion in the analysis could also affect the correlations between the parameters and, in this way, hinder the interplay between the foam and relative permeability parameters, which is the primary focus of this work.

3.4.1 Construction of the Priors Distributions

Uniform distributions with large support were assumed for the relative permeability parameters n_w, n_g, k^0_{rw}, and k^0_{rg}, following the choice used in the work of Berg et al.

(2021a). For the foam parameters *fmmob*, *SF*, and *sfbet* previous studies (Valdez et al., 2022, 2021) also employed uniform prior distributions. However, in this case, the chosen boundaries for the uniform prior introduce the researcher's biases and might significantly influence the inference outcome since no prior knowledge is available for the parameters *fmmob* and *sfbet* based on their physical meaning. In general, these boundaries are set in a trial-and-error procedure. The foam *SF* parameter, on the other hand, is limited by physical principles within the range $[S_{wc}, 1 - S_{gr}]$.

As shown in Table 2, having a clear interval defined for the support, the uniform distribution will be attained via the principle of maximum entropy.

To select priors for *sfbet* and *fmmob* parameters based on the maximum entropy principle, an approximation of these parameters is provided in order to apply the same principle. Therefore, two approaches (Boeije and Rossen, 2013; Zeng et al., 2016) for estimating the parameters of the `STARS` mathematical model using steady-state foam data are briefly revised. The main advantage of these approaches is that they are simple and can be carried out easily to provide reliable information about the parameters (Boeije and Rossen, 2013). The method of Boeije and Rossen (2013) is used to provide information for the *fmmob* parameter, whereas the method of Zeng et al. (2016) provides information about the *sfbet* parameter.

3.4.1.1 Priors for *fmmob* and *sfbet*

To obtain information about the maximum mobility reduction factor *fmmob*, we use the algorithm presented in Boeije and Rossen (2013), which splits apparent viscosity data in low- and high-quality regimes, as shown in Figure 9. In this work, two convex curves were used to approximate the apparent viscosity in both low- and high-quality regimes. The intersection of these two curves represents the critical foam quality denoted by f_g^*, where the apparent viscosity is maximum.

The critical water saturation S_w^*, which can also be interpreted as an approximation for *SF*, can be found via Darcy's law for the water phase:

$$\left(1 - f_g^*\right) = \frac{k_{rw}\left(S_w^*\right)}{\mu_w} \mu_{app}\left(f_g^*\right). \tag{3.20}$$

Then, once the critical point of foam quality and apparent viscosity is obtained, which is denoted here by $(\mu_{app}(f_g^*), f_g^*)$, it is possible to find an approximation for the *fmmob* parameter, represented here by $\overline{fmmob}$, through Darcy's law for the gas phase:

$$\frac{1}{1 + \overline{fmmob}} = \frac{f_g^* \mu_g}{k_{rg}\left(S_w^*\right) \mu_{app}\left(f_g^*\right)}. \tag{3.21}$$

To approximate *sfbet*, some calculations presented in the method of Zeng et al. (2016) are used. The original method consists of an iterative approach, whereas here, only

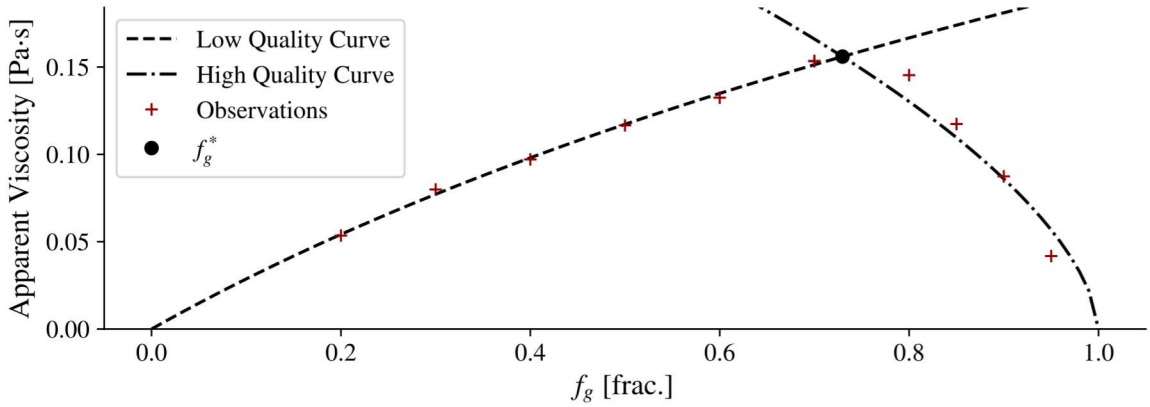

Figure 9 – First step of the method proposed by Boeije and Rossen (2013) to estimate the critical foam quality, f_g^*. The dot symbol marks the intersection between the two curves, which fit the low- and high-quality foam regimes.

a single step will be considered. This approach uses $\overline{fmmob}$, which after some algebraic manipulation on Eqs. (3.5)-(3.9), results in the following linear relation for S_w given by

$$\tan\left(\left(\frac{MRF-1}{\overline{fmmob}}-0.5\right)\pi\right)=\overline{sfbet}\,(S_{\mathrm{w}}-S_w^*)\,, \tag{3.22}$$

where the mobility reduction factor MRF is computed using Eq. (3.8). Then, $\overline{sfbet}$ can be obtained as the angular coefficient from the right-hand side of Eq. (3.22).

Finally, given the previous information $\overline{sfbet}$ and $\overline{fmmob}$, one can consider the maximum entropy principle to assign exponential prior distributions for these parameters. A summary of all the choices for prior distributions of the parameters from relative permeability and foam models is shown in Table 4.

Table 4 – Foam parameters and the associated prior distribution for Bayesian inference.

Parameter X	Information	Support	Prior
$fmmob$	4287.503	$[0,\infty)$	$\mathrm{Exp}\left(\overline{fmmob}^{-1}\right)$
$sfbet$	107.310	$(0,\infty)$	$\mathrm{Exp}\left(\overline{sfbet}^{-1}\right)$
SF	0.301	$(S_{wc}, 1-S_{gr})$	$\mathcal{U}[S_{wc}, 1-S_{gr}]$
k_{rg}^0	-	$(0,\infty)$	$\mathcal{U}[0.01, 1.2]$
k_{rw}^0	-	$(0,\infty)$	$\mathcal{U}[0.01, 1.2]$
n_w	-	$(0,\infty)$	$\mathcal{U}[0.1, 10]$
n_g	-	$(0,\infty)$	$\mathcal{U}[0.1, 10]$

3.4.2 Computational Tools

Using the experimental data along with the Bayesian model consisting of the priors outlined in Table 4 and the Eqs. (3.3)-(3.6), the Bayesian inference process for foam parameters is conducted with the help of the `PyMC3` library (Salvatier et al., 2016). For the Bayesian inference, four independent chains are created, and the combination of

these chains provides the posterior distribution for each parameter. The HMC variant NUTS (Hoffman and Gelman, 2014) is used as the step function. A total of 10^5 samples are drawn for each randomized parameter, and 10^3 samples are utilized for the *burn-in* phase.

The uncertainties found in the parameters are propagated to the outputs of computer simulations of one-dimensional foam core-flooding using the numerical simulator `FOSSIL` (FOam diSplacement SImuLator) (de Paula et al., 2020; Paula et al., 2022). In particular, we considered quantities of interest from the core flooding simulation, including breakthrough time and pressure drop across the core. The simulator is designed to solve two-phase foam flow in porous media, governed by Eqs. (3.1) and (3.2), and is based on robust and efficient numerical methods. It is also capable of incorporating several features, such as non-Newtonian foam, heterogeneous media, capillary pressure, and other complexities (Paula et al., 2022; Vásquez et al., 2022). A detailed study on the prior selection is presented in Section A.1.

3.5 RESULTS

This section presents the numerical experiments conducted to quantify uncertainty and analyze the sensitivity of the foam models. First, we present the parameter characterization using the inverse UQ based on the MCMC method to obtain the posterior distribution of the parameters. Next, the uncertainties are propagated to both the steady-state foam model and the PDE-based model. In addition, sensitivity analyses are also carried out.

3.5.1 Inverse Uncertainty Quantification

Figure 10 shows the marginal posterior distributions (on the top diagonal) as well as pairwise projections of the posterior distributions for all the parameters. The red points represent the ground-truth value for each parameter. The posterior distributions exhibit consistency and a tight credible interval around the true parameters across multiple sampling runs, indicating convergence in Bayesian inference. Moreover, a detailed convergence diagnostics and additional analysis can be found in Section A.2. It can be observed that the obtained posterior distributions are able to comprise the ground-truth value. The slight mismatch in the peak of the posterior distributions and the ground-truth value is expected due to the presence of noise. Section A.2 presents a comparison between the matching when using an optimization procedure over synthetic datasets with and without noise.

The results obtained from the given dataset indicate that there are direct correlations between certain pairs of parameters. For instance, when considering a pair of parameters such as SF and n_w, it was observed that values in their upper region tend to

occur together more often. Similarly, the same holds for both parameters in the lower region. In addition, strong correlations were observed for Corey's parameters. More specifically, the phase exponent and phase endpoint of Corey's model are correlated (n_w and k^0_{rw} present a positive correlation, as well as n_g and k^0_{rg}). Correlations for other datasets are detailed in Section A.3.

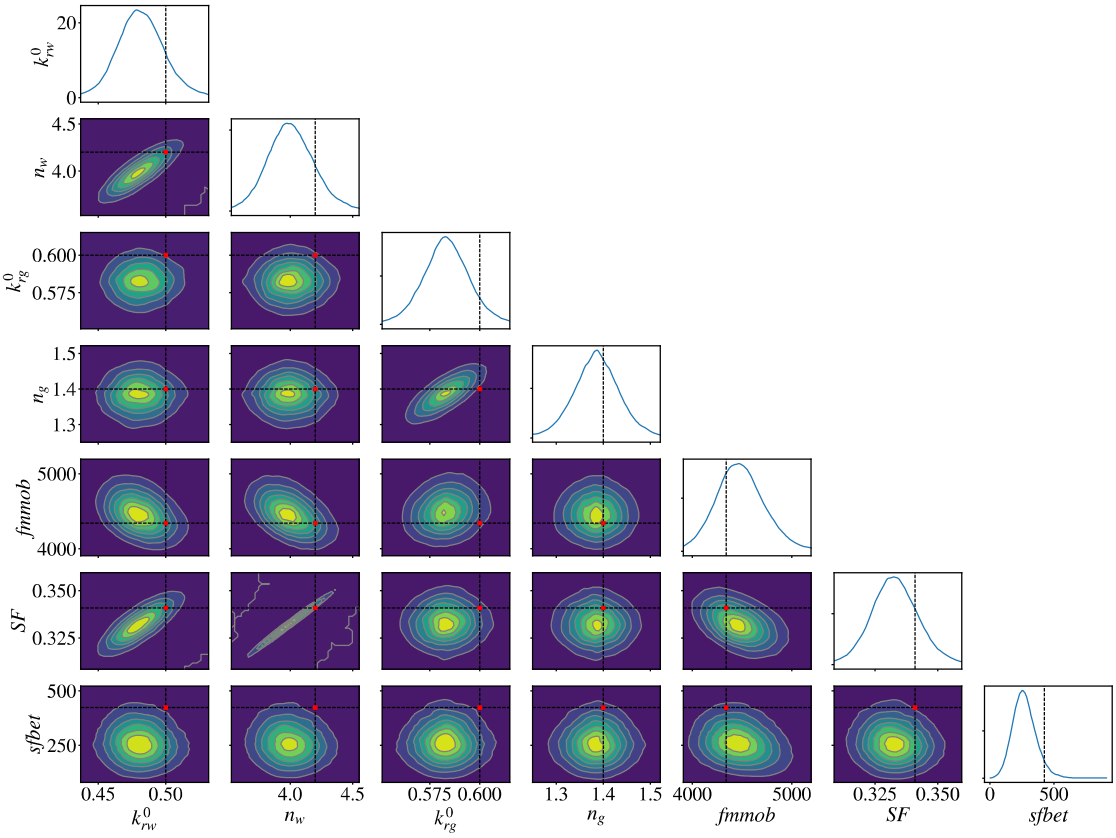

Figure 10 – Pair plot of joint distributions approximated by a multivariate Kernel Density Estimation (KDE) over the posterior distributions. Red squares indicate the ground-truth value on the joint plot over the crossed dashed lines. The plot also displays marginal densities on the main diagonal for each parameter.

Table 5 shows the median and standard deviation from the posterior distribution of each parameter obtained after the inverse UQ, which can be compared to the ground-truth parameter value also reported. It can be noted that the Bayesian inference provides an accurate estimation (based on the median) for all parameters, with the exception of the *sfbet* parameter, which is within a 90% of the credible interval of the posterior.

Table 5 – Comparison between the ground-truth value and the median values and deviation of each posterior distribution achieved.

	Median ± Standard Deviation						
Parameter	*fmmob* ($\times 10^3$)	*sfbet* ($\times 10^2$)	*SF* ($\times 10^{-1}$)	k^0_{rw} ($\times 10^{-1}$)	k^0_{rg} ($\times 10^{-1}$)	n_w ($\times 10^0$)	n_g ($\times 10^0$)
Real	4.341	4.240	3.409	5.000	6.000	4.200	1.400
Estimated	4.467 ± 0.26	2.624 ± 0.91	3.325 ± 0.10	4.809 ± 0.19	5.830 ± 0.13	3.998 ± 0.20	1.385 ± 0.05

3.5.2 Steady-State Foam Model

The uncertainties obtained for the parameters, as presented in Figure 11, were propagated to the relative permeability model given by Eq. (3.4) and to the steady-state STARS foam model described by Eqs. (3.7)-(3.9) using the classical Monte Carlo method. Figure 11 presents the propagated uncertainties to the relative permeabilities and foam apparent viscosity in terms of the mean value and of a 5%-95% prediction interval. The results show that the data aligns well with the prediction interval, considering the uncertainties from the input parameters.

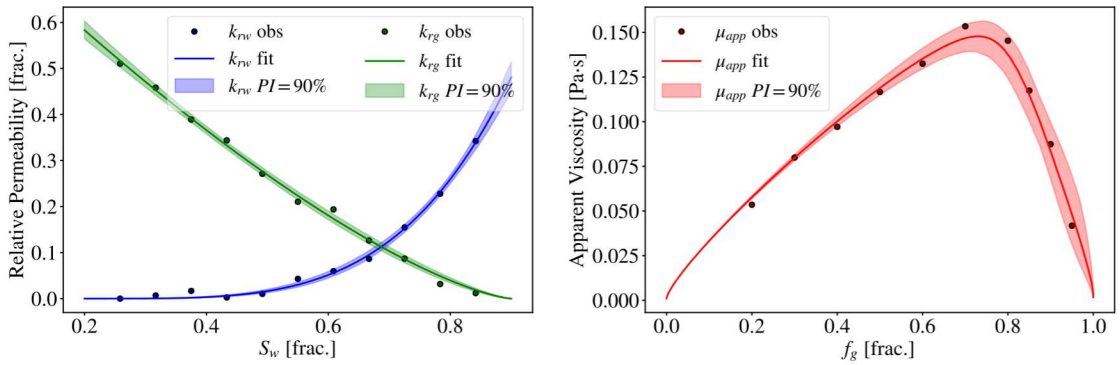

Figure 11 – Propagated uncertainties from input parameters to relative permeability and foam apparent viscosity. Each color represents one quantity, while the solid line represents the mean value, and the shaded region represents the corresponding 90% prediction interval.

To conduct the sensitivity analysis, a credible interval of 90% is considered for the posterior distributions, and the values in this range are sampled using Saltelli's extension of the Sobol sequence (Campolongo et al., 2011; Saltelli, 2002). The bounds used in the SA are presented in Table 6.

Table 6 – Intervals of the parameters, corresponding to a 90% credible interval from the posteriors, used to carry out the Sensitivity Analysis.

	Boundaries	
Parameter	Lower	Upper
k_{rw}^0	4.526×10^{-1}	5.129×10^{-1}
n_w	3.691×10^{0}	4.344×10^{0}
k_{rg}^0	5.628×10^{-1}	6.036×10^{-1}
n_g	1.300×10^{0}	1.472×10^{0}
$fmmob$	4.079×10^{3}	4.923×10^{3}
SF	3.169×10^{-1}	3.496×10^{-1}
$sfbet$	1.293×10^{2}	4.286×10^{2}

For both relative permeability and steady-state foam models, a sensitivity analysis via Sobol indices was conducted. The results in terms of main and total Sobol indices are presented in Figure 12. For the relative permeability, the sensitivities are presented as

a function of water saturation, whereas for apparent viscosity, it is given as a function of foam quality (f_g). Based on the sensitivities of the relative permeabilities, it can be observed that the exponent parameter for gas and the water end-point parameter are more relevant in the region of high water saturation. Conversely, in regions of lower water saturation (and higher gas saturation), sensitivity is governed by the exponent parameter for water and the gas end-point parameter. This is a predictable outcome, as the endpoint parameters represent the maximum relative permeability of a given phase, which decreases to zero as saturation levels decline.

The sensitivities for foam apparent viscosity indicate that the *fmmob* parameter predominates in the low-quality regime, with no significant high-order interactions (as represented by the total Sobol indices). However, in the high-quality regime, one can observe that not only SF and n_w are more relevant, but they also exhibit strong high-order interactions, as indicated by the total Sobol indices (when these indices exceed the main indices). These findings underscore the significant impact of the water-relative permeability model on foam strength within the high-quality regime. Therefore, accurately representing the water-relative permeability model is imperative for reliable foam simulations. Section A.3 includes studies using synthetic datasets that exhibit different wettability behaviors. These studies encompass the entire workflow, from inverse UQ to sensitivity analysis, and the results align with those presented here.

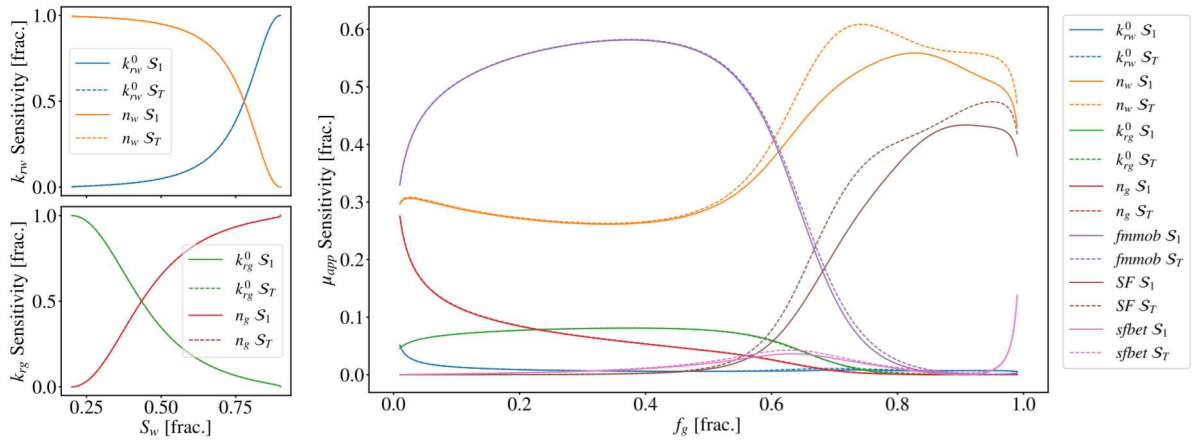

Figure 12 – Main and total Sobol indices for relative permeability functions (left) and for the apparent viscosity as a function of foam quality (right).

3.5.3 Quality Scan Simulation

Here, we present a case study that represents a core-flooding simulation, known as a foam quality-scan experiment, by solving the governing PDEs described by Eqs. (3.1)-(3.2). The computational domain consists of a block extending from 0 to $0.1538m$ in the x-direction and 0 to $0.000475678m$ in the y-direction to match the area of a circular cross-section of diameter $0.02461m$ as Pedroni (2017) core sample. The domain is discretized

into a grid of 100 cells in the x-direction and a single cell in the y-direction. A constant absolute permeability of 66 mD and porosity of 0.1091 are considered. Phases' viscosity and residual saturations are given in Table 3. The boundary conditions for the Darcy equations are applied to describe an injection process from the top to the bottom of the domain. The following fractional flows were used: $f_g = \{0.2, 0.3, 0.4, 0.5, 0.6, 0.7, 0.8, 0.85, 0.9, 0.95\}$, as in the steady-state case.

To facilitate the analysis of this case, PCE-based surrogate models were employed to solve the time-consuming partial differential equations. Pressure drop was taken as the quantity of interest at several time steps in the numerical solution. The surrogate models were constructed using a total of N samples, as given by Eq. (3.17), where $p = 7$ (number of randomized parameters) and $d = 3$ is the polynomial degree, resulting in 120 simulations to be carried out using the `FOSSIL` simulator. To evaluate the accuracy and reliability of the emulator, the Leave-One-Out (LOO) cross-validation was employed. Figure 13 demonstrates the accuracy of the emulator in terms of the pressure drop (ΔP), which shows for the samples out of the training process its true value ΔP_{FOSSIL} computed by the `FOSSIL` simulator and the corresponding approximation obtained by the PCE, which is denoted by ΔP_{PCE}. It is worth noting that the PCE-based emulator accurately predicts the response (pressure drop) with high precision, as confirmed by the computed coefficient of determination of $R^2 = 0.998$. In addition, by distinguishing between low- and high-quality regimes, one can observe that for the cases in the low-quality regime, the PCE shows better agreement due to lower uncertainty than in the high-quality regime (see Figure 13).

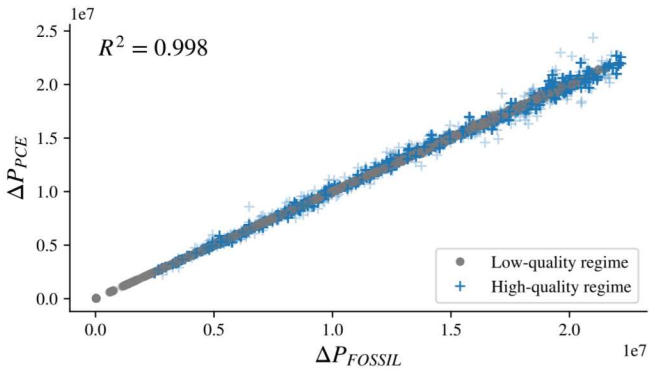

Figure 13 – Accuracy of the emulators via a Leave-One-Out (LOO) strategy and the corresponding coefficient of determination (R^2).

Figure 14 shows the predictions obtained by the PCE-based emulators of the pressure drop as a function of time. The dashed line represents the median, whereas the shaded region represents the 90% prediction interval. One can observe that for each fractional flow simulated, the uncertainties in this transient case are compatible with the ones obtained for the steady-state case, where more uncertainty is obtained in the high-quality regime, as shown in Figure 11. This indicates that uncertainties do not increase

directly with time, but rather as a function of the underlying physical phenomenon in a high-quality regime.

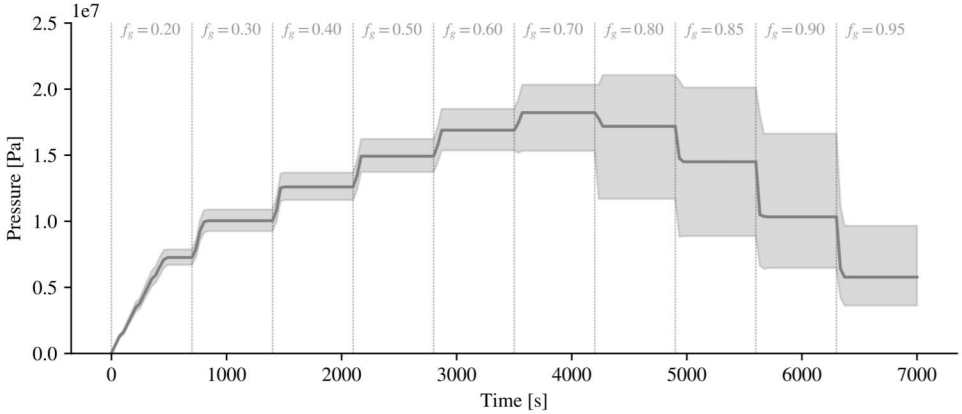

Figure 14 – Uncertainties in pressure drop as a function of time obtained by the PCE-based emulator. The solid line represents the median, while the shaded region is the 90% prediction interval.

The results of the sensitivity analysis are presented in Figure 15. The temporal behavior of the sensitivity indices suggests that foam effects parameterization does not significantly impact the outcomes until the gas flow reaches a steady state. Furthermore, the contributions of each parameter in the output's sensitivity are almost equally significant in fraction magnitude for all foam quality plateaus. For instance, at the transition where $f_g \approx 0.6$ and $t \approx 2800s$, the *fmmob* influence for both QoIs - apparent viscosity and pressure drop - decreases from almost 0.6 baselines to a little above 0.4, encountering the n_w contribution. Subsequently, in the regime transition, where $f_g \approx 0.7$, the n_w influence increases to a fraction of 0.6 of the sensitivity, with indications of strong interactions with *SF* by its total index.

Notice that the sensitivity indices for pressure drop closely align with the sensitivity of μ_{app} as illustrated in Figure 12 when f_g is continuously varied. However, in the current study, the sensitivity indices for pressure drop are presented as a function of time.

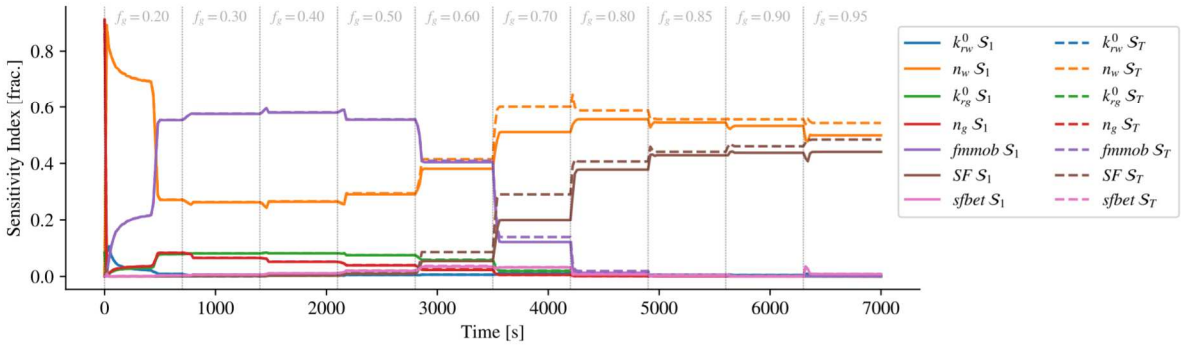

Figure 15 – Sobol indices for pressure drop over time.

3.5.4 Breakthrough Time

A new set of simulations was conducted to assess the uncertainties and sensitivities associated with the breakthrough time (BT). The breakthrough time, that is, the time it takes for the gas phase to reach the reservoir's end, is a revealing parameter of the recovery process's effectiveness. Unlike the previous foam quality-scan simulations, here, a single fixed foam quality is prescribed to evaluate the sensitivity of the breakthrough time. Ten different values for the foam quality injection, ranging from 0.20 to 0.95, were used, resulting in ten sets of simulations. Each simulation used the same setup and initial conditions as the previous case, despite the fixed f_g used for injection, and was carried out for a sufficiently long time to observe the breakthrough. The analyses of the BT again were aided by PCE emulation employing the same parameter boundaries presented in Table 6.

The uncertainties for breakthrough time are presented in Figure 16 for each injection condition. To obtain the distributions for each BT, a PCE emulator was constructed for each case, and then the input parameters were sampled to approximate BT. One can observe that, besides reducing the time to reach the breakthrough, its variance also decreases as the foam quality increases.

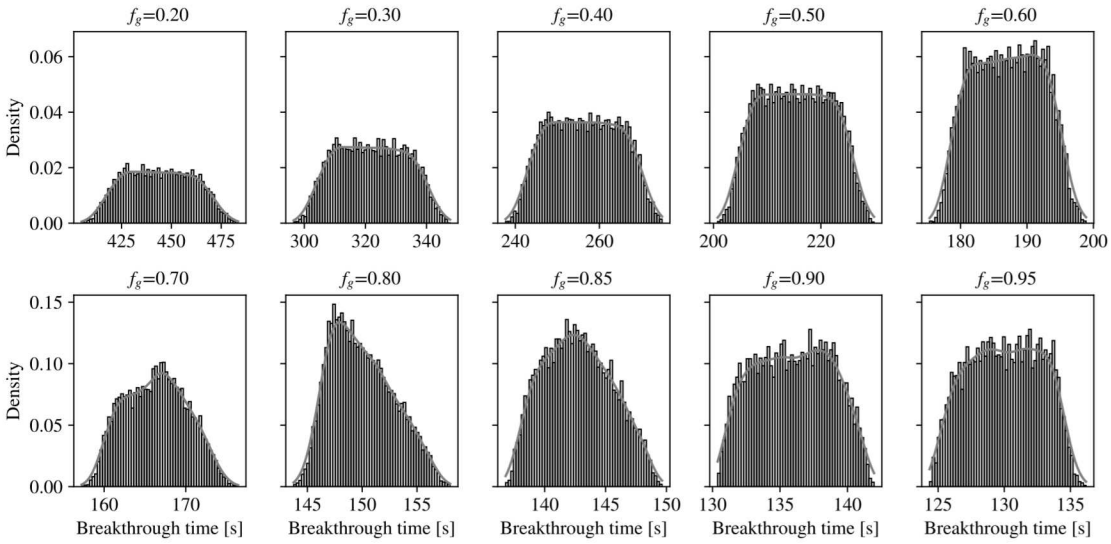

Figure 16 – Propagation of uncertainties for the BT using PCE for each different foam quality. Breakthrough times are given in seconds.

Figure 17 shows the results of the sensitivity analysis of the BT using the PCE emulators. The sensitivity of the breakthrough time in the low-quality regime region is governed by the parameter n_w for all f_g values, with negligible contributions from other parameters with sensitivities smaller than 0.1 (notice that Figure 17 uses a log scale in the y-axis). The foam parameters of STARS used in this study were found to have little impact on the breakthrough time in the low-quality regime. However, in the high-quality regime, *SF* is the most significant input parameter, and *sfbet* also increases its contribution. The

parameter *fmmob* exhibited a continuous decrease in importance as foam quality increased across the different cases, initially ranking as the second most important parameter and eventually becoming almost insignificant in the high-quality regime.

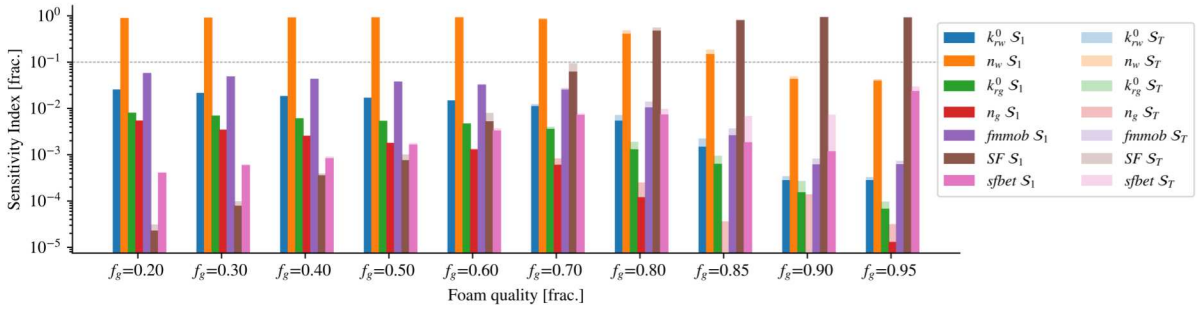

Figure 17 – First and Total Sobol Indices for the breakthrough time simulated at different foam quality injections. y-axis is presented at a log scale to detail the variance, also for parameters with low contributions.

To deepen the SA results and provide an understanding of the effects of relative permeability and foam parameters on BT, we further evaluated three representative cases ($f_g = \{0.5, 0.8, 0.9\}$) using the Shapley additive explanations (SHAP) (Lundberg and Lee, 2017; Zhou et al., 2021) to explain how the output of the model (PCE-based) is affected. The horizontal axis of the plots represents the degree of impact of a feature (input parameter) on the model's prediction of the breakthrough time. Values to the right indicate a stronger positive impact, while values to the left indicate a stronger negative impact. The color bar displays how the feature's value affects the model's prediction. The results indicate that an increase in n_w or *SF* leads to a shorter gas breakthrough time. Conversely, as expected due to its representation of maximum mobility reduction, increasing *fmmob* increases breakthrough time, making foam more efficient in mobility control. It is worth noting that overestimating n_w or *SF* can lead to an underestimation of foam performance, and vice versa. Hence, it is crucial to accurately determine these parameters for effective evaluation of foam performance.

3.6 DISCUSSIONS

Previous studies conducted by Valdez et al. (2021) and de Miranda et al. (2022a,b) have focused on assessing uncertainties in foam models in steady-state, while others Valdez et al. (2020); Berg et al. (2021b) explored the separated effects of foam parameters or relative permeability. In this chapter, sensitivity analysis highlights the importance of considering the interactions between the mathematical representation of foam flow modeling and other model components, specifically a foam implicit-texture model together with the Corey-Brooks relative permeability model, when evaluating foam flow modeling. Based on the results of core flooding simulations conducted in the presence of foam, it is clear that the water relative permeability exponent, denoted as n_w, has a crucial impact

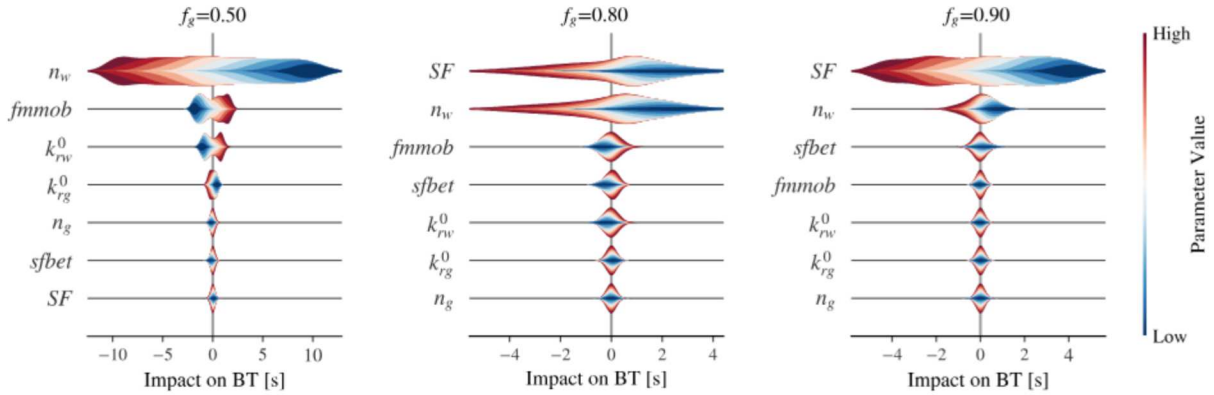

Figure 18 – Comparison of three simulations with fixed foam quality - low, transition, and high-quality regimes. The plot shows feature impact on model prediction, with x-axis indicating positive or negative impact on the breakthrough time and the color bar representing feature value impact.

on foam simulation. It exhibits significant interactions with the critical water saturation, represented as *SF*, in determining the sensitivity of the foam strength.

Our results showed that the uncertainty in pressure drop increases in the high-quality regime. The propagation results, together with the sensitivity analysis, show that accurate estimations for *SF* and n_w are crucial for high-quality regime simulations. The most significant factors for the interval agree with the previous result using the steady-state fractional flow theory. The most influential parameters in low-quality are *fmmob* followed by n_w, while in the high-quality regimes are *SF*, n_w, and their interactions.

The results for breakthrough time showed that parameters *SF* and n_w still figure as main parameters on its variance, but now intercalating which one has the main impact on the sensitivity, depending on the foam quality used for injection. It is worth noting that as the injected gas increases, the breakthrough time naturally decreases due to the increased presence of gas in the medium. Also, note that the sensitivity for a single foam quality is independent of other injections in the breakthrough analyses. The breakthrough time sensitivity analysis reveals the importance of the water's relative permeability exponent, with the understanding that when it increases, the breakthrough time also increases. Higher values of n_w result in lower values of the water relative permeability for intermediate water saturations, consequently reducing water velocity. For a fixed total velocity, it increases the velocity of the gas. Therefore, the parameter n_w plays a crucial role in obtaining reliable representations of foam flow, particularly at low gas injection rates.

3.6.1 Correlation of Parameters

The correlation between *SF* and n_w stems from their complementary effects on fluid mobility in porous media. The exponent n_w governs the degree of nonlinearity in the water's relative permeability, with higher values indicating a sharper decline in permeability

as water saturation decreases. Conversely, as water saturation increases, a higher n_w results in a more pronounced increase in relative permeability, reflecting a stronger nonlinear relationship between water saturation and permeability. The *SF* foam parameter represents the critical water saturation below which foam loses effectiveness in controlling gas mobility. Together, these parameters affect total mobility in contrasting ways. A higher n_w significantly reduces water permeability at low- and mid-range saturations, resulting in decreased overall mobility. In contrast, a higher *SF* value indicates that more water is necessary to achieve maximum foam effectiveness, which increases overall mobility. This interplay is clearly demonstrated by their impact on the system's total mobility, as expressed in Eq. (3.7) with mobilities defined in Eq. (3.3).

Figure 19 illustrates the impact of varying n_w and *SF* on apparent viscosity, comparing the results with the synthetic data from Section **3.5.1**. When these parameters vary inversely, the apparent viscosity deviates significantly from the observed values. For instance, higher values of n_w and smaller values of *SF* result in an apparent viscosity curve exceeding the observed data. On the other hand, lower values of n_w and higher values of *SF* result in an apparent viscosity that is lower than the observed data.

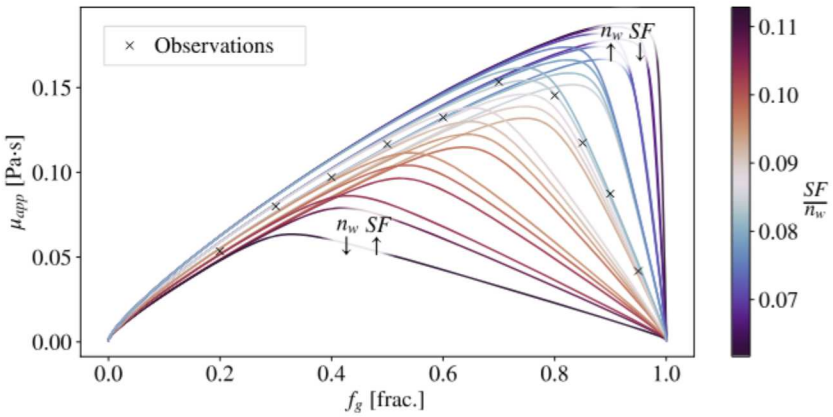

Figure 19 – Analysis of the effects of varying parameters n_w and *SF* on apparent viscosity. The color bar illustrates the magnitude differences by the ratio between *SF* and n_w.

In addition, it is important to note that the correlations for n_w (relative permeability) and *SF* (foam) parameters corroborate with Sobol indices results, which indicates that the parameters' interplay is stronger at higher foam qualities (see Figure 12).

Notice that the correlation between Corey's exponents and endpoint parameters is expected due to their roles in the relative permeability curve geometry of each phase. An increase in $k^0_{r\alpha}$ shifts the curve upward, while increasing n_α steepens it. Conversely, a decrease in these parameters produces a similar but opposite effect, with lower values of $k^0_{r\alpha}$ shifting the curve downward and reduced n_α resulting in a more gradual slope. Proportional increases in both parameters tend to counterbalance and maintain a good fit between the curve and the data, resulting in high likelihood values. In addition, we

highlight that the likelihood function based on apparent viscosity and relative permeability observations may also contribute to the correlations between $k^0_{r\alpha}$ and n_α.

3.6.2 Relative Permeability Models

Alternative models for describing relative permeability, such as LET (Lomeland et al., 2005), may offer more flexibility than the traditional Corey model, as it exhibits a high level of agreement with experimental data across a wide saturation range. However, the increased number of LET model parameters introduces greater uncertainty (Valdez et al., 2020). In addition, Berg et al. (2021a) noted that while the LET model's additional degrees of freedom allow for a better description of the data, it remains a phenomenological parameterization with empirical parameters that lack physical interpretation, including cross-correlations of fit parameters. Moreover, when accounting for foam representation, the LET model does not allow for direct observation of water saturation in steady-state from the foam quality scan, unlike Corey's model (Kapetas et al., 2015). That is why, in the present chapter, we used Corey's model, as it is a widely used empirical approach to model the relative permeability curves of two-phase flow in porous media, probably the most used model for foam flow modeling (Kovscek and Radke, 1994; Ma et al., 2014a; Kapetas et al., 2015; Almaqbali et al., 2017; Tang et al., 2019b; Ding et al., 2020a; Tang et al., 2022). Nevertheless, the computational analysis presented in our work can be extended to other models, such as LET.

3.6.3 Limitations

This study focused on analyzing two distinct parameterizations of the model's components: the `STARS` foam implicit-texture representation, which accounted solely for water saturation effects, and the Corey-Brooks relative permeability model. Although the interaction between the two models affecting foam strength has been significant, in order to obtain a more comprehensive understanding of the model's reaction, it is necessary to consider a broader study that takes into account the interactions between different representations of foam texture and how other physics, such as capillary pressure, could influence the model response.

In this work, we are primarily concerned with quantifying uncertainties arising from laboratory-derived parameter fitting in foam modeling. Our approach utilizes one-dimensional simulations as an *in silico* experimental framework to elucidate the potential variability in foam performance predictions at the core sample scale. While this approach provides valuable insights into parameter sensitivity, it is important to acknowledge its limitations. The simplified nature of our approach does not fully encapsulate the complex phenomena encountered at the field scale, such as heterogeneity, multi-dimensional flow, and long-term dynamic processes. Therefore, the uncertainty analysis results should be

interpreted within the laboratory context, taking into account important considerations for future research that bridge laboratory findings with field-scale applications.

In addition, as highlighted by Patzek and Myhill (1989) and Hirasaki (1989), the significantly slower propagation of foam compared to surfactants in field applications reveals complexities and uncertainties that are not fully captured by laboratory experiments and one-dimensional simulations. This observation highlights the challenges in accurately scaling laboratory data to field conditions, where additional factors influence the behavior of foam. Patzek (1996) further underscores the importance of carefully considering the scaling characteristics of foam dynamics, such as bubble growth and collapse, surfactant types, injection strategies, and reservoir architectures when extending lab-based models. These scaling issues introduce additional layers of uncertainty, complicating the task of accurately matching mathematical models to experimental data and predicting field-scale performance (Bertin et al., 1999).

Nevertheless, core flood data are primarily used to calibrate the parameters of the foam implicit-texture model and to determine relative permeability, as demonstrated in previous studies, such as Alcorn et al. (2022) and Vieira et al. (2024). We aim to investigate how these calibration procedures introduce uncertainties and how they can impact key quantities of interest, as well as the overall foam flow, despite the differences between core flood modeling and field-scale applications.

3.7 CONCLUSIONS

This work presented an inverse uncertainty quantification approach comprehending both relative permeability and foam parameters to enable parametric uncertainty propagation and sensitivity analysis evaluation for a foam flow model in porous media. A new strategy is proposed to define and incorporate prior knowledge about non-observable parameters into the Bayesian inference for foam parameters. By using a noisy synthetic dataset and an algebraic model employing fractional flow theory, posterior distributions were achieved via Bayesian inference, comprising their respective ground-truth values. Following this inverse uncertainty quantification step, uncertainty propagation and sensitivity analysis were carried out to evaluate the algebraic steady-state and the transient PDE model against the data. Additionally, PCE-based surrogate models were employed to represent the outputs of the transient foam flow simulator for different experimental setups.

The main findings of this work rely on the simultaneous estimation and uncertainty characterization of relative permeability and foam model parameters, as well as their interplay. The proposed approach achieved a reasonable match between the model and the reference dataset with noise, as well-defined posterior distributions were obtained for all model parameters through Bayesian inference. In addition, the results also revealed a

significant correlation and interplay between foam and relative permeability components of the flow model.

The estimated uncertainties were propagated to the outputs of algebraic steady-state and transient PDE models based on the local equilibrium approach for foam flow. Limited uncertainty, which comprehends the experimental data synthetically generated, was observed for both cases, which are also compatible between the two models. Results of the Sobol sensitivity analysis on both models also revealed a good agreement in terms of the impact of each input parameter on the outputs, where it was found that the *fmmob* (foam) and n_w (relative permeability) parameters are the more relevant ones for pressure drop and apparent viscosity in the scenario studied. The analysis of the breakthrough time revealed that the water exponent n_w and the *SF* foam parameter have a significant impact on this quantity of interest, indicating another interesting interplay between these two components of the model. The sensitivity results for the breakthrough time indicate that accurately determining n_w or *SF* is crucial for evaluating foam performance precisely. Finally, it was demonstrated that the polynomial chaos expansion is an efficient approach for surrogate models of transient foam flow dynamics, enabling computationally expensive uncertainty quantification and sensitivity analyses.

4 MODELING FOAM FLOW IN POROUS MEDIA INFLUENCED BY OIL

This chapter presents the paper de Miranda et al. (2025b) submitted for consideration of publication entitled "*Modeling Foam Flow in Porous Media Influenced by Oil: A Computational Framework for Improved Parameter Estimation*", which develops a computational framework to estimate foam parameters in the presence of oil using systematic core flooding protocols with progressive oil injection.

4.1 INTRODUCTION

In gas-assisted enhanced oil recovery (EOR) projects, foam represents a strategic approach to overcome significant reservoir challenges by reducing gas mobility and improving sweep efficiency (Kovscek and Radke, 1994; Farajzadeh et al., 2012). When deployed in heterogeneous reservoirs, foam creates flow resistance by trapping gas in a network of liquid lamellae, redirecting injected fluids toward unswept zones, and mitigating viscous fingering and gravity override phenomena (Bello et al., 2023b). The effectiveness of foam-assisted recovery relies on its rheological properties and its stability under reservoir conditions, highly impacted by the presence of crude oil and the scarcity of water (Talebian et al., 2014; Bello et al., 2023b).

Numerical models are often employed during foam-based EOR processes to evaluate their feasibility, predict production performance, and assess carbon dioxide (CO_2) storage capacity (Paula et al., 2022; Lyu et al., 2021a). In these applications, the accurate simulation of complex fluid flows is frequently limited by the approximations introduced through mathematical modeling or numerical methods and by uncertainties in model parameters. Important model parameters such as relative permeability, capillary pressure, and foam-related properties are typically estimated through calibration procedures using core flooding experiments (Berg et al., 2024). While there are several research studies on experimental procedures and methods to determine foam parameters related to the effects of water saturation, shear-thinning behavior, surfactant concentration, and other factors (Boeije and Rossen, 2013; Ma et al., 2014a; Valdez et al., 2021; Zeng et al., 2016), fewer studies address the issue of estimating parameters related to the effects of oil on foam.

The impact of oil is often assessed with steady-state foam–oil co-injection experiments, which typically involve either fixing the oil injection rate while varying the gas fraction, or simultaneously varying both the oil and gas fractions (Amirmoshiri et al., 2018; Da et al., 2018; Chen et al., 2018; Tang et al., 2019c; Jian et al., 2019; Hussain et al., 2019; Vieira et al., 2024; Jia et al., 2024). In particular, Tang et al. (2019d,a,c) demonstrated that oil effects on foam can be assessed through co-injection experiments conducted at

fixed ratios of oil-water superficial velocity. This protocol enables direct quantification of oil effects on foam behavior. Regarding the estimation of oil-related parameters, one of the few studies in this area was conducted by Lyu et al. (2021b), who applied a non-linear least-squares minimization approach to fit foam parameters using data from a single foam quality-scan experiment. However, their method aimed to simultaneously capture the effects of water saturation, shear-thinning behavior, and the presence of oil on foam using a single experimental dataset. Despite these efforts, a systematic understanding of the experimental data required to reliably estimate oil-related foam parameters, particularly with reduced uncertainty, remains largely unexplored in the literature.

To address this gap, the study employs a computational framework based on numerical simulations to replicate core flooding experiments that are used for characterizing foam properties in implicit-texture models. The main contribution of this work is a systematic evaluation of the approach used to estimate foam parameters from experiments commonly employed to assess oil effects on foam, with the goal of obtaining more reliable estimates and reducing uncertainty. Therefore, this work demonstrates that oil-related parameters can be extracted from experiments already commonly used in the literature. In addition, we assess the impact of limited data availability and analyze how uncertainties in foam model inputs propagate to key quantities of interest, such as oil and gas production. Additionally, we investigate how variations in estimated oil-related parameters affect predictions from numerical simulations of three-phase flow with foam, including scenarios with oil-bank formation and complex two-dimensional heterogeneous reservoirs. The computational framework and results of this work can support the refinement of injection strategies and measurement techniques to better isolate oil effects on foam, enabling more accurate interpretation of experimental data for model parameter calibration. This approach helps reduce parametric uncertainty and ultimately improves predictive models for field-scale foam applications.

The remainder of this work is organized as follows. Section 4.2 presents the governing equations for three-phase flow in porous media and the foam model used in this study, with particular emphasis on the systematic and novel workflow for characterizing foam parameters through numerical simulations. Section 4.3 describes the numerical implementation of the three-phase flow simulator and the Bayesian inference techniques for parameter estimation. Section 4.4 presents the results, including the generation of synthetic experimental data, estimation of oil-related foam parameters, uncertainty quantification analysis, and evaluation of parameter impacts through two-dimensional heterogeneous simulations. Section 4.5 discusses the implications of the findings and the limitations of current experimental protocols, while Section 4.6 presents the conclusions.

4.2 METHODS

Next, we present the governing equations for multiphase flow in porous media, accounting for the oil, water, and gas phases in the presence of foam, as used in the numerical simulations. We then introduce the proposed parameter estimation approach for determining oil-related foam parameters.

4.2.1 Fractional Flow Formulation

The three-phase flow of water, oil, and gas in a porous medium is governed by mass conservation equations for each phase, along with a Darcy-like equation that defines phase velocities. Following Tang et al. (2019a), the phases are assumed to be incompressible and immiscible. For simplicity, gravity and capillary pressures are neglected. Phase saturations are denoted by S_α with velocities u_α, where $\alpha \in \{w, o, g\}$ corresponds to water, oil, and gas phases. Then, the governing equations are given by:

$$\phi \frac{\partial S_\alpha}{\partial t} + \nabla \cdot u_\alpha = 0, \quad \text{in } \Omega \times [0, T], \tag{4.1}$$

$$u_\alpha = -\mathrm{K}\, \lambda_\alpha \nabla p_\alpha, \quad \text{in } \Omega, \tag{4.2}$$

with the phase mobility given by

$$\lambda_\alpha = \frac{k_{r\alpha}}{\mu_\alpha}, \tag{4.3}$$

where $k_{r\alpha}$, μ_α, and p_α denote the relative permeability, viscosity, and pressure of phase α, ϕ is the porosity, and K is the absolute permeability.

The relative permeabilities $k_{r\alpha}$ are described by the Brooks-Corey model (Brooks and Corey, 1963) for three-phase flow. Without considering foam effects, they are given by:

$$k_{rw} = k_{rw}^0\, s_w^{n_w}, \qquad k_{ro} = k_{ro}^0\, s_o^{n_o}, \qquad k_{rg} = k_{rg}^0\, (1 - s_w - s_o)^{n_g}, \tag{4.4}$$

with the normalized saturations defined by

$$s_w = \frac{S_w - S_{wc}}{1 - S_{wc} - S_{or} - S_{gr}}, \qquad s_o = \frac{S_o - S_{or}}{1 - S_{wc} - S_{or} - S_{gr}}, \tag{4.5}$$

where n_w, n_o, and n_g are the Corey exponents and S_{wc}, S_{or}, and S_{gr} denote connate water, residual oil, and residual gas saturations.

The fractional flow of a phase α is defined as the ratio of the phase velocity to the total velocity of all phases flowing through the porous medium:

$$f_\alpha = \frac{u_\alpha}{u_T}, \quad u_T = \sum_\alpha u_\alpha, \tag{4.6}$$

where u_T is the total superficial velocity. Under conditions of fixed injection velocity in a core flooding experiment, a steady state is eventually reached, and a constant pressure

difference across the core is established (Welge, 1952; Rossen, 1996; Tang et al., 2019b). At this steady state, the apparent viscosity of the fluid system can be calculated. The apparent viscosity, defined as the inverse of the total mobility λ_T in experimental settings, is calculated as:

$$\mu_{app} = \lambda_T^{-1} = \frac{\mathrm{K}}{|u_T|}\frac{\Delta p}{L}, \tag{4.7}$$

where Δp is the pressure drop (measured between the outflow and the core injection), and L is the core length.

At steady state, the fractional flow of each phase can also be expressed mathematically as the ratio of its mobility to the total mobility, that is:

$$f_\alpha = \frac{\lambda_\alpha}{\lambda_T} \quad \Longrightarrow \quad k_{r\alpha} = \frac{\mu_\alpha\, f_\alpha}{\mu_{app}}. \tag{4.8}$$

In addition, Eq. (4.8) also establishes a direct expression to determine relative permeability from experimentally measurable quantities: the injected fractional flow (f_α), phase viscosity (μ_α), and apparent viscosity (μ_{app}). This relation forms the basis for analyzing foam effects on fluid mobility in porous media.

4.2.2 Foam Model

Few mechanistic foam models explicitly account for the effects of oil on foam behavior (Myers and Radke, 2000; Ma et al., 2018; Zhao et al., 2022). In contrast, implicit-texture models offer advantages in terms of both efficiency and simplicity, and can be calibrated to experimental data to reproduce observed outcomes. The widely used commercial simulator for foam flow, `STARS` (CMG, 2019), employs an implicit-texture of foam and is adopted in this study. This model employs a mobility reduction factor (MRF) to describe foam effects, which is introduced into the gas mobility as follows:

$$\mu_{app} = \left(\lambda_w + \lambda_o + \frac{\lambda_g}{MRF}\right)^{-1}, \qquad MRF = 1 + fmmob\prod_i F_i, \tag{4.9}$$

where F_i are factors modeling physical phenomena with impacts on the foam texture. In this work, following Lyu et al. (2021b), only the terms F_{dry} and F_{oil}, which describe the effects of water and oil saturation on foam performance, are considered:

$$F_{dry} = \frac{1}{2} + \frac{1}{\pi}\arctan(epdry(S_w - fmdry)), \tag{4.10}$$

$$F_{oil} = \begin{cases} 1, & S_{or} \le S_o \le floil, \\ \left(\frac{fmoil - S_o}{fmoil - floil}\right)^{epoil}, & floil < S_o < fmoil, \\ 0, & fmoil \le S_o \le S_{wc} - S_{gr}. \end{cases} \tag{4.11}$$

Here, *fmmob* describes the maximum gas mobility reduction due to foam, *epdry* controls the smoothness of foam degradation caused by dry-out effects, *fmdry* approximates the

critical water saturation, below which foam collapses due to drying effects, *epoil* regulates the smoothness with which increasing oil saturation weakens foam, *floil* indicates the oil saturation point at which oil begins to weaken foam, and *fmoil* indicates the oil saturation point at which oil destroys foam.

4.2.3 Characterization of Foam Parameters

A systematic workflow for characterizing the effects of dry-out and oil on foam behavior in porous media through numerical simulations is illustrated in Figure 20. Our approach follows the steps outlined below to obtain data for foam characterization, where (E) items stand for experimental procedures and (D) items stand for computational steps for parameter calibration that integrate experimental protocols with computational modeling.

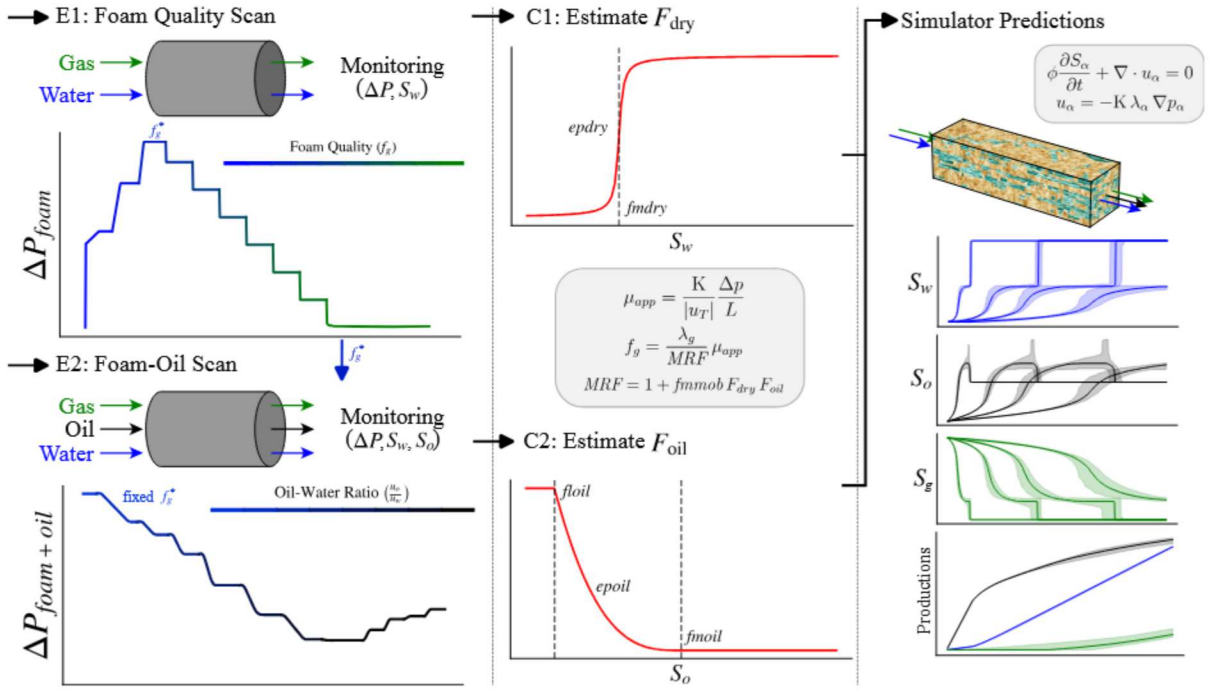

Figure 20 – Schematic representation of the workflow employed in this study: from core flooding experiments (left), through model parameter estimation (center), to uncertainty quantification (right). The left panels illustrate a foam-quality scan and a foam–oil scan, with experimental data used to characterize the effects of foam dry-out (F_{dry}) and oil-induced foam weakening (F_{oil}), respectively. The right panel depicts the uncertainty quantification stage, in which the estimated parameters and their associated uncertainties are propagated through numerical simulations.

It is important to highlight that in this work, we relied on data generated from numerical simulation of foam flow in porous media to represent the laboratory experiment (E) from which the calibration (C) to determine the parameters is conducted. The main reason for adopting this approach is that it provides control over the experimental setup and the exact parameter values used in the simulations. This enables a rigorous verification

process, allowing us to directly compare the estimated parameters with the actual values used to generate the data (synthetic data). Such conditions enable systematic evaluation of parameter estimation and uncertainty quantification, ultimately improving the reliability of methods for interpreting experimental data and calibrating foam models.

Before presenting our approach, we first consider a preliminary but essential step: performing a co-injection of water, oil, and gas into the porous medium (Oak et al., 1990; Alizadeh and Piri, 2014) to estimate the water/oil/gas relative permeabilities based on a selected model, such as the Corey–Brooks function, as defined in Eq. (4.4).

The subsequent steps define the workflow (Figure 20) for estimating foam parameters, including the effects of oil on foam behavior:

(E1) Conduct a foam quality scan using co-injection of surfactant and gas until a steady-state of each gas fraction.

(C1) Estimate foam parameters such as *fmmob* (maximum mobility reduction factor), and the ones related to dry-out effects such as *epdry* and *fmdry* using the foam quality scan data (see Eqs. (4.9) and (4.10)). Also, determine f_g^*, the gas fraction associated with the maximum pressure drop; this value represents optimal foam generation conditions and will serve as the reference point for subsequent oil injection tests.

(E2) Conduct a core flooding with coinjection of surfactant, oil, and gas at the fixed critical gas fraction f_g^* while progressively increasing the oil-water ratio (u_o/u_w) and maintaining total velocity constant throughout the experiment (see Figure 23, bottom-left panel).

(C2) Estimate foam parameters from the F_{oil} term related to the effects of oil on foam (see Figure 25).

To characterize foam parameters from Eqs. (4.9), (4.10) and (4.11), the initial step is to carry out a foam quality scan (step E1) (Moradi-Araghi et al., 1997; Ma et al., 2013; de Miranda et al., 2022b) using the co-injection of gas and water in the presence of foam. The pressure drops obtained at steady-state after this step are used to compute apparent viscosity using Eq. (4.7), which, together with the fractional flow f_g information, will allow the determination of *fmmob*, *fmdry*, and *epdry* parameters (step C1). The foam quality corresponding to the maximum apparent viscosity (and pressure drop), denoted by f_g^*, is identified after the foam quality scan and will be used in the following steps.

Next, a core flooding at a fixed gas fractional flow, f_g^*, while progressively increasing the oil-water injection ratio is conducted (step E2). This step is crucial to determine the effects of oil on foam and, consequently, estimate the oil-related parameters (step C2). To this end, the observed data at the steady state of each injection ratio u_o/u_w is used to

compute a corresponding mobility reduction factor (*MRF*). In particular, we used the following expression, described in Valdez et al. (2021), to compute the mobility reduction factor:

$$MRF = \frac{\lambda_g}{f_g} \frac{K\,\Delta P}{u_T\,L}, \tag{4.12}$$

where the use of λ_g presupposes that relative permeabilities have been previously characterized.

To ensure accurate parameter estimation for the F_{oil} term, along with the corresponding oil saturation S_o, a correction for dry-out effects must be applied. Specifically, each data point in the dataset is adjusted by incorporating F_{dry} as follows:

$$F_{oil} = \frac{1}{F_{dry}} \frac{(MRF - 1)}{fmmob}. \tag{4.13}$$

This process generates a collection of data points (S_o, F_{oil}), enabling the estimation of oil-related parameters *floil*, *fmoil*, and *epoil* (see Eq. (4.11) and Figure 25 for further details).

4.3 NUMERICAL IMPLEMENTATION

In this section, we outline the techniques employed for parameter inference and the numerical implementation details of the three-phase flow simulator used in all experiments.

4.3.1 Parameter Inference

The foam parameters to be estimated are denoted as $\boldsymbol{\theta} = \{fmmob, epdry, fmdry, floil, fmoil, epoil\}$ and appear in Eqs. (4.9), (4.10), and (4.11). Following the outlined procedure, we start by estimating the parameters related to maximum mobility reduction $fmmob$ and related to the water saturation effects *epdry* and *fmdry* are estimated using the data from the foam quality scan from Step E1. Numerous approaches have been reported in the literature for estimating the parameters that characterize dry-out effects (F_{dry} term) and the maximum reduction in foam mobility (*fmmob*), using datasets obtained from foam quality scans (Ma et al., 2014a; Boeije and Rossen, 2013; Zeng et al., 2016; Valdez et al., 2021; de Miranda et al., 2022b, 2024). In this study, these parameter values are regarded as the ground truth. This approach establishes a baseline for analysis while enabling attention to be directed toward other critical aspects of the work, the parameters related to oil effects (F_{oil} term), which shall be denoted by $\boldsymbol{\theta} = \{floil, fmoil, epoil\}$ from now on.

A Bayesian inference technique is used to estimate these parameters along with their associated uncertainties. We employ the No-U-Turn Sampler (NUTS), which is a variant of Hamiltonian Monte Carlo (Hoffman and Gelman, 2011; Salvatier et al., 2016). This method quantifies uncertainty by sampling from the posterior distribution $p(\boldsymbol{\theta}|\mathbf{y}) \propto p(\mathbf{y}|\boldsymbol{\theta})p(\boldsymbol{\theta})$ for a given quantity of interest $\mathbf{y}$, specifically the F_{oil} function in this study. Through this

approach, we generate posterior samples that facilitate uncertainty propagation and allow us to calculate credible intervals and posterior predictive distributions.

This approach quantifies parameter uncertainty by sampling from the posterior distribution. The likelihood function assumes normally distributed measurement errors with constant variance:

$$p(\mathbf{y}|\boldsymbol{\theta}) = \prod_{i=1}^{n} \frac{1}{\sqrt{2\pi\sigma^2}} \exp\left(-\frac{(y_i - f(x_i;\boldsymbol{\theta}))^2}{2\sigma^2}\right) \tag{4.14}$$

where y_i represents the observed data, $f(x_i;\boldsymbol{\theta})$ is the model prediction, and σ^2 is the measurement error variance. The following prior distributions for the parameters are used:

$$\mathit{floil} \sim \mathcal{U}(10^{-3}, 1.0), \quad \mathit{fmoil} \sim \mathcal{U}(\mathit{floil}, 1.0), \quad \mathit{epoil} \sim \mathcal{U}(10^{-2}, 10), \tag{4.15}$$

which are established based on physical constraints (*floil* and *fmoil*) or based on a reasonable large interval (*epoil*). The hierarchical constraint *floil* $<$ *fmoil* enforces the physical requirement that the oil saturation at which foam begins to weaken must be lower than the saturation at which foam completely collapses. The NUTS method is used with 5×10^4 posterior samples, 5×10^3 tuning iterations, and 4 independent chains to ensure reliable convergence. Additional details about the adopted Bayesian inference algorithm can be found in Salvatier et al. (2016).

4.3.2 Numerical Simulations

The numerical simulations used the parameters from Lyu et al. (2021b); Tang et al. (2022) to generate representative data. Table 7 presents fluid properties, relative permeabilities, and foam parameters used in the baseline simulations. To simulate the core-flooding experiments, one-dimensional simulations of three-phase flow with foam were carried out using an in-house code developed based on `OpenFOAM` (Jasak, 2009). In summary, the governing equations were solved using the IMPES (IMplicit Pressure, Explicit Saturation) method; that is, the pressure equation was solved implicitly, while saturations were updated explicitly. For more details on the formulation, see Horgue et al. (2015).

To generate data that more closely resembles experimental observations, a predefined level of noise is added to the numerical simulation results before proceeding to parameter estimation. Gaussian noise was added at 2% of the highest observed value for a quantity during the entire injection protocol, specifically to the pressure drop observations and the average saturations of water and oil. The gas saturation was calculated using this noisy data derived from the saturations of other phases.

Table 7 – Fluid properties, relative permeabilities, and foam parameters: viscosity (μ_α), residual saturation ($S_{r\alpha}$), Corey exponent (n_α), and end-point relative permeability ($k^0_{r\alpha}$).

Fluid	μ_α (Pa · s)	$S_{r\alpha}$	n_α	$k^0_{r\alpha}$	*fmmob*	*fmdry*	*epdry*
Water	1.00×10^{-3}	0.1	2.0	1.0	2000	0.3	32000
Oil	5.00×10^{-3}	0.1	2.0	1.0	*floil*	*fmoil*	*epoil*
Gas	1.00×10^{-5}	0.0	2.0	1.0	0.1	0.5	3.0

The computational domain was represented by a one-dimensional porous medium with $0.247\,m$ length, absolute permeability of 1300 mD, and porosity of $\phi = 0.25$. The mesh was discretized using 100 cells in the x direction, while the transverse directions (y, z) were resolved with 1 cell each.

4.3.2.0.1 Foam quality scan

Simulations of a foam quality scan (water/surfactant and gas) were performed with a fixed total velocity of 2.924×10^{-5} m/s while varying the foam quality f_g. Each case was simulated for 5×10^3 seconds using a time step of $\Delta t = 1$ second. Initially, for $f_g = 0.1$, the medium was fully saturated with water, disregarding the residual saturations of other phases. Subsequent simulations were initialized from the final state of the preceding case, progressively increasing f_g to assess its influence on flow regimes.

4.3.2.0.2 Core-flooding with oil injection

Simulations of core-flooding co-injecting water, gas, and oil used the same computational domain configuration and fixed total velocity. Here, the gas fraction f_g^* with the highest observed pressure drop is fixed while water and oil are injected at different ratios $\frac{u_o}{u_w}$ to evaluate the oil effects in foam. Each simulation, using a different water-to-oil ratio, is performed with a time step size of $\Delta t = 0.01s$ for at least 10^4 seconds. This period is monitored to ensure that steady-state conditions for pressure and saturation have been reached. If these conditions are not met, an additional 5×10^3 seconds is added, and the conditions are checked again until they are satisfied.

4.3.2.0.3 Heterogeneous two-dimensional simulations

To further assess the impact of parameter estimation for F_{oil}, simulations were conducted in a two-dimensional domain featuring a heterogeneous permeability field derived from layer 19 of the 10th SPE comparative project (SPE10) (Christie and Blunt, 2001), which was rescaled to a length of 3.67 m as described by Paula et al. (2022) and Cedro et al. (2025) to emphasize the structure of a realistic permeability field rather

than focusing on the challenges associated with upscaling. This layer features gradual variations in permeability magnitude which facilitate the development of preferential paths for displacement, as depicted in Figure 21. Additional details on these simulations are provided in the following section. The simulated cases were designed based on initial configurations that closely resemble those investigated by Lyu et al. (2021b). The configuration used consists of a porous medium that is initially saturated with higher initial oil saturation, $(S_w, S_o) = (0.2, 0.8)$, representing conditions typical of an early-stage EOR process.

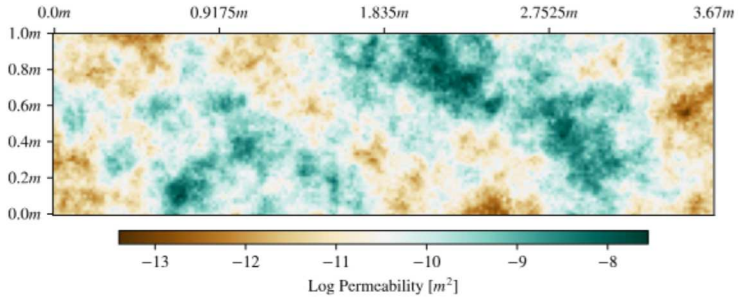

Figure 21 – Permeability field for layer 19 of the SPE10 benchmark model.

4.4 RESULTS

We begin by describing the simulations carried out to generate data representative of core flooding experiments. Then, we use this data to show how to estimate foam parameters, with a special focus on the oil-related ones. Finally, we explore different cases of the parameters to show the impacts of estimated foam parameters on 2D simulations on heterogeneous fields and evaluate relevant quantities such as production and pressure drop.

4.4.1 Generation of synthetic data from numerical experiments

First, a foam quality scan with gas and water only is simulated by varying the injected gas fraction f_g from 0.1 to 0.9 in steps of 0.1. This procedure allows for evaluating foam performance and determining the critical gas fraction f_g^* at which the maximum mobility reduction occurs. The results of this experiment are used to estimate $fmmob$ (representing the maximum mobility reduction factor) and F_{dry} parameters such as $epdry$ and $fmdry$. Figure 22 presents the pressure drop evolution for the water-gas co-injection in the computational simulation of the foam quality scan experiment. Regarding the foam quality scan protocol, the critical foam value f_g^* is unknown *a priori*. Therefore, the gas fraction corresponding to the maximum observed pressure drop is taken as an approximation of the critical foam quality f_g^* for subsequent core flooding simulations, which for this simulation is around 0.3.

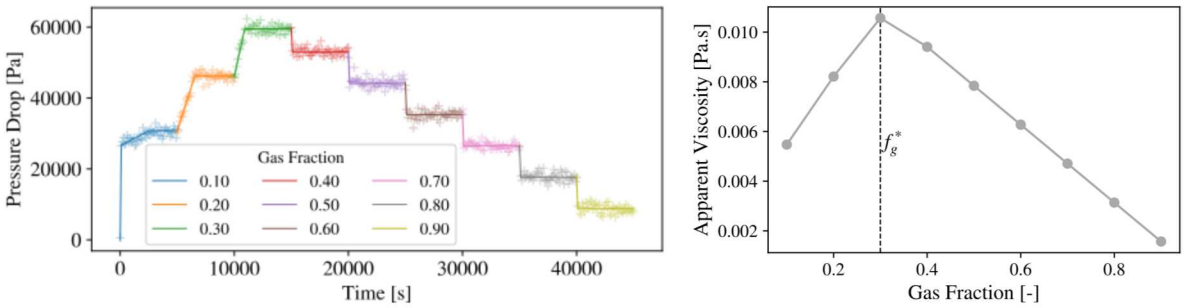

Figure 22 – Numerical simulation of foam quality-scan experiment. Left: pressure drop (with noise) along time in the foam quality scan protocol in the absence of oil. Right: steady-state values of the apparent viscosity as a function of the gas fraction f_g.

Based on the results of the foam quality scan, the parameters *fmmob*, *fmdry*, and *sfbet* can be estimated. In this study, however, these parameters are fixed at their ground truth values. Next, to evaluate the influence of oil on foam strength, oil is co-injected alongside surfactant and gas, with the oil fraction gradually increased, as described by Tang et al. (2016). The critical gas fraction (f_g^*), observed during the foam quality scan, acts as a reference point for the injection strategy. This strategy ensures a constant total velocity while progressively increasing the oil-water rate u_o/u_w, and keeping the gas fraction fixed.

Figure 23 illustrates the pressure drop recorded during this procedure and the steady-state values of apparent viscosity as a function of oil fraction, while Figure 24 presents the average saturation levels for the phases during the simulation time. Initially, it is observed that the oil injection into the core leads to a gradual decrease in pressure drop, which is attributed to a weakening of the foam strength. Further, it is possible to see that after a certain level of oil injection in the core (in our study case, the oil-water rate is around 0.16 and 0.20), the pressure drop starts to increase; this region marks where the foam is destroyed, and oil viscous forces start to decrease overall mobility, and a slight increase in pressure drop is observed.

Systems that are more vulnerable to oil damage require careful control over the oil injection process during experiments. For instance, when the upper threshold parameter *fmoil* is lowered, as discussed in Section **B.3.4**, it becomes increasingly important to monitor the gradual increase in oil injection to accurately characterize the interactions between foam and oil.

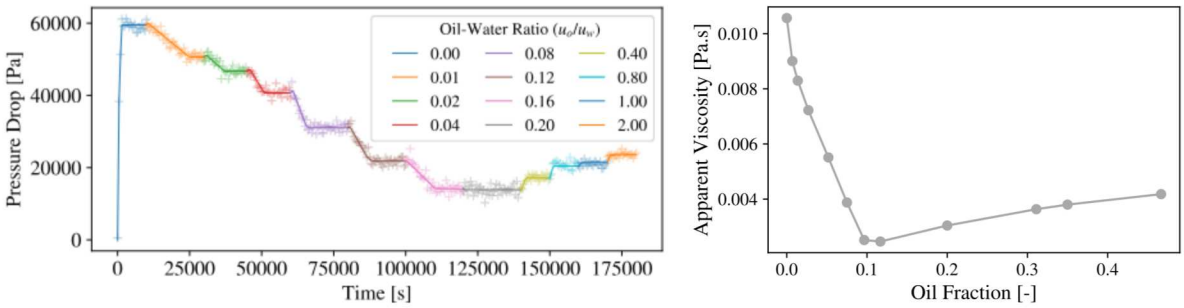

Figure 23 – Left: simulated pressure drops increasing oil injection at f_g^* and the noisy synthetic points generated. Right: steady-state values of apparent viscosity as a function of oil fraction f_o.

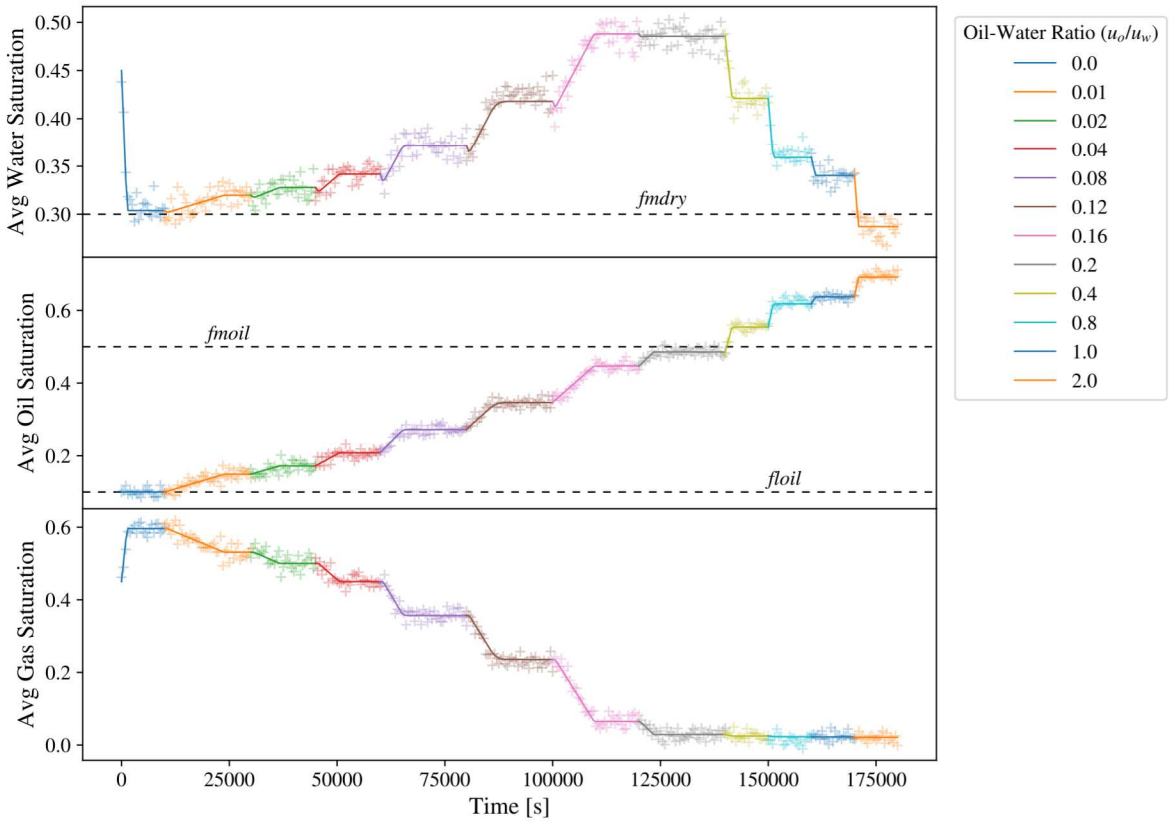

Figure 24 – Saturations of the water (top), oil (middle), and gas (bottom) phases during the simulations with increasing oil-water ratio u_o/u_w at a fixed gas injection f_g^*. Noise was added to the simulation results to represent experimental data. The graphs also show the saturation levels corresponding to the parameters *fmdry*, *fmoil*, and *floil*.

In this particular case, there is no transition of steady-state water saturation levels below the critical water saturation in the presence of foam, represented in the `STARS` model by the parameter *fmdry* and illustrated in the top panel of Figure 24. Nevertheless, it is important to monitor water saturation when increasing the injected oil fraction, as it can activate the dry-out effects on foam performance. The *floil* and *fmoil* lines represent the regions where the oil begins to influence foam effectiveness and where it reduces the

foam's capacity to control gas mobility, respectively. Notice that in the transition at *fmoil*, the apparent viscosity of the flow begins to rise as oil injection increases, as illustrated in Figure 23.

Section **B.3.4** presents the results of simulations and parameter estimation for a ground-truth case with a reduced value of the *fmoil* parameter, a scenario also considered by Lyu et al. (2021b). In this study, we revisit this configuration to demonstrate the applicability of our approach under varying foam destruction thresholds.

4.4.2 Estimation of F_{oil} parameters

After collecting the steady-state data from the oil rate scan experiments (see Figures 23 and 24), the parameter estimation for the F_{oil} term can proceed. Figure 25 presents the data points for F_{oil} values at various oil saturations from the experimental protocol, while the solid line shows the fitted function according to the formulation in Eq. (4.11). The figure also shows the estimated F_{oil} function using Eq. (4.13) together with propagated uncertainties from the parameters, which are presented next. As shown in Figure 25, the estimated function closely matches the ground truth (red dashed line), demonstrating the efficacy of the proposed approach. The 90% prediction interval (shaded area) indicates the uncertainty associated with the parameter estimation, which is larger at intermediate oil saturations where the transition from full foam stability to complete foam destruction occurs.

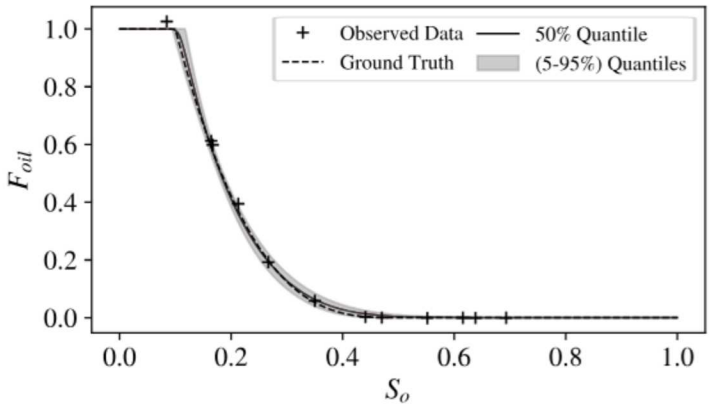

Figure 25 – Estimation of the parameters from the F_{oil} function with uncertainty propagation. The data points represent values derived from oil rate scan experiments. The solid line shows the fitted function, and the shaded area represents the 90% prediction interval. The ground truth function (dashed line) is included for comparison and serves as a reference for evaluating the accuracy of parameter estimation.

Figure 26 displays the joint posterior probability distributions of the estimated parameters (*floil*, *fmoil*, and *epoil*) in the lower triangular panels, as obtained through Bayesian inference, while the diagonal panels show the corresponding marginal posterior distributions. The correlation plots show that *floil* is well-constrained around 0.1, consistent

with the ground truth value, and that there is a significant correlation between *fmoil* and *epoil*. The marginal distributions indicate that *floil* is well-identified, whereas *fmoil* and *epoil* are considerably more challenging to estimate, presenting respectively a coefficient of variation (CoV) of 6.9%, 21.7%, and 32% illustrated further in Figure 31. The joint distributions reveal that different combinations of these parameters can yield similar F_{oil} functions, suggesting potential issues with parameter non-identifiability. Despite these challenges, the resulting posterior distributions reflect a good agreement between the data and the fitted model, closely aligning with the ground truth.

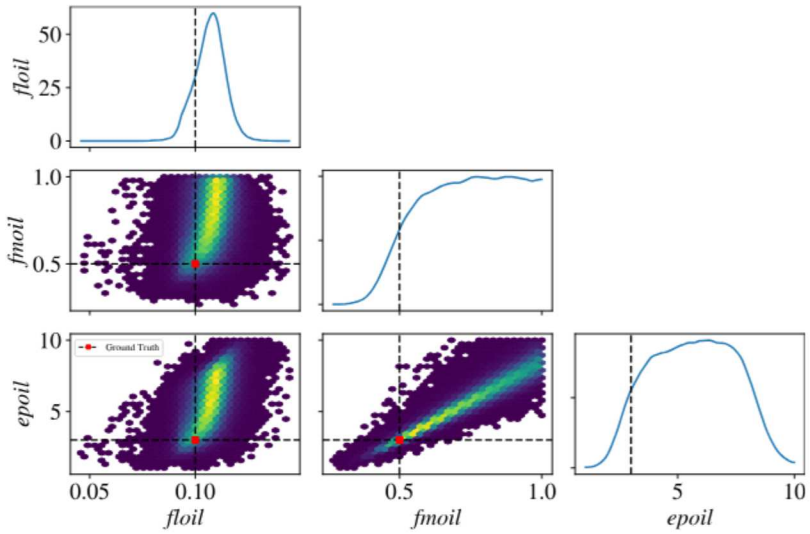

Figure 26 – Posterior probability distributions of estimated F_{oil} parameters obtained through Bayesian inference. Diagonal plots show marginal distributions for each parameter (*floil*, *fmoil*, and *epoil*), while off-diagonal plots demonstrate parameter correlations.

4.4.3 Uncertainty propagation of foam-oil interactions

The practical implications of parameter uncertainty are further explored here by presenting the results of numerical simulations with the estimated parameters and evaluating relevant quantities of interest, such as oil and gas production. To this end, we selected two simulation scenarios with different injection conditions (J) and initial saturation conditions (I) from the works of Lyu et al. (2021b) and Tang et al. (2022) to propagate the uncertainties from the estimated F_{oil} parameters (from Figure 26). Specifically, we employed the configurations referred to as Case 2 for Scenarios 3 and 4 (see Table 1 in Lyu et al. (2021b)). For consistency, we adopt the same notation and case labeling as presented in Lyu et al. (2021b). Scenario 3 reflects a medium with depleted oil saturation post-extraction, while Scenario 4 represents a near-primary oil-saturated state, where elevated oil content hinders foam stability.

4.4.3.0.1 Scenario 3

The injection (J) and initial (I) conditions for this simulation are represented in the diagram presented in Figure 27. Figure 27(a) shows the uncertainties in how the saturation path traverses regions of varying *MRF* values, which directly influences the efficiency of gas mobility control by foam. Panels (b) and (c) from Figure 27 show the uncertainties in gas and oil saturations. Notably, the formation of an oil bank is observed in all samples for this case, exhibiting some variability in its shape due to underlying uncertainties (gray shaded region).

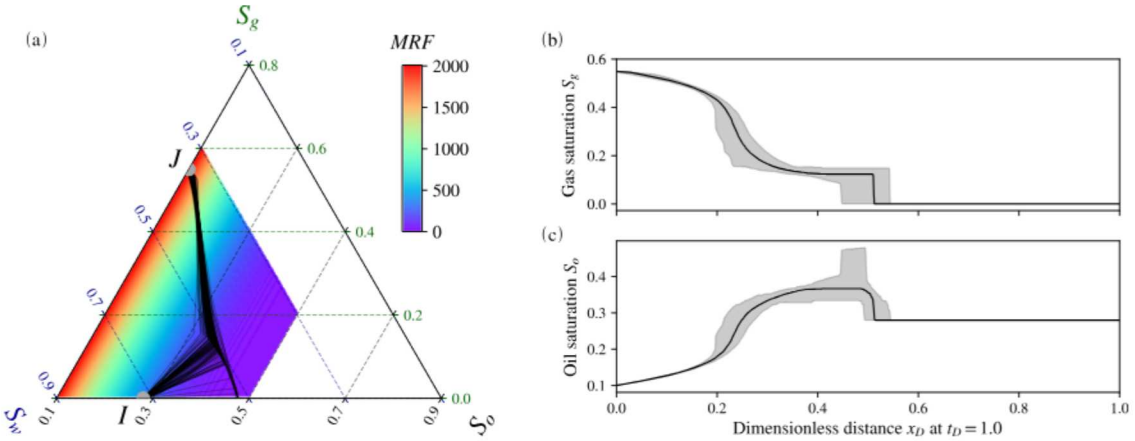

Figure 27 – Scenario 3 from Lyu et al. (2021b): (a) Uncertainty propagation to saturation paths (solid black lines) in a ternary diagram; (b) gas saturation; (c) oil saturation, both with associated uncertainties. The solid line represents the median and the shaded region the 90% prediction interval.

Figure 29 (left) presents the results of uncertainty propagation of Scenario 3 for the cumulative production of gas and oil phases over time, based on 1D simulations using the estimated posterior distributions of the parameters (see Figure 26). Although uncertainty in the F_{oil} parameters introduces variability in oil and gas production predictions, the overall magnitude of this uncertainty remains limited, primarily due to the small volume of initial oil in place. In summary, although saturation paths show some variability (see Figure 27), the efficiency of oil displacement as measured by oil production remains relatively stable.

4.4.3.0.2 Scenario 4

Next, we performed the uncertainty propagation of the F_{oil} parameters for the simulation of Scenario 4. The injection and initial conditions are depicted in Figure 28, along with the resulting uncertainty in the saturation paths (panel a), while the gas and oil saturations are shown in panels (b) and (c). The initial condition in this scenario corresponds to a case with a larger volume of oil in place, leading to significantly higher production levels compared to the previous case. From the oil saturation, it is also worth

noting that, in this case, no oil bank is formed. Furthermore, reduced uncertainty is observed in both the saturation paths and profiles.

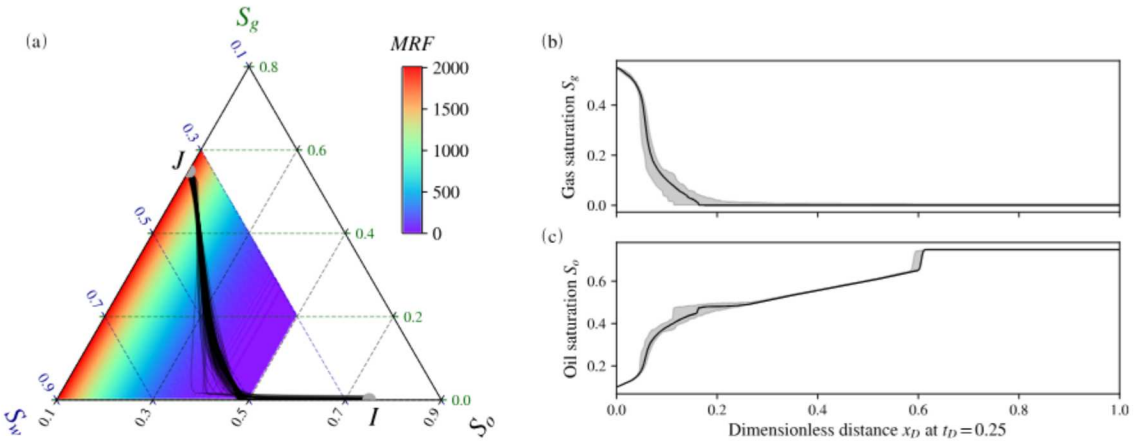

Figure 28 – Numerical results for Scenario 4 from Lyu et al. (2021b): (a) uncertainty propagation to saturation paths (solid black lines) in a ternary diagram; (b) gas saturation; (c) oil saturation, both with associated uncertainties.

Figure 29 (right) shows the results of uncertainty propagation of Scenario 4 for the cumulative production of gas and oil phases over time. As expected from the initial conditions, this case leads to a larger oil production, reaching approximately 0.6 PV by the end of the simulation. The magnitude of uncertainty of the productions remains small, which reflects the accuracy of the parameter fitting with reduced uncertainties.

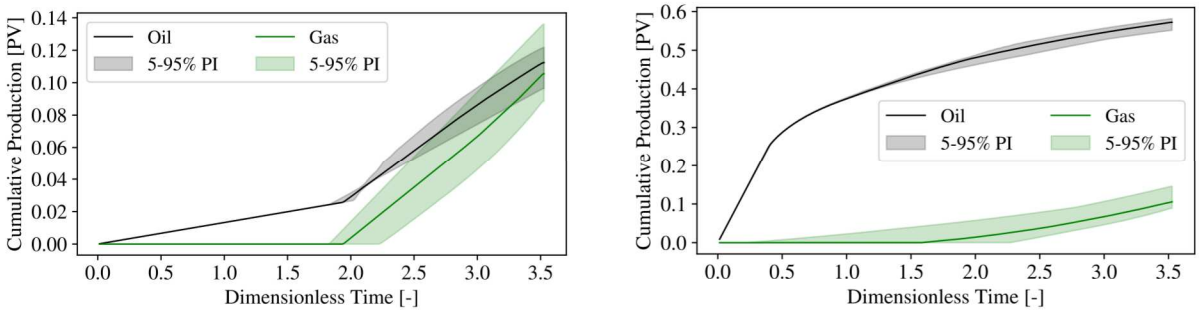

Figure 29 – Numerical results for the cumulative production of oil and gas phases over time with uncertainty propagation based on Scenarios 3 (left) and 4 (right) from Lyu et al. (2021b). The shaded areas represent 5-95% prediction intervals derived from the posterior distributions of F_{oil} parameters.

Table 8 quantifies the propagated uncertainties in terms of the coefficient of variation for the final cumulative production forecasts. Gas production exhibits higher uncertainty than oil production across both scenarios. The contrasting uncertainty patterns between scenarios reflect the different initial saturation conditions and their interaction with foam stability mechanisms under parameter variations.

Table 8 – Coefficient of variation for cumulative production under parameter uncertainty propagation for Scenarios 3 and 4.

	Coefficient of Variation (%)	
Scenario	Oil Production	Gas Production
3	7.1	14.4
4	2.0	21.2

4.4.4 Impact of parameters calibration on the oil production within 2D porous medium

This section examines the performance implications of two different foam characterizations by analyzing them in two-dimensional heterogeneous porous media simulations. Specifically, we consider a case in which the F_{oil} parameters were estimated under a data-scarce scenario in order to evaluate how the associated uncertainties affect the predictions of the three-phase foam flow model.

First, we present the data used for parameter estimation and uncertainty quantification in Figure 30 (left). In this case, several data points were intentionally removed to mimic a scenario with limited observational data, which often occurs due to the high costs of conducting such experiments (Valdez et al., 2021). Figure 30 (right) displays the F_{oil} term computed using the fitted parameters, with the associated uncertainties represented as a prediction interval. In this case, the uncertainties are substantially wider than those observed previously (see Figure 25), reflecting the reduced amount of observational data available for parameter inference. It is also noteworthy that the uncertainties associated with the *floil* parameter are greater than those related to the *fmoil* parameter, as evidenced by the broader prediction intervals in the upper and lower regions of the graph, respectively.

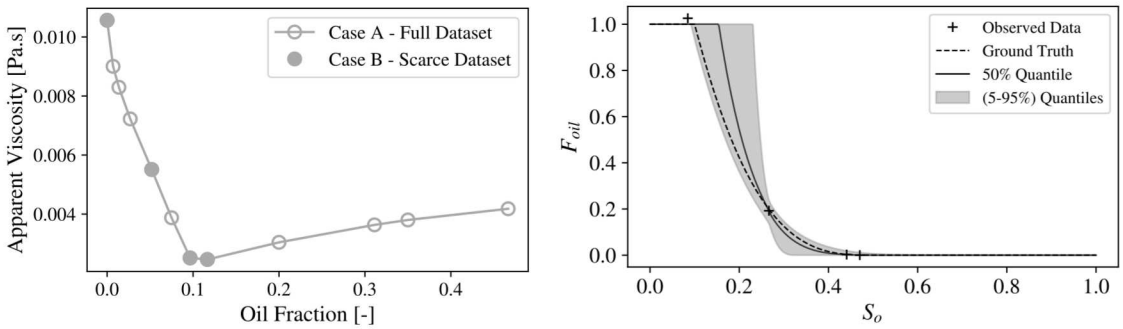

Figure 30 – Left: Steady-state values of apparent viscosity as a function of oil fraction f_o, shown for both the full dataset (all circles) and the reduced dataset (filled circles only) used for parameter inference. Right: Derived data points for F_{oil}, along with the estimated parameters and their associated uncertainty. The solid line represents the fitted model, the dashed line corresponds to the model with ground-truth parameters, and the shaded region indicates the 90% prediction interval.

Figure 31 presents the coefficients of variation for the posterior distributions

obtained in Case A and Case B. The results indicate that the most pronounced difference between the two cases is observed in the *floil* parameter, whereas the other two parameters exhibit only moderate to small variation.

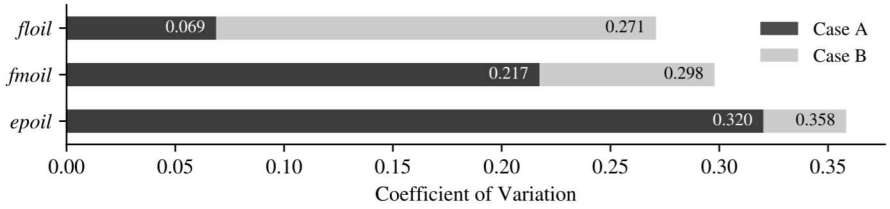

Figure 31 – Coefficient of variation for the estimated posterior distributions for the F_{oil} parameters in Case A and Case B.

Next, we employed the F_{oil} parameters listed in Table 9, which were obtained from estimations using both the full and reduced datasets, to conduct simulations based on the 19th layer of the SPE 10 model, as shown in Figure 21. All other fluid properties are consistent with those reported in Table 7, except for the residual oil saturation, which was increased to 0.15 to emphasize the effects of parameter mismatches. The injection process follows the same initial and boundary conditions described in the previous section, with an injection pressure of 10^5 Pa applied at the left boundary, and the simulations were carried out for a total of 50000 seconds.

The two cases analyzed in this study are labeled as Case A and Case B, and the oil-related parameters estimated for each one are reported in Table 9. Case B corresponds to the scenario with limited data available for parameter inference (see Figure 30), and the estimated parameters indicate a foam formulation that exhibits greater tolerance to the presence of oil.

Table 9 – Foam parameters for the oil term F_{oil} in cases A (full dataset), B (scarce dataset), and the ground-truth (GT) parameters.

Case	*floil*	*fmoil*	*epoil*
A	0.1069	0.4882	2.939
B	0.2055	0.7513	9.991
GT	0.1	0.5	3.0

Figure 32 presents snapshots of the saturation from the 2D simulations in a heterogeneous medium for both cases at selected time instants. Initially, a water front advances, pushing some of the oil and tracing preferential paths through the high-permeability zones. Subsequently, the gas front not only advances but also mobilizes both other phases in areas not previously swept by water. Notably, in case B, the gas front appears more contained,

as the estimated F_{oil} indicates a greater resistance to the detrimental effects of the oil on foam.

The cumulative production of oil and gas, expressed in pore volumes (PV), is shown in Figure 33 for both simulation cases. In case A, the projected oil production at the final simulation time surpasses that of case B, achieving a difference of over 5%. This increase can be attributed to the enhanced overall mobility during displacement, as the modelled foam in B is less affected by oil. At the same injection pressure, the gas velocity in case A is higher. As the foam in case A is more susceptible to oil effects, gas production is greater during the entire simulation; that is, the foam provides less gas trapping.

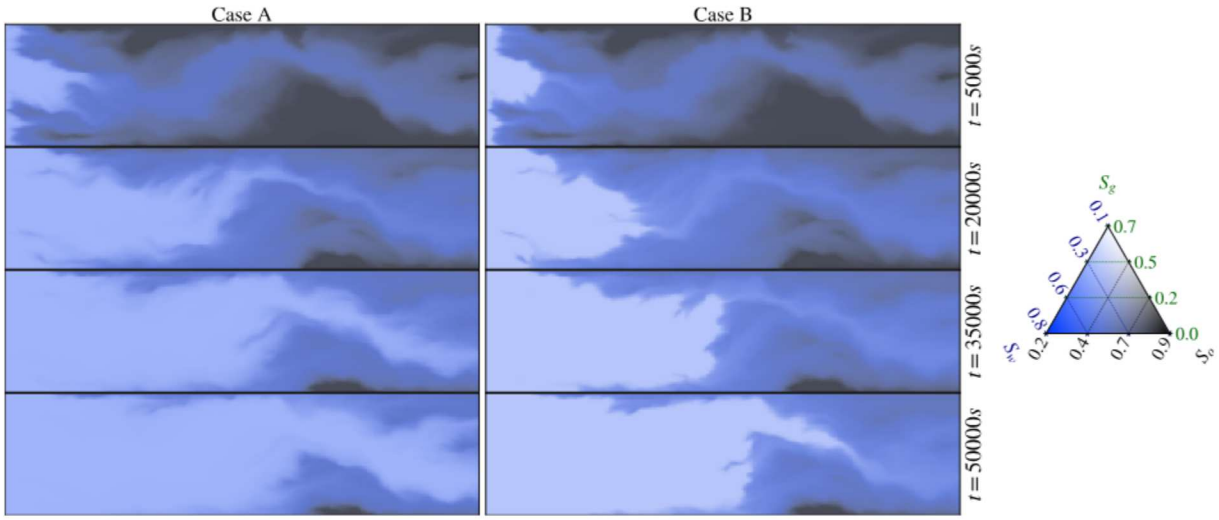

Figure 32 – Saturation profiles at different time instants for case A (left) and B (right). The triangle represents the color coding used to describe the predominant phase saturation.

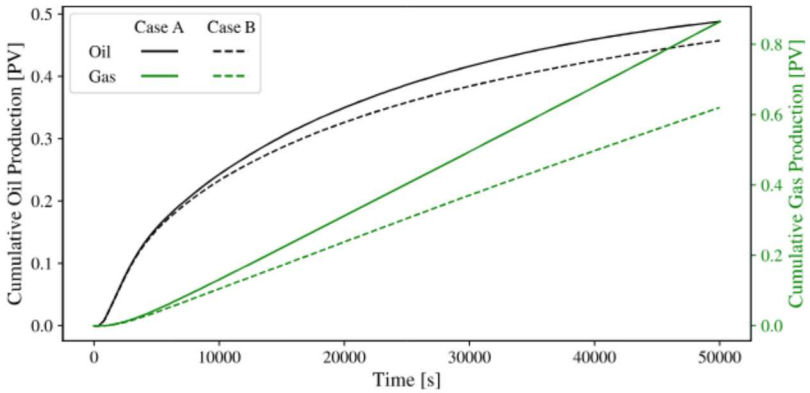

Figure 33 – Comparison of gas and oil productions for a water-gas coinjection at initial conditions $(S_o, S_w) = (0.8, 0.2)$ with a core initially with 80% oil and 20% water.

4.5 DISCUSSIONS

Beyond fitting parameters, this work aims to computationally understand how experimental procedures are reflected in relevant observations to characterize the effects of

oil, considering measurable oil saturation. The development of standardized steady-state protocols with direct, continuous saturation monitoring would substantially advance the characterization and parameter estimation method of foam-oil effects, providing more reliable inputs for field-scale simulation models.

We investigated an experimental protocol for obtaining representative oil saturation measurements, which are essential for accurately characterizing the F_{oil} function. This approach incorporates the assumption that the *floil* parameter meets or exceeds residual oil saturation. However, this assumption may not hold universally, as residual oil saturation alone could potentially reduce foam capacity for gas mobility control. This *floil* threshold is absent in alternative models, such as the implementation in the ECLIPSE simulator (Schlumberger, 2014), which eliminates this parameter by assigning it a value of zero. Comparative analysis of F_{oil} function formulations may be addressed in future works.

As observed in Figure 26, even with a dataset exhibiting minimal noise, the parameters derived from F_{oil} indicate potential issues with identifiability (non-uniqueness of parameters). Notably, *fmoil* and *epoil* show a significant correlation within the posterior distribution, lacking a distinctly defined peak. This issue can be reduced with additional data points. It may also be further explored together with other implicit-texture models found in the literature that consider fewer parameters for this representation (Schlumberger, 2014; Namdar-Zanganeh et al., 2010).

Uncertainties in the F_{oil} function play a pivotal role in the reliability of model predictions. For instance, in Scenario 3, even a minor uncertainty in the F_{oil} function led to significant variations in oil and gas production. On the other hand, in Scenario 4, gas production exhibited high uncertainty, as demonstrated by the coefficient of variation presented in Table 8. These findings are particularly important when dealing with scenarios with very high or very low water saturation initially, where predictions may underestimate or overestimate oil production or CO_2 storage capacity.

In the case study analyzing three-phase co-injection presented in this work, which employed the parameters outlined by Lyu et al. (2021b), we observed in Figure 24 that the dry-out effects were negligible. This was due to no significant variation in water saturation, which prevented it from reaching the critical threshold for foam collapse. However, in practical scenarios of three-phase co-injection, especially in cases where a strong foam is present, the injected oil can displace some of the water saturation. This situation can lead to significant dry-out effects. Therefore, accurately determining and considering the term F_{dry} is crucial for the calculations, as shown in Eq. (4.13).

4.6 CONCLUSIONS

This study presented an approach for characterizing foam parameters in the presence of oil, with an emphasis on data typically obtained from laboratory experiments. To achieve this, we replicated core flooding experiments through computer simulations to assess how oil influences foam stability and how these effects can be quantified using steady-state measurements. A detailed, step-by-step approach was outlined for conducting experiments that generate data essential for the accurate characterization of oil-related parameters in implicit-texture foam models. A Bayesian framework was employed for parameter estimation, enabling the assessment of parameter uncertainty. Subsequently, a series of numerical simulations were performed, propagating the obtained parametric uncertainty to model outputs, such as oil and gas production, to evaluate the impact of these uncertainties. Additionally, we conducted two-dimensional simulations using a representative heterogeneous permeability field, considering two distinct parameter sets. One set of parameters was derived from a limited dataset to simulate the challenges typically encountered in experimental conditions with sparse data.

The simulation results demonstrated that gradual increases in oil-water injection ratios at fixed gas fraction provide more reliable data for parameter estimation. The numerical simulations addressed limitations in current experimental protocols where abrupt increases in oil injection often lead to non-representative oil saturations, hampering accurate characterization of functions in implicit-texture models.

Bayesian inference techniques applied to synthetic experimental data highlight difficulties in parameter identification. Uncertainty propagation through one-dimensional simulations revealed that even minor parameter uncertainties significantly impact predictions of gas production more than those of oil production. The two-dimensional heterogeneous simulations confirmed that inaccurate estimation of oil-related parameters from limited datasets leads to substantial variations in displacement patterns, cumulative production, and gas-oil ratios.

5 FOAM STRENGTH ASSESSMENT THROUGH MOBILITY REDUCTION FACTOR FORMULATION

This chapter presents the paper de Miranda et al. (2025a) submitted for consideration of publication entitled "*On the mobility reduction factor for the quantification of foam strength in porous media*", which develops a parameter estimation approach based on a new expression for the mobility reduction factor for characterizing foam parameters through direct pressure drop measurements, bypassing intermediate relative permeability modeling steps as required in other approaches from the literature.

5.1 INTRODUCTION

Predicting foam behavior at the core scale is critical for transferring laboratory insights to the field (Ma et al., 2015). Numerical simulators, such as `STARS` (CMG, 2019), represent foam effects through a mobility reduction factor (MRF) that multiplies down the gas mobility. In principle, this aligns with the widely accepted view that foam mainly suppresses gas flow (Bernard and Jacobs, 1965; Kovscek and Radke, 1994; Rossen, 1996; Eftekhari and Farajzadeh, 2017). However, in laboratory practice, foam strength is usually quantified via apparent viscosity, which is proportional to the pressure drop and influenced by both phases (Farajzadeh et al., 2015b; Eftekhari and Farajzadeh, 2017). Additionally, experimental formulations of MRF do not clearly distinguish the reduction in gas-phase mobility, which makes it inconsistent with the modeling assumption of gas-only mobility reduction, complicating parameter estimation (Lotfollahi et al., 2016).

Most approaches, therefore, rely on relative permeability functions to disentangle phase contributions (Ma et al., 2014b). Yet relative permeability estimation is itself uncertain and strongly affects the identifiability of foam parameters (Zeng et al., 2016; Cavalcante Filho et al., 2017; Valdez et al., 2021; Ribeiro et al., 2024; de Miranda et al., 2024). This creates a two-layer uncertainty source: first in relative permeability, then in foam characterization.

In this chapter, we propose an alternative formulation of the MRF that isolates the gas-phase contribution directly, without requiring relative permeability functions. The method is derived algebraically from the steady-state experimental definition of MRF, producing a gas-specific expression consistent with simulator formulations such as `STARS`. We then evaluate its performance for parameter estimation using synthetic foam-quality scans, comparing it against the conventional apparent-viscosity-based objective function. Identifiability and robustness are assessed under both correct and misspecified relative permeability models, highlighting how the proposed definition confines the uncertainty to the foam parameters alone.

5.2 MATHEMATICAL MODELING

The foam flow in porous media can be modeled by a multiphase system with surfactant transport, where phases are assumed to be incompressible and immiscible. The system involves mass conservation for each phase, flow relationships for phase velocities, and transport of surfactant. Phase saturations are denoted by S_α, velocities by u_α, where $\alpha \in \{w, g\}$, and C_s represents the aqueous surfactant concentration (Zavala et al., 2024). These governing equations are simplified under the conditions of steady-state laboratory experiments, where constant inlet fluxes, pressures, and surfactant concentration are assumed. This reduces the mass conservation and transport equations to algebraic expressions (Valdez et al., 2021; de Miranda et al., 2022a). The homogeneity hypothesis results in spatial invariance of saturations and concentrations, yielding a constant pressure drop ΔP, water saturation, and surfactant concentration (Ma et al., 2013; Eftekhari and Farajzadeh, 2017; Kahrobaei and Farajzadeh, 2019).

The fractional flow of a phase α is defined as the ratio of the phase velocity to the total velocity of all phases flowing through the porous medium:

$$f_\alpha = \frac{u_\alpha}{u_T}, \quad u_T = \sum_\alpha u_\alpha, \tag{5.1}$$

where u_T is the total superficial velocity in the flow direction. At steady-state conditions in experimental settings, the apparent viscosity of the system can be calculated as follows:

$$\mu_{app} = \lambda_T^{-1} = \frac{\mathrm{K}}{u_T}\frac{\Delta p}{L}, \tag{5.2}$$

where λ_T is the total mobility, K is the absolute permeability of the domain, Δp is the pressure difference, and L is the length of the core. At steady-state, the fractional flow of each phase can also be expressed mathematically as the ratio of its mobility to the total mobility, that is:

$$f_\alpha = \frac{\lambda_\alpha}{\lambda_T}, \tag{5.3}$$

where the phase mobility is given by $\lambda_\alpha = k_{r\alpha}/\mu_\alpha$, and depends on relative permeability $k_{r\alpha}$ and viscosity μ_α of phase α.

5.2.1 Relative Permeability

Relative permeabilities are usually described either by the Brooks-Corey (Brooks and Corey, 1963) or LET models (Lomeland et al., 2005). Without considering foam effects, the Brooks-Corey form for water-gas flow is given by:

$$k_{rw}^{\text{Corey}} = k_{rw}^0\, s_w^{n_w}, \qquad k_{rg}^{\text{Corey}} = k_{rg}^0\,(1 - s_w)^{n_g}, \tag{5.4}$$

with the normalized water saturation defined by

$$s_w = \frac{S_w - S_{wc}}{1 - S_{wc} - S_{gr}}, \tag{5.5}$$

where n_w and n_g are the Corey exponents.

The LET functions for relative permeability (Lomeland et al., 2005), which offer more flexibility to describe multiphase flow, are defined as:

$$k_{rw}^{\mathrm{LET}} = k_{rw}^{0} \frac{s_w^{L_w}}{s_w^{L_w} + E_w \left(1 - s_w\right)^{T_w}}, \qquad k_{rg}^{\mathrm{LET}} = k_{rg}^{0} \frac{\left(1 - s_w\right)^{L_g}}{\left(1 - s_w\right)^{L_g} + E_g {s_w}^{T_g}}, \tag{5.6}$$

where L_w, L_g control the lower part of the curve, E_w, E_g determine transition curvature, T_w, T_g characterize upper part of the curve, and S_{wc} and S_{gr} denote connate water and residual gas saturations. In general, the LET correlation functions for relative permeability provide a better description of the data (Berg et al., 2021b).

5.2.2 Foam Model

The implicit-texture formulation implemented in `STARS` (CMG, 2019) represents foam effects through a mobility reduction factor (MRF) term applied to reduce the gas phase mobility. For water-gas systems, the apparent viscosity is expressed as:

$$\mu_{app} = \left(\lambda_w + \frac{\lambda_g}{MRF}\right)^{-1} = \left(\frac{k_{rw}}{\mu_w} + \frac{k_{rg}}{\mu_g MRF}\right)^{-1} \tag{5.7}$$

while the mobility reduction factor of the `STARS` model for foam is given by

$$MRF = 1 + fmmob \prod_i F_i, \tag{5.8}$$

where F_i represent dimensionless functions capturing various foam destabilization mechanisms. This chapter considers two primary effects: the dry-out function F_{dry} accounting for foam coalescence at low water saturations, and the surfactant function F_{surf} representing concentration-dependent foam stability.

The dry-out function takes the form:

$$F_{dry}(S_w) = \frac{1}{2} + \frac{\arctan[epdry(S_w - fmdry)]}{\pi} \tag{5.9}$$

where *fmdry* represents an approximation for the critical water saturation below which foam becomes unstable and collapses, and *epdry* controls the sharpness of the transition from the low- to high-quality regimes (Osterloh and Jante, 1992). The surfactant concentration effect is modeled as:

$$F_{surf}(C_s) = \begin{cases} \left(\frac{C_s}{fmsurf}\right)^{epsurf} & \text{if } C_s < fmsurf, \\ 1 & \text{otherwise,} \end{cases} \tag{5.10}$$

where *fmsurf* denotes the reference surfactant concentration (wt%) and *epsurf* determines the sensitivity of foam strength to concentration changes.

Estimation of the model's parameters relies on steady-state core flooding experiments conducted at various foam qualities and surfactant concentrations. The primary observable is the relationship between apparent viscosity and injected gas fraction at constant total velocity. As foam quality increases, the apparent viscosity initially rises due to foam generation, then decreases beyond a transition quality f_g^* corresponding to the onset of dry-out conditions. The reference mobility reduction factor *fmmob* scales the overall foam strength and is determined through history matching of experimental pressure drop and saturation data (Ma et al., 2013).

5.2.3 The mobility reduction factor expression

Since the first application of foam for gas mobility control (Bond and Holbrook, 1956), the quantification of its mobility-reduction capability has evolved from empirical correlations toward a mechanistic understanding (Ma et al., 2015). While the assumption of foam reducing solely gas-phase mobility prevails (Bernard and Jacobs, 1965; Eftekhari and Farajzadeh, 2017), modeling approaches in the literature have linked the experimentally measured ratio of pressure drop with and without foam (Chang and Grigg, 1996; Mohammadi et al., 1995; Ma et al., 2015). Typically, the mobility reduction factor (*MRF*) is computed using the following expression

$$\frac{\Delta P_{\text{foam}}}{\Delta P_{\text{ref}}}, \tag{5.11}$$

to characterize foam. However, even approaches assuming that foam affects solely gas-phase mobility may be misled by inconsistencies between this modeling assumption and the classical definition of such ratios during parameter estimation (Vieira et al., 2024; Hematpur et al., 2025).

According to Rosman and Kam (2009), the *MRF* is determined from the pressure drop ratio between the foam and no-foam conditions in the same rock sample at identical saturation states. In the literature, however, the no-foam pressure drop ΔP_{ref} has been defined in different ways: continuous brine injection (Simjoo et al., 2013; Jia et al., 2024), continuous gas injection (Bello et al., 2023c), or water–gas co-injection (Sri Hanamertani et al., 2021; AlYousef et al., 2023). Each condition yields distinct quantities associated with *MRF*, hindering direct comparison of experimental results and complicating parameter estimation in foam simulators.

5.2.4 Current parameters estimation procedures

In a steady-state scenario, the relative permeability for any chosen model can be written in terms of experimentally measurable quantities

$$k_{r\alpha} = \frac{\mu_\alpha \, f_\alpha}{\mu_{app}}. \tag{5.12}$$

A significant assumption among the methods for foam parameter fitting relying on apparent viscosity measurements (Eq. (5.7)) is that the relative permeability functions are known prior to analysis (Ma et al., 2013; Eftekhari and Farajzadeh, 2017; Vicard et al., 2022; Valdez et al., 2021). However, its accuracy relies on the adequacy of the relative permeability model and the quality of the data used for parameter fitting; uncertainties in either the model or its parameters at this stage inevitably propagate into the foam parameter estimates.

Procedures for foam parameter estimation relying on steady-state data from a foam-quality scan or flow-rate scan, without monitoring water saturation experimentally, generally assume that the relative permeabilities are described by the modified Brooks-Corey model (Brooks and Corey, 1963). The experiments provide data points in the form of (f_g^i, μ_{app}^i). To evaluate the `STARS` model for parameter estimation, however, the corresponding water saturation must be determined for each given pair (f_g, μ_{app}). Therefore, if the Brooks-Corey form is assumed, the corresponding water saturation can be analytically inverted, as proposed by Farajzadeh et al. (2015b) and Eftekhari and Farajzadeh (2017), as follows:

$$S_w = \left(\frac{(1 - f_g)\mu_w}{k_{rw}^0 \, \mu_{app}} \right)^{\frac{1}{n_w}} (1 - S_{wc} - S_{gr}) + S_{wc}. \tag{5.13}$$

Once S_w is obtained for each pair (f_g, μ_{app}), the foam apparent viscosity model (`STARS`) can be computed, since it depends on S_w through $F_{dry}(S_w)$ (Eqs. (5.7)-(5.9)). Since S_w estimation from apparent viscosity data relies on assumed relative permeability functions (Eq. (5.13)), uncertainties in these functions further propagate to parameter estimation.

The LET relative permeability model described in Eq. (5.6), unlike the Brooks-Corey model, cannot be analytically inverted for saturation, requiring numerical methods for this inversion. Consequently, its application with the `STARS` foam flow model has been limited. In the following, we introduce a new expression to quantify the *MRF*, enabling the estimation of foam parameters without prior knowledge of, or assumptions about, the relative permeabilities.

5.2.5 Derivation of a new *MRF* expression

An alternative expression connecting experimental measurements of pressure drop to the *MRF* term used in foam models is derived from the formula given in Eq. (5.11) following the experimental requirements defined by Rosman and Kam (2009). The present approach contributes to establishing a quantity that does not depend on relative permeability for foam characterization. This is because the empirical effects in the *MRF* term depend directly on observable variables and do not require knowledge of modeling phase mobilities.

Starting from a steady-state flow at the same saturation levels, the pressure drop ratio between the foam and no-foam cases is analogous to the ratio between the total mobilities, which can be expressed as:

$$\frac{\Delta P_{\text{foam}}}{\Delta P_{\text{ref}}} = \frac{\frac{u_T L}{K}\,\mu_{app}^{\text{foam}}}{\frac{u_T L}{K}\,\mu_{app}^{\text{ref}}} = \frac{\mu_{app}^{\text{foam}}}{\mu_{app}^{\text{ref}}} = \frac{\lambda_T^{\text{ref}}}{\lambda_T^{\text{foam}}} = \frac{\lambda_l + \lambda_g}{\lambda_l + \frac{\lambda_g}{MRF}}\,, \tag{5.14}$$

where λ_l represents liquid phase mobility (water or combined water-oil in three-phase systems). Next, rearranging to isolate the foam-induced pressure increment yields the following expression:

$$\frac{\Delta P_{\text{foam}}}{\Delta P_{\text{ref}}} - 1 = \frac{\lambda_l + \lambda_g}{\lambda_l + \frac{\lambda_g}{MRF}} - 1 = \frac{(\lambda_l + \lambda_g) - \left(\lambda_l + \frac{\lambda_g}{MRF}\right)}{\lambda_l + \frac{\lambda_g}{MRF}} = \frac{\frac{\lambda_g}{MRF}\,(MRF - 1)}{\lambda_l + \frac{\lambda_g}{MRF}}\,. \tag{5.15}$$

Normalizing by the steady-state form of the gas fractional flow f_g in presence of foam (Eq. (5.3)) isolates the contribution to gas-phase:

$$MRF = 1 + \frac{\Delta P_{\text{foam}} - \Delta P_{\text{ref}}}{f_g\,\Delta P_{\text{ref}}} = \frac{\Delta P_{\text{foam}} - (1 - f_g)\,\Delta P_{\text{ref}}}{f_g\,\Delta P_{\text{ref}}}\,. \tag{5.16}$$

The *MRF* term is designed in implicit-texture foam models by adding a unitary regularization term to the part modeling the foam effects in reducing gas mobility, as shown in Eq. (5.7) (right), ensuring that gas mobility returns to its original state when foam effects vanish. Indeed, if $\Delta P_{\text{foam}} = \Delta P_{\text{ref}}$ in Eq. (5.16), we have $MRF = 1$.

Note that Eq. (5.16) can also be written as:

$$MRF = \frac{\Delta P_{\text{foam}} - f_l\,\Delta P_{\text{ref}}}{f_g\,\Delta P_{\text{ref}}}\,, \tag{5.17}$$

which clearly and correctly defines *MRF*. The numerator subtracts the liquid contribution of the reference pressure drop, $f_l\,\Delta P_{\text{ref}}$, from the total foam pressure drop, isolating the portion attributable to the gas phase under foam. The denominator, $f_g\,\Delta P_{\text{ref}}$, is the gas contribution of the reference pressure drop. Thus, *MRF* quantifies the foam-induced amplification of gas-phase resistance relative to its baseline, without requiring relative-permeability curves.

Observe that, if $f_l\,\Delta P_{\text{ref}}$ were replaced by $f_l\,\Delta P_{\text{foam}}$, Eq. (5.17) would reduce to the simple ratio $\Delta P_{\text{foam}}/\Delta P_{\text{ref}}$, thereby losing the gas-specific normalization. In that case, the *MRF* definition would implicitly incorporate changes related to the liquid phase, while the objective of *MRF* is to isolate the effect of foam on the gas phase only. Therefore, the subtraction must involve the liquid contribution of the reference case, ensuring that *MRF* remains a gas-specific measure of foam strength.

Figure 34 illustrates the alignment between the proposed *MRF* expression (dots) and the one computed with the `STARS` equation (solid line), in comparison to the classical *MRF* definition (crosses), $\Delta P_{\text{foam}}/\Delta P_{\text{ref}}$, using noisy datasets for foam and no-foam experiments.

A quantitative analysis was also performed to complement the visual inspection. Since the *MRF* values span several orders of magnitude, the evaluation employed the Mean Absolute Percentage Error (MAPE) as a scale-invariant metric. The classical *MRF* definition exhibited substantial deviations (average MAPE ≈ 1.75), whereas the proposed formulation demonstrated high accuracy across all scenarios (average MAPE ≈ 0.007).

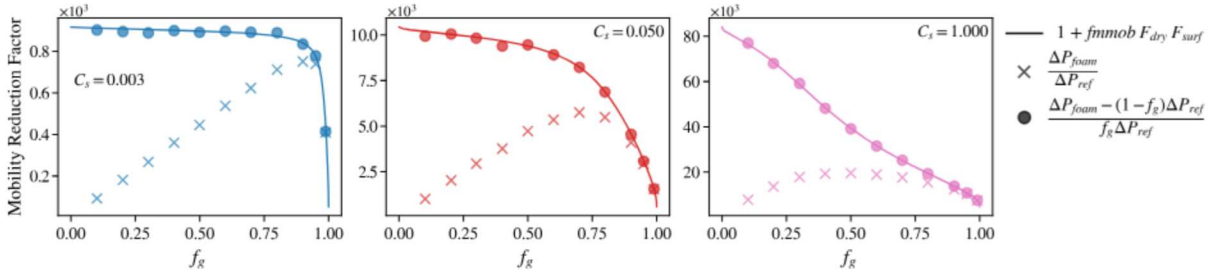

Figure 34 – Comparison of the *MRF* expression in the `STARS` model (solid line) in front of the datasets considering the two formulas, Eq. (5.11) (cross) and Eq. (5.16) (dot), over noisy observations for different surfactant concentrations. As the concentration increases, the impact of noise on saturation and pressure drop becomes less significant, improving the precision of the calculations.

We observe that for low f_g values, the classic definition drastically underestimates the correct value of *MRF*, since f_l is high. Because it normalizes by the total (liquid+gas) reference drop rather than the gas contribution, the large liquid contribution in the denominator reduces the foam-induced gas resistance. Indeed, since

$$\frac{\Delta P_{\text{foam}}}{\Delta P_{\text{ref}}} = \frac{\lambda_l + \lambda_g}{\lambda_l + \lambda_g / MRF} = \frac{1}{(1 - f_g) + f_g / MRF}, \tag{5.18}$$

in the liquid-dominated limit $f_g \to 0$, this ratio tends to unity regardless of the actual value of *MRF*. Therefore, $\Delta P_{\text{foam}} / \Delta P_{\text{ref}}$ systematically underestimates the correct *MRF* when f_g is small. On the other hand, the novel estimation of *MRF* follows the true values. This comparison demonstrates that the proposed expression aligns more closely with the model formulation, supporting its use for direct parameter estimation based on only pressure drop measurements.

5.3 DATASET AND PARAMETER ESTIMATION APPROACH

Synthetic datasets were generated using the implicit-texture foam model (Eq. (5.7)) with known parameter values to focus on the mathematical aspects of parameter estimation and uncertainty quantification approaches. This strategy eliminates experimental uncertainties and model-data mismatch, allowing comparisons to a reference value to understand the fundamental properties of different estimation methods, and has been used extensively in the literature (Berg et al., 2024; Ribeiro et al., 2024; de Miranda et al., 2024).

To generate the dataset, we based our models and parameters on the work of Jones et al. (2016). The foam parameters were derived from their data using steady-state multiphase flow equations with foam effects (Eqs. (5.1)-(5.6)). However, to assess robustness against model mismatch, we used the LET functions. To this end, we approximated the relative permeabilities reported by Jones et al. (2016), which are Brooks-Corey based, using the LET relative permeabilities.

Figure 35 shows the LET relative permeability functions (solid lines), which were based on data from the Brooks-Corey representation of Jones et al. (2016). The parameters of the LET functions are reported in Table 10, along the original Corey exponents ($n_w = 2.86$, $n_g = 0.7$) from Jones et al. (2016). It is important to note that the LET function can reproduce the shape of the Brooks–Corey function, whereas the converse is not necessarily true. This flexibility gives the LET formulation a broader applicability and makes it better suited for representing diverse relative permeability behaviors (Berg et al., 2021b; Valdez et al., 2020).

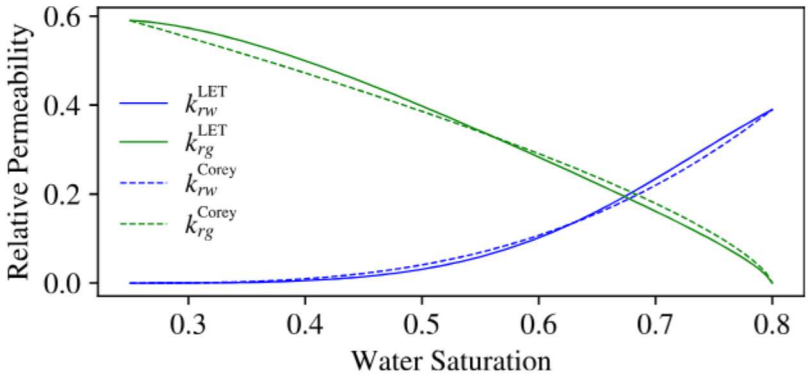

Figure 35 – Comparison of LET (solid lines) and Brooks-Corey (dashed lines) relative permeability functions used in this work.

With the set of parameters reported in Table 10, the dataset - presented in Figure 36 - spanned surfactant concentrations of 0, 0.003, 0.01, 0.03, 0.05, 0.1, 0.5, and 1.0 wt%. The zero-concentration case provides the reference conditions required for *MRF* calculation using Eq. (5.16), conducted at high gas fractions to achieve high gas saturations, similar to those observed in the presence of foam. Simulations include foam qualities from 0.1 to 0.99, generating pressure drop and saturation data where true parameter values are known exactly. A 10% Gaussian noise is added to the apparent viscosity and saturation values to simulate uncertainty inherent in experimental measurements (Berg et al., 2024). The original dataset from Jones et al. (2016) and the synthetic dataset are presented in the left and right panels of Figure 36. The steady-state foam corefloods from Jones et al. (2016) were conducted on Bentheimer sandstone cores at 60°C and 20 bar back-pressure. Nitrogen and an AOS surfactant solution were co-injected at a constant superficial velocity of 2.4×10^{-5} m/s to generate foam, while pressure drop was measured. The differences

between the original dataset and model-generated data arise from model limitations that do not fully capture the experimentally observed behavior.

Table 10 – Parameter values used for synthetic data generation based on Jones et al. (2016)

Foam Parameters				
fmmob	*fmdry*	*epdry*	*fmsurf*	*epsurf*
84916	0.334	66.7	0.558	0.865
Relative Permeability Parameters				
k_{rw}^0	S_{wc}	L_w	E_w	T_w
0.39	0.25	3.0	2.0	1.0
k_{rg}^0	S_{gr}	L_g	E_g	T_g
0.59	0.2	0.75	1.0	1.5
Fluid/Rock Properties				
μ_w [Pa·s]	μ_g [Pa·s]	u_t [m/s]	σ [N/m]	ϕ
1.0×10^{-3}	1.805×10^{-5}	2.4×10^{-5}	0.0291	0.23

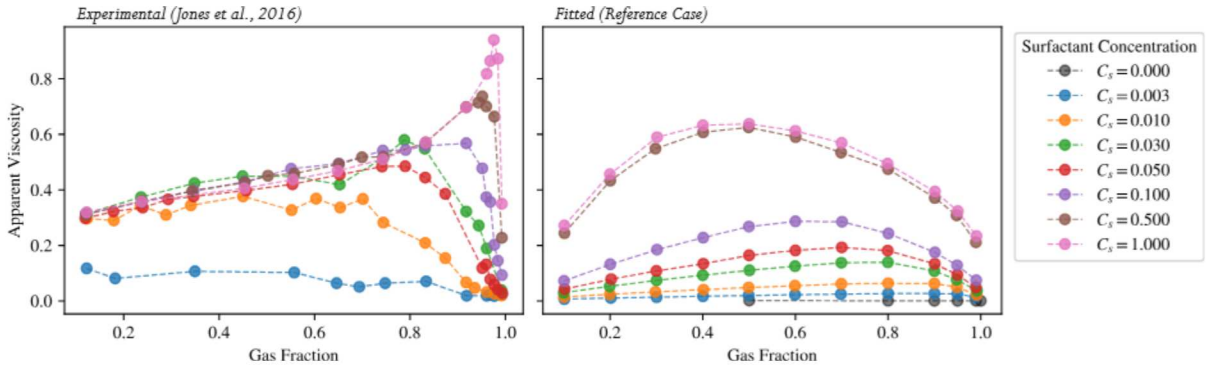

Figure 36 – Apparent viscosity vs foam quality for different surfactant concentrations. Left: The original data from Jones et al. (2016) data. Right: The synthetic data at the same surfactant concentrations plus a no surfactant experiment, that is, without foam, used as a reference for *MRF* calculation.

Therefore, from this point onward, we use the dataset generated with the parameters estimated by Jones et al. (2016). Based on these data, two distinct datasets were constructed. The first dataset provides direct measurements of apparent viscosity (μ_{app}) in relation to foam quality (f_g). The second dataset contains calculated *MRF* values derived from pressure drop measurements based on the proposed Eq. (5.16); the data are presented for three selected surfactant concentrations in Figure 34.

5.4 METHODS

The two parameter estimation approaches evaluated in this work are illustrated in Figure 37, highlighting the fundamental difference in their workflows and data requirements. The apparent viscosity approach (highlighted in blue) requires previous knowledge of the relative permeability functions and the pressure drop with foam. In contrast, the proposed

MRF approach of this work (highlighted in green) relies solely on pressure experimental data with and without foam, and no information about the relative permeabilities is required.

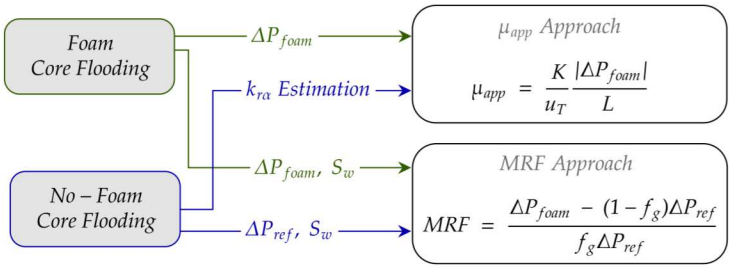

Figure 37 – Workflow comparison for foam parameter estimation. Method (Direct *MRF*) uses reference experiments at matching saturations to directly calculate mobility reduction factors. The Apparent Viscosity approach requires a separate relative permeability characterization to model apparent viscosity. Both methods optimize for the same foam model parameters using different objective functions.

5.4.1 Foam Parameter Estimation

In this section, we describe the objective functions employed for foam parameter estimation. Two alternatives are considered: one based on apparent viscosity (Eq.(5.7)) and another based on the mobility-reduction factor (*MRF*) proposed in this work (see Eq.(5.16)). Both functions represent the normalized sum of squared deviations between model predictions and experimental observations.

The accuracy of the methods for estimating foam parameters using apparent viscosity observations also depends on the adequacy of the assumed relative permeability model and its estimated parameters. Structural mismatch between assumed $k_{r\alpha}$ functions and true flow behavior or parametric uncertainties propagates into foam parameter estimates (Ma et al., 2013; Eftekhari and Farajzadeh, 2017; Vicard et al., 2022; Valdez et al., 2021).

In the following, the apparent viscosity–based and *MRF*-based parameter estimation approaches are formulated as optimization problems.

5.4.1.0.1 Apparent Viscosity Approach

Given the observed apparent viscosity μ_{app}^{obs}, and the relative permeability parameters $\boldsymbol{k}$ to evaluate apparent viscosity model μ_{app}^{model} using Eq. (5.7), find foam parameters $\boldsymbol{\theta}$ that minimizes

$$\chi^2_{\mu_{app}}(\boldsymbol{\theta}\,;\,\boldsymbol{\kappa}) = \sum_i \left[\frac{\mu_{app,i}^{model}(\boldsymbol{\theta}\,;\,\boldsymbol{\kappa}) - \mu_{app,i}^{obs}}{\max(\mu_{app}^{obs})}\right]^2 . \tag{5.19}$$

It is important to note that procedures lacking saturation monitoring necessitate the estimation of S_w from (f_g, μ_{app}), as detailed in Eq. (5.13). This issue may become more

significant for complex models that do not permit analytical inversion, as Corey-Brooks (Eq. (5.13)).

5.4.1.0.2 Mobility Reduction Factor Approach

Given the observed mobility reduction factor MRF^{obs} (Eq. (5.16)), find foam parameters $\boldsymbol{\theta}$ that minimizes

$$\chi^2_{MRF}(\boldsymbol{\theta}) = \sum_i \left[\frac{MRF_i^{model}(\boldsymbol{\theta}) - MRF_i^{obs}}{\max(MRF^{obs})} \right]^2 . \tag{5.20}$$

A key advantage of the MRF approach is that it estimates foam parameters without requiring prior knowledge of relative permeability functions.

Both optimization problems were carried out using the differential evolution (DE) method, a population-based stochastic search algorithm (Storn and Price, 1997; Price, 2013), and relied on the following settings across all scenarios: a population size of 500 individuals for the DE method evolved over 500 generations within the parameter space limited by physical constraints presented in Table 11.

Table 11 – Parameter bounds used in differential evolution optimization.

Parameter	Lower Bound	Upper Bound
fmmob	10^3	10^7
fmdry	S_{wc}	$1.0 - S_{gr}$
epdry	10^1	10^5
fmsurf	10^{-2}	2.0
epsurf	10^{-2}	5×10^1

5.4.2 Profile Likelihood Analysis

Parameter identifiability is a fundamental aspect to support reliable model calibration. Profile likelihood (PL) analysis is a technique for assessing practical and structural identifiability by examining the objective-function topology in the vicinity of optimal values (Raue et al., 2009), thereby highlighting correlation structures and potential ambiguities in parameter estimation.

The PL method involves fixing each parameter of interest at specified values while optimizing the remaining parameters to minimize the objective function. To this end, in this chapter, each parameter was systematically varied within ±50% of reference values, generating 200 evaluation points per profile. At each fixed parameter value, 20 independent optimization runs of the DE method were performed with randomized initial populations to ensure robust convergence and capture potential local minima.

Three distinct scenarios were examined to evaluate the influence of relative permeability characterization on foam parameter identifiability:

1. The first scenario represents ideal conditions where the apparent viscosity objective function presented in Eq. (5.19) is minimized using ground truth relative permeability functions. This baseline establishes the intrinsic identifiability limits of foam parameters under perfect knowledge of multiphase flow properties.

2. The second scenario employs again the apparent viscosity objective function, Eq. (5.19). However, it adopts a misspecified relative permeability function, particularly assuming the Brooks-Corey functions instead of the LET functions, illustrated in Figure 35, the subtle yet critical model discrepancy. It represents the common experimental conditions where relative permeability characterization contains uncertainties in model specification and parameter fitting.

3. The third scenario evaluates the mobility reduction factor formulation, presented in Eq. (5.20), which, by construction, eliminates direct dependence on relative permeability functions during optimization.

5.4.3 Relative Permeability Uncertainty Quantification

Following the establishment of parameter identifiability through profile likelihood analysis, an uncertainty quantification analysis was carried out to assess the robustness of each foam parameter estimation approach. This evaluation analyzes how uncertainties in relative permeability characterization propagate through the parameter estimation process and influence the reliability of the estimated foam parameters.

To evaluate uncertainties, we regenerated the data by sampling the Corey-Brooks relative permeability parameters, $\boldsymbol{\kappa} = \{n_w, n_g, k^0_{rw}, k^0_{rg}\}$, using Latin Hypercube Sampling (Iman and Conover, 1982). The parameters were sampled from Gaussian distributions centered at their ground truth values ($n_w = 2.86$, $n_g = 0.7$, $k^0_{rw} = 0.39$, and $k^0_{rg} = 0.59$) with a $\pm 10\%$ variation, generating 2^{13} parameter sets that span the uncertainty space.

For each sampled relative permeability parameter set, two estimation pathways were evaluated to enable direct comparison between the strategies presented in Figure 37. The apparent viscosity approach employs the perturbed relative permeability functions in μ_{app} calculations during foam parameter optimization, representing the conventional method where relative permeability characterization uncertainties directly affect the estimation process (for further details see Eftekhari and Farajzadeh (2017)).

The *MRF* approach utilizes the same perturbed relative permeability functions to generate reference pressure drop values ΔP_{ref}, which, combined with foam experiment pressure drops ΔP_{foam}, are used to calculate *MRF* values according to Eq. (5.16). Foam parameters are subsequently estimated using just the *MRF* dataset without relying on relative permeability knowledge functions during optimization. While in the apparent viscosity approach, monitoring water saturation is just an optional step, it assumes a

relative permeability function, which introduces epistemic uncertainty. In contrast, the *MRF* approach does require monitoring saturations but does not make any assumptions about the relative permeability.

5.5 RESULTS

We begin by presenting the alignment of the proposed *MRF* expression for characterizing foam experimental data to the `STARS` foam model. We then present the results of the methods discussed in the preceding section, which were used to evaluate parameter identifiability and to quantify uncertainty associated with variability in the relative permeability function.

5.5.1 Mobility reduction factor

Figure 34 shows the `STARS` model evaluation using the ground-truth parameters (solid line) compared to *MRF* computed with Eq. (5.11) (cross) or Eq. (5.16) (dot) for three selected surfactant concentrations. First, it is evident that the proposed expression for *MRF* quantification aligns more closely with the data obtained using the `STARS` foam mathematical model. Moreover, as the surfactant concentration increases and the foam strengthens, the proposed *MRF* appears to be less sensitive to noise.

5.5.2 Parameter Identifiability

Figure 38 presents the profile likelihood results for three scenarios: apparent viscosity objective function with known relative permeability functions (μ_{app}^{LET}, using the ground truth parameters), apparent viscosity objective function with a mismatch in relative permeability functions (μ_{app}^{Corey}), and mobility reduction factor objective function (*MRF*). Each column represents a different profiled parameter.

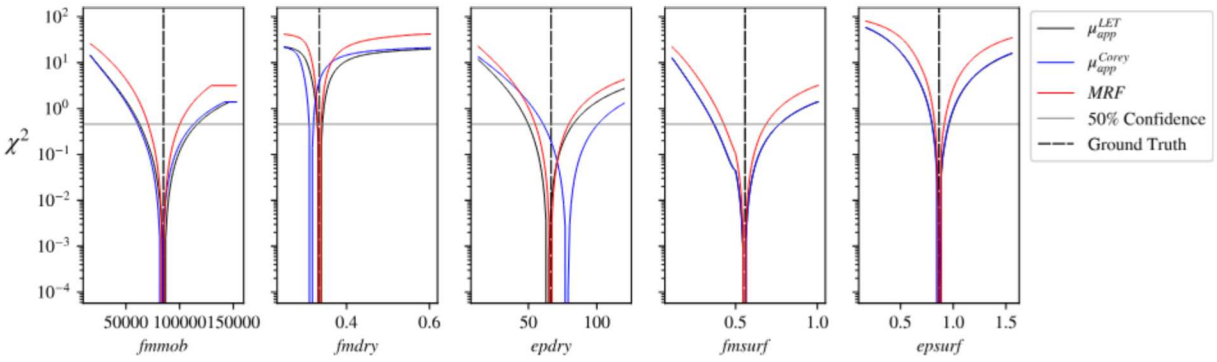

Figure 38 – Profile likelihood analysis for foam parameter estimation under three scenarios: μ_{app}^{LET}: apparent viscosity objective function assuming the correct relative permeability functions that generated the data (LET); μ_{app}^{Corey}: apparent viscosity objective function assuming assuming wrong relative permeability functions (Corey); *MRF*: mobility reduction factor objective function, no relative permeability assumptions. Vertical lines indicate ground truth parameter values.

In the first scenario (Figure 38, solid black line), the profile likelihood exhibits well-defined minima within the confidence threshold of 50% for all foam parameters when using the apparent viscosity approach with correct relative permeability functions (without uncertainty in relative permeability). This confidence threshold defines the range of acceptable parameter estimates that maintain at least half of the maximum likelihood. The formulation that incorporates the mobility reduction factor into the objective function (Figure 38, solid red line) also demonstrates close agreement with the ground truth parameters.

The case where noise is introduced in the relative permeability functions to represent difficulties in their estimation significantly impacts the identifiability profiles, as shown in the blue lines in Figure 38. Notable deviations from the ground truth values occur for *fmdry* and *epdry*, with the objective function minima shifting substantially from their true positions. Although the mismatch in *fmdry* seems small, it is important to recognize that even minor deviations in this parameter can have a substantial effect on model predictions (Valdez et al., 2022).

Table 12 summarizes the foam parameter estimation results for each approach. The apparent viscosity method produced significant errors, as it incorrectly attributed the relative permeability model (mismatch) to foam effects. In contrast, the *MRF* approach, being agnostic to the permeability model, closely approximated the true foam parameters.

Table 12 – Parameter estimation comparison between μ_{app} and *MRF* methods considering LET relative permeability for data generation.

		Estimate (Absolute Relative Error)		
Parameter	**Ground Truth**	μ_{app} **w/** ***Corey***	μ_{app} **w/** ***LET***	***MRF***
fmmob [10^5]	0.849	0.830 (2.24%)	0.854 (0.58%)	0.845 (0.49%)
fmdry [10^{-1}]	3.344	3.148 (5.88%)	3.354 (0.30%)	3.345 (0.02%)
epdry [10^1]	6.666	7.846 (17.70%)	6.435 (3.46%)	6.606 (0.90%)
fmsurf [10^{-1}]	5.580	5.532 (0.87%)	5.524 (1.00%)	5.540 (0.72%)
epsurf [10^{-1}]	8.649	8.648 (0.01%)	8.673 (0.28%)	8.659 (0.12%)

5.5.3 Uncertainty Propagation from Relative Permeability Functions

The uncertainties in the relative permeability parameters $\boldsymbol{\kappa}$ are propagated to the model outputs, namely the apparent viscosity and the mobility reduction factor. To evaluate the impact on the estimated parameters, we conduct multiple runs of the parameter estimation process.

First, we show in Figure 39 (left panel) the uncertainties from relative permeability parameters to the relative permeability functions. On the right panel of Figure 39, we show the result of propagating the relative permeability uncertainties to the no-foam reference pressure drop, which is required for the *MRF* approach.

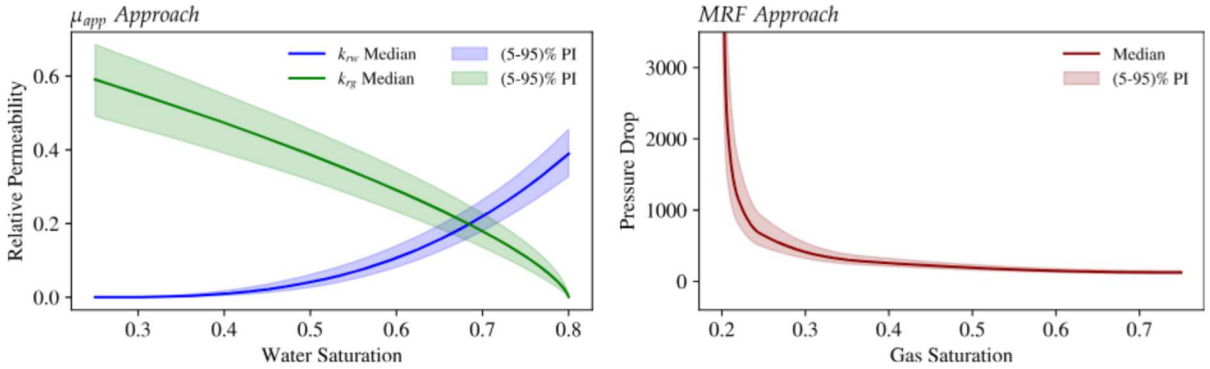

Figure 39 – Propagated uncertainties from relative permeability parameters to the relative permeability functions (left) and to the reference pressure drop (right).

Next, we carried out 2^{13} parameter estimation runs to provide a statistically robust characterization of bias and variance in estimated foam parameters under uncertainty in relative permeability in order to compare the approaches using μ_{app} or *MRF*. Table 13 presents a comparison of the maximum error committed when using the two different approaches. The maximum relative errors demonstrate that the *MRF* approach consistently yields better approximations for the dry-out parameters (*fmdry* and *epdry*). On the other hand, both methods show similar performance for the other parameter estimation. The improved performance of the *MRF* method observed in Table 4 stems from its theoretical consistency with the gas-only mobility reduction hypothesis. While the μ_{app} approach relies on inversion of relative permeability models to estimate water saturation, the *MRF* method requires explicit saturation monitoring. This direct measurement of water saturation is especially advantageous for estimating dry-out parameters (*fmdry*, *epdry*), which are strongly connected to water saturation behavior. By eliminating the need for relative permeability inversions and directly measuring the saturation that controls foam dry-out, the *MRF* approach drastically reduces uncertainty in these critical parameters.

Table 13 – Comparison of estimated values from both approaches and their relative error against the ground truth (GT) values.

		Maximum Error (Relative Error)	
Parameter	**GT**	μ_{app} **Approach**	***MRF* Approach**
fmmob $[10^5]$	0.849	0.516 (-39.28%)	0.506 (-40.47%)
fmdry $[10^{-1}]$	3.344	3.977 (18.91%)	3.328 (-0.48%)
epdry $[10^1]$	6.666	13.810 (107.11%)	6.385 (-4.21%)
fmsurf $[10^{-1}]$	5.580	4.585 (-17.84%)	5.925 (6.18%)
epsurf $[10^{-1}]$	8.649	9.152 (5.82%)	8.837 (2.18%)

A more detailed analysis of the estimated parameters is presented in Figure 40 that compares the fitting results of the two approaches in a joint plot of the estimated values $\boldsymbol{\theta}$ for sampled relative permeability parameters $\boldsymbol{\kappa}$. For all parameters except *fmmob*, the μ_{app} approach produces a wider spread of estimated parameter values than the *MRF* approach,

indicating a greater propagation of uncertainties in these parameters. With respect to Figure 40, we can also note that the *MRF* approach for foam parameter estimation reduces the range of estimated parameters, and consequently, the associated uncertainties, particularly for the *epdry* and *fmdry* parameters. This improvement stems from the *MRF* approach explicitly incorporating information about water saturation.

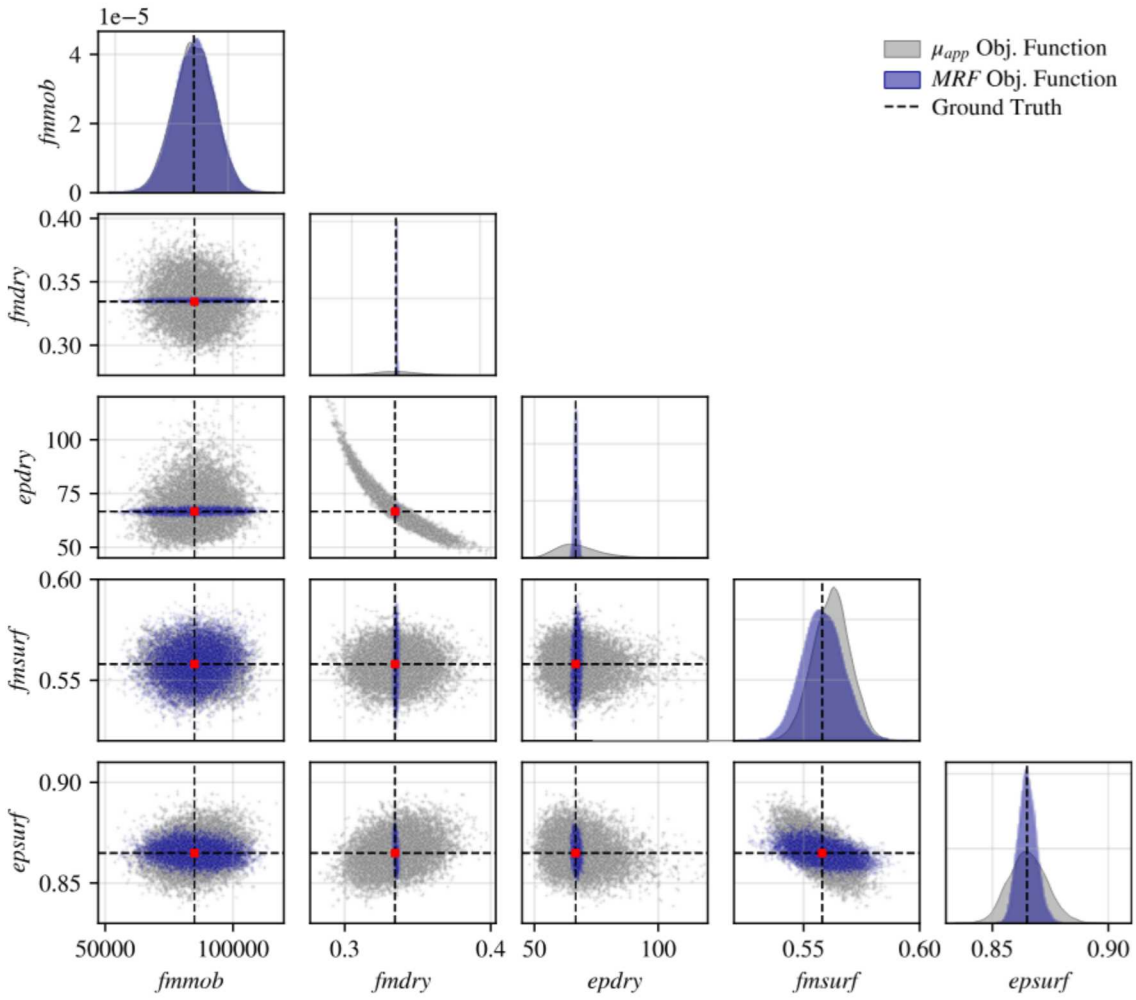

Figure 40 – Comparison of foam parameter estimates from apparent viscosity (gray) and *MRF* (blue) approaches across 8192 relative permeability realizations.

5.6 DISCUSSION

5.6.1 Relative Permeability Models

The proposed *MRF* approach, while requiring saturation monitoring, which can be obtained through CT (Simjoo et al., 2013), NMR (Amirmoshiri et al., 2018), or mass balance calculations (Ma et al., 2013), provides parameters less affected by epistemic uncertainties from relative permeability assumptions. Recent studies on uncertainty quantification of relative permeability models (Berg et al., 2021b, 2024; Valdez et al., 2020; Ribeiro et al., 2024) have shown that these uncertainties can substantially affect production factors. Therefore, in scenarios where relative permeabilities are highly uncertain, the

direct measurement of water saturation in the *MRF* approach also provides an advantage for estimating dry-out parameters, which are highly sensitive to water saturation, reducing uncertainty propagation.

The *MRF* approach becomes particularly relevant when considering more complex relative permeability models, such as LET (Lomeland et al., 2005), which include additional parameters for endpoint curvature and transition behavior. Assumptions regarding the estimated values for the relative permeability parameters enable the foam parameter estimation to adjust to the studied dataset and indicate a best estimation set, although it does not accurately represent the actual mobility reduction provided by foam (see Figure 38 and Tables 12 and 13).

The *MRF* approach circumvents this mathematical limitation by relying solely on the observed pressure drop and saturation for core flooding experiments (with and without foam). This flexibility sets the estimation of relative permeability as a subsequent step or even a possibility to estimate together with the foam parameters. It avoids bias from functional form assumptions and enables hypothesis testing during the parameter estimation procedure, such as the variation in the residual saturations due to the presence of foam (Mehrabi et al., 2022).

5.6.2 Mobility Reduction Factor Definition

Beyond the parameter fitting capability, the lack of standardized definitions for experimental *MRF* (Rosman and Kam, 2009; Simjoo et al., 2013; Sri Hanamertani et al., 2021; AlYousef et al., 2023; Bello et al., 2023c; Jia et al., 2024) creates challenges for data interpretation and cross-study comparisons. This inconsistency in experimental protocols produces *MRF* values that, while sharing nomenclature with the implicit-texture model parameter, represent fundamentally different physical quantities (see Figure 34). Different experimental *MRF* definitions (involving reference conditions such as continuous brine injection, continuous gas injection, or water-gas co-injection) yield values that cannot be directly compared or converted into implicit-texture foam parameters without additional data. Without standardization, the same foam system characterized in different laboratories produces *MRF* values that represent distinct physical quantities despite identical nomenclature.

Although this study focuses exclusively on the effects of surfactant concentration and water saturation, the *MRF* approach is capable of capturing other foam behaviors, such as shear-thinning effects. However, fitting parameters associated with these additional behaviors would require further data, which have been simplified in the present analysis to consider only dry-out and surfactant effects.

To further demonstrate the applicability of the proposed *MRF* expression, we present an additional analysis using the experimental data provided by Kapetas et al.

(2015). Figure 41 illustrates the *MRF* values using the proposed expression for the experimental data of the foam-quality scan presented by Kapetas et al. (2015), along with the fitted parameters from Valdez et al. (2022) used to simulate both the reference pressure drop and the corresponding ground-truth function. This demonstrates that Eq. (5.16) remains applicable to other foam physics, such as the non-Newtonian behavior, and may also extend to additional contexts, as long as saturation matching between the reference and foam experiments is preserved.

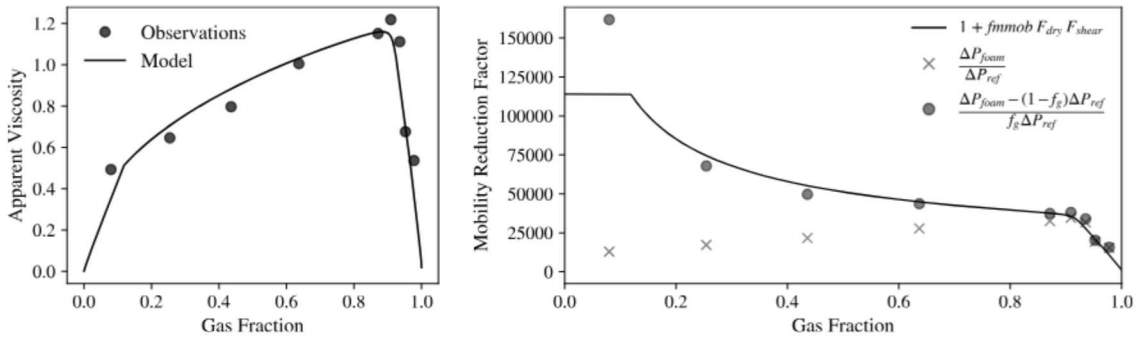

Figure 41 – *MRF* approach validation on data from Kapetas et al. (2015) with active F_{shear} effects showing good agreement between calculated and theoretical values.

5.6.3 Injected Surfactant Concentrations

Including F_{surf} in the model while using data from a single surfactant concentration may result in identifiability issues. The optimization cannot distinguish between the reference foam strength (*fmmob*) and the concentration-dependent scaling, leading to parameter correlation and non-unique parameters. This coupling manifests as flattened profile likelihood curves or oscillations for both *fmmob* and surfactant parameters. To illustrate this behavior, we conducted the profile likelihood analysis using data from increasing surfactant concentrations (Figure 42). The results suggest that the non-identifiability cases observed in Figure 42 (corresponding to the first three cases) arise because the experimental procedure lacks the necessary variation in surfactant concentrations to properly constrain the F_{surf} terms. This issue is due to the absence of data, rather than the estimation method used, whether the proposed *MRF* approach or the traditional μ_{app} approach. Particularly, in the case examined, at least three surfactant concentrations are needed to prevent identifiability issues, as shown in the bottom panel.

5.6.4 Translation to field scale

Although upscaling introduces additional complexities, such as heterogeneity and gravitational effects, robust laboratory-scale characterization is the fundamental basis for reliable field models. Field implementation typically employs history matching to refine laboratory-derived parameters using early production data (Alcorn et al., 2022; Sæle et al., 2022). As shown in Table 3, the proposed *MRF* approach yields lower estimation

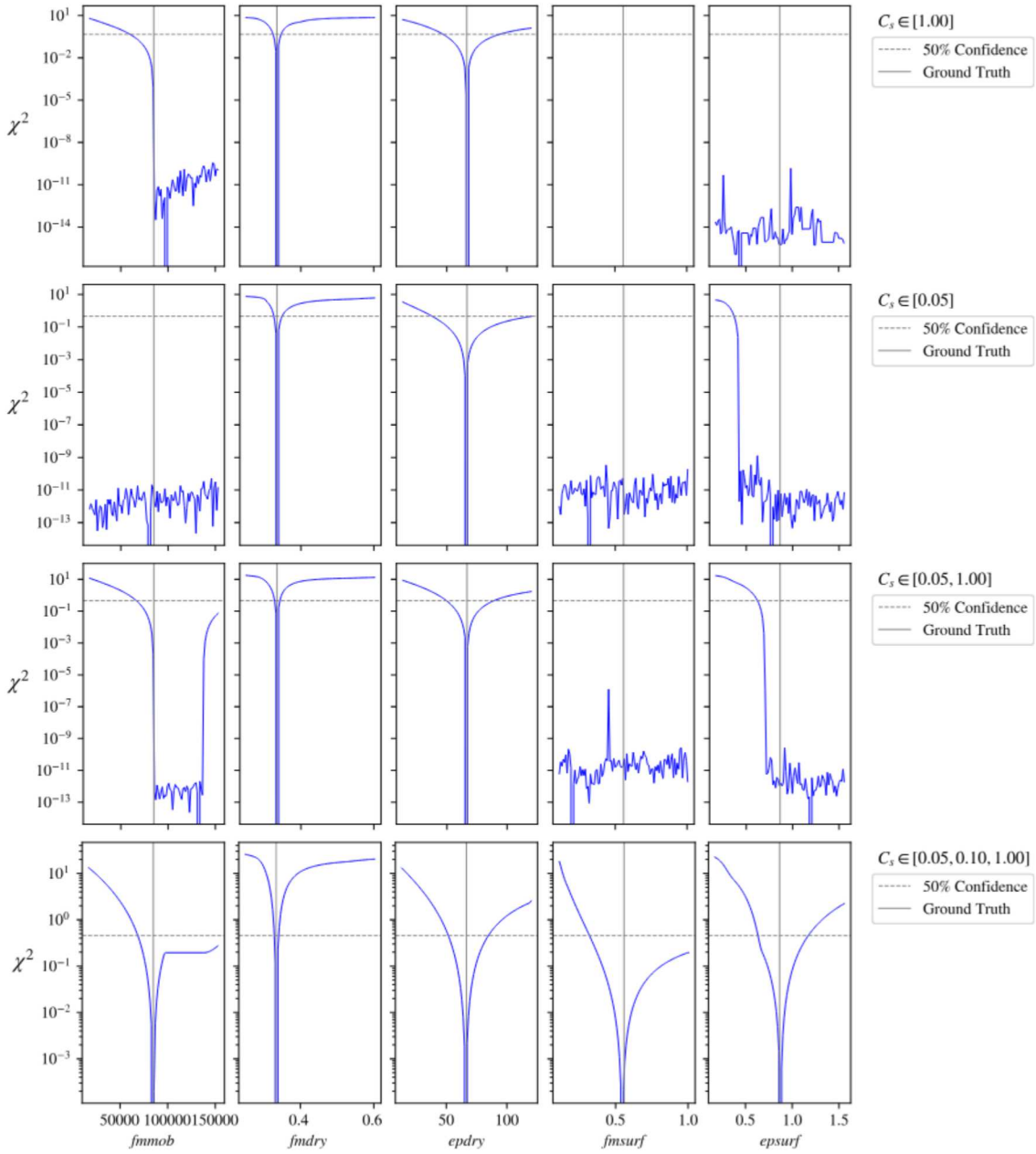

Figure 42 – Profile likelihood analysis showing parameter identifiability improvement with increasing surfactant concentration data points.

errors for critical foam parameters, particularly *fmmob*, *fmdry*, and *epdry*, compared to the conventional μ_{app} approach. These parameters control the foam strength and the dry-out behavior, which are essential for predicting foam propagation and stability in reservoirs. Reduced uncertainties in these parameters lead to more accurate field-scale predictions of foam performance, including sweep efficiency and oil recovery. In contrast, the μ_{app} approach introduces larger errors that propagate to field models, potentially leading to suboptimal foam application designs and unfavorable economic outcomes. Consequently, uncertainties originating from core-flooding parameter estimation are inevitably transferred to field-scale simulations (Sharma et al., 2020; de Moura Ribeiro et al., 2025).

Biased parameter estimations from uncertain lab estimates either propagate to field predictions or are compensated through adjustments to reservoir properties during history matching. This misattribution obscures sources of uncertainty and reduces physical consistency in forecasts. While this work does not address upscaling or field-scale translation, it strengthens the core-scale characterization essential for field-level modeling.

5.6.5 Applicability and Limitations

The proposed *MRF* method requires saturation monitoring and a no-foam reference experiment at matching saturations, which may not be feasible in all laboratory settings. In summary, the choice between methods for foam parameter estimation should consider: (1) when relative permeability is well-characterized (low uncertainty), both methods are applicable, though *MRF* typically provides lower uncertainty due to its circumvention of relative permeability assumptions; (2) when relative permeability is highly uncertain, *MRF* is preferred; (3) when saturation monitoring is unavailable, the traditional μ_{app} method may be the only option. In addition, we note that if relative permeability models, such as the LET model, are to be employed, the *MRF* method remains the preferred choice, since inverting the LET model is not straightforward. The decision should balance experimental capabilities, required accuracy, and the intended application, as foam parameter estimation is critical for accurate field-scale predictions, where the reliability of parameters significantly impacts forecasts.

5.7 CONCLUSIONS

This study presented an alternative approach for foam parameter estimation in implicit-texture models, which is based on the definition of an alternative mobility reduction factor expression. The proposed approach introduces the foam quality f_g value into the *MRF* formula to circumvent the need for relative permeability functions assumption during the estimation of foam parameters. The derived expression provides a standardized metric for comparing foam strength across experiments and laboratories, and serves as an alternative method for parameter estimation.

We employed the LET relative permeability functions with the foam implicit-texture model implemented in `STARS` to generate the data and validate the approach's capacity to circumvent model assumptions. The analysis of parameter identifiability showed that both the surfactant-related parameters and the dry-out parameters can be reliably estimated using the proposed formulation. Both approaches studied require conducting foam quality scan experiments at a sufficient range of injected concentrations to prevent issues with parameter identifiability.

The *MRF* formulation provides direct physical interpretability and facilitates meaningful comparisons between foam characterization studies conducted under different experimental conditions. Moreover, uncertainty quantification revealed that the *MRF* approach enabled more robust parameter estimation by consistently producing lower parameter estimation variances compared to the apparent viscosity approach, particularly for the dry-out parameters *fmdry* and *epdry*. This reduction in uncertainty propagation represents a significant advantage for experimental characterization of foam behavior.

6 CONCLUSIONS

Modeling foam flow in porous media requires a comprehensive treatment of parametric uncertainties to enable reliable predictions for enhanced oil recovery applications. The improved parameter estimation approaches and uncertainty quantification techniques developed in this work address challenges in foam flow characterization by integrating Bayesian inference, numerical simulations, and surrogate modeling. This work establishes methods for quantifying uncertainties in implicit-texture foam models across two-phase and three-phase systems, progressing from coupled parameter estimation to direct characterization approaches. It also provides an important link between experimental design and parameter estimation, strengthening the reliability of numerical simulations and predictive modeling.

In the first part of the thesis (Chapter 3), we demonstrated the interplay between relative permeability and foam parameters in two-phase flow systems by performing a simultaneous inverse uncertainty quantification. The results revealed strong correlations between parameters traditionally estimated independently, particularly between the water relative permeability exponent and the critical water saturation for foam stability. These correlations suggest that assuming relative permeability functions not derived from specific experimental conditions can substantially impact foam parameter estimation, potentially leading to biased predictions and misleading interpretations of foam effectiveness. Additionally, the polynomial chaos expansion for surrogate modeling enabled efficient uncertainty propagation in transient simulations, revealing that parameter sensitivities vary significantly across different flow regimes. While $fmmob$ controls the variance of foam strength in the low-quality regime, n_w and $SF/fmdry$ interactions dominate high-quality regime behavior. Analysis of gas breakthrough times further demonstrated that the relative importance of these parameters shifts with injection conditions: water relative permeability governs the response at low gas fractions, whereas foam stability parameters become dominant at high gas fractions. These findings highlight the importance of accurately determining both model components (relative permeability and foam parameters), with special attention to their potential interactions.

The second part of the thesis, presented in Chapter 4, advances the framework by extending the uncertainty quantification analysis to three-phase foam–oil flow. In particular, an improved parameter estimation method for the foam parameters related to oil saturation was developed and evaluated under different conditions. The approach was validated using both synthetic data and literature cases, including oil bank formation. The results suggest that experimental designs should increase oil injection in gradual steps with saturation monitoring to span the range required for reliable parameter estimation. Two-dimensional heterogeneous reservoir simulations illustrated that single best-estimate

parameters derived from sparse datasets produce substantially different flow behavior compared to the true system response. Furthermore, strong correlations between oil destabilization function parameters indicated identifiability challenges. While the propagated uncertainties exhibited low variation in the F_{oil} function itself, these uncertainties significantly affected simulator responses, particularly in scenarios with low initial oil saturations, which are characteristic of depleted reservoirs implementing FAWAG as a tertiary recovery method.

The third part of the thesis, presented in Chapter 5, introduced an alternative parameter estimation method based on the mobility reduction factor term, utilizing the pressure drop measurements from steady-state experiments with and without foam. This approach eliminates the usage of relative permeabilities in the process and, therefore, eliminates epistemic uncertainties associated with relative permeability parameters, which traditionally introduce modeling assumptions and propagate errors through multi-step procedures. An identifiability analysis indicated that surfactant-related foam parameters require experiments spanning multiple surfactant concentrations for reliable estimation. Moreover, the proposed method based on a new MRF expression enables the incorporation of more sophisticated relative permeability models, such as LET, for foam flow in porous media, an aspect that has not been addressed in the literature to date.

In summary, this work advanced the understanding of foam flow modeling in porous media by applying uncertainty quantification techniques to link experimental data with numerical simulations effectively. Incorporating uncertainties into computational models improves the reliability of foam flow simulators and provides quantitative criteria for parameter estimation. This work refined the calibration of three-phase foam flow simulators by accounting for experimental uncertainties. The methods developed herein may guide experimental design by identifying minimum data requirements and optimal measurement strategies for parameter estimation. These contributions enable practitioners to evaluate the adequacy of experimental datasets and maintain quantified confidence in foam flow predictions for enhanced oil recovery applications.

6.1 PRACTICAL GUIDELINES

The results of this study may be translated as practical guidelines for foam-assisted EOR applications, aiding in the risk-aware planning of foam injection projects:

1. **Experimental Design**: Characterizing the effects on foam, such as oil saturation and surfactant concentration, requires comprehensive data coverage related to these effects. Therefore, experiments should avoid sudden changes in foam strength to ensure that variations in the variable of interest are meaningful.

2. **Foam Characterization**: A standard measurement for the MRF term, defined as

the relative pressure increase per unit of injected gas fraction, enables cross-study comparisons of foam strength and allows for the characterization of parameters while circumventing assumptions about relative permeability, thus avoiding misleading forecasts of foam performance.

3. **Probabilistic Forecasting**: Parameter uncertainty, modeled by probability distributions, can be propagated through reservoir-scale simulations to provide more robust information for operational decisions. Uncertainty-aware forecasts offer significantly more reliability than single best-estimate predictions.

4. **Surrogate Modeling**: Emlulator-based approaches, such as PCE, enable computationally tractable propagation of foam parametric uncertainties for field-scale studies while maintaining prediction capability from robust simulators.

6.2 LIMITATIONS AND FUTURE WORK

This work employed implicit-texture foam models throughout the uncertainty quantification framework. While computationally tractable for parameter estimation, these models represent foam dynamics through empirical correlations rather than mechanistic descriptions of bubble generation, coalescence, and transport (Lozano et al., 2021).

The UQ approaches assume parameter transferability from core samples to a heterogeneous reservoir. However, the parameter uncertainties quantified at the core scale may amplify when applied to field-scale predictions due to additional complexities related to subsurface modeling that are not fully captured by laboratory experiments (Hirasaki, 1989; Patzek and Myhill, 1989; Patzek, 1996).

In the literature, modeling the three-phase relative permeability function itself is a considerable challenge in fluid dynamics (Alizadeh and Piri, 2014). It becomes even more complex when the presence of foam is considered (Farajzadeh et al., 2012). One of the possible observed effects from the presence of foam in three-phase flows is the reduction of residual oil (Farajzadeh et al., 2012; Sun et al., 2015). Modeling relative permeability for this purpose introduces complexity in parameter estimation. A straightforward future work is to combine the direct *MRF* characterization method from Chapter 5 with three-phase foam-oil systems, allowing for the estimation of foam parameters without relying on assumptions about relative permeability.

Additionally, the proposed UQ approaches can be used for the more sophisticated models mentioned earlier to account for researching other effects on foam. The techniques presented here enable probabilistic/ensemble forecasting for probabilistic risk assessment (Zhu, 2005; Tartakovsky, 2007; Leutbecher and Palmer, 2008; Cushman and Tartakovsky, 2016), resulting in more robust foreknowledge to guide foam-assisted EOR planning or feed studies of optimization under uncertainty.

6.3 ACADEMIC CONTRIBUTIONS

This work led to several academic contributions, which are outlined below:

1. Modeling Foam Flow in Porous Media Influenced by Oil: A Computational Framework for Improved Parameter Estimation (submitted).

2. Uncertainty Quantification on Foam Modeling: The Interplay of Relative Permeability and Implicit-texture Foam Parameters. Transport in Porous Media 152, 8, 2025. doi: 0.1007/s11242-024-02137-1.

3. On the identifiability of relative permeability and foam displacement parameters in porous media flow. Water Resources Research, 2024, 60.3: e2023WR036751. doi: 10.1029/2023WR036751.

4. Characterization of Foam-Assisted Water-Gas Flow via Inverse Uncertainty Quantification Techniques. In: International Conference on Computational Science. Cham: Springer International Publishing, 2022. p. 310-322. doi: 10.1007/978-3-031-08760-8_26.

5. An Improved Approach for Uncertainty Quantification Based on Steady-State Experimental Data in Foam-Assisted Enhanced Oil Recovery. In: ECMOR 2022. European Association of Geoscientists & Engineers, 2022. p. 1-14. doi: 10.3997/2214-4609.202244048.

6. A workflow for uncertainty quantification of numerical models for foam-based EOR. In: Rio Oil & Gas 2022: Technical Papers. IBP. 2022. v. 179. p. 1. doi: 10.48072/2525-7579.rog.2022.179.

While items 3-6 are relevant to the overall theme of this work, they have not been included in full to maintain objectivity and conciseness. The contents of this work were also presented and discussed at scientific events, including the following presentations:

- 28th Encontro Nacional de Modelagem Computacional, 1-4 October 2024, Ilhéus-BA, Brazil. Title: Estimação de parâmetros do modelo de textura implícita de espuma para escoamentos trifásicos em meios porosos.

- 6th Brazil InterPore Conference on Porous Media, 7–9 August 2023, Campinas-SP, Brazil. Title: Improving the inverse uncertainty quantification in foam-assisted enhanced oil recovery using physically based priors.

- SIAM Conference on Mathematical & Computational Issues in the Geosciences, 19–22 June 2023, Bergen, Norway. Title: Improving the Inverse Uncertainty Quantification in Foam-Assisted Enhanced Oil Recovery

- 15th Annual Meeting of InterPore 2023. 22–25 May 2023, Edinburgh, Scotland. Title: Improved techniques for uncertainty quantification of foam flow in porous media.
- 14th Annual Meeting of InterPore, 30 May–2 June 2022, Abu Dhabi, United Arab Emirates. Title: Inverse and forward uncertainty quantification of relative permeability and foam model parameters for EOR processes.
- Rio Oil & Gas 2022, 26–29 September 2022, Rio de Janeiro-RJ, Brazil. Title: A workflow for uncertainty quantification of numerical models for foam-based EOR
- 18th European Conference on the Mathematics of Oil Recovery, 5–7 September 2022, The Hague, Netherlands. Title: An Improved Approach for Uncertainty Quantification Based on Steady-State Experimental Data in Foam-Assisted Enhanced Oil Recovery.

REFERENCES

A. R. Adebayo. A Graphical Interpretation Technique to Evaluate Strength and Stability of Foam in Porous Media Based on Mobile-Trapped Foam Ratio. *Transport in Porous Media*, 139(2):327–355, September 2021. ISSN 1573-1634. doi: 10.1007/s11242-021-01668-1.

A. Afsharpoor, G. S. Lee, and S. I. Kam. Mechanistic simulation of continuous gas injection period during surfactant-alternating-gas (SAG) processes using foam catastrophe theory. *Chemical Engineering Science*, 65(11):3615–3631, June 2010. ISSN 0009-2509. doi: 10.1016/j.ces.2010.03.001.

Z. P. Alcorn, Aleksandra Sæle, Metin Karakas, and Arne Graue. Unsteady-state co2 foam generation and propagation: Laboratory and field insights. *Energies*, 15(18):6551, 2022. ISSN 1996-1073. doi: 10.3390/en15186551.

A. H. Alizadeh and M. Piri. Three-phase flow in porous media: A review of experimental studies on relative permeability. *Reviews of Geophysics*, 52(3):468–521, 2014. ISSN 1944-9208. doi: 10.1002/2013RG000433.

A. Almaqbali, V. E. Spooner, S. Geiger, D. Arnold, and E. Mackay. Uncertainty quantification for foam flooding in fractured carbonate reservoirs. In *SPE Reservoir Simulation Conference*. OnePetro, 2017.

Z. AlYousef, A. Gizzatov, H. AlMatouq, and G. Jian. Assessment of foam generation and stabilization in the presence of crude oil using a microfluidics system. *Journal of Petroleum Exploration and Production Technology*, 13(4):1155–1162, April 2023. ISSN 2190-0566. doi: 10.1007/s13202-022-01604-z.

M. Amirmoshiri, Y. Zeng, Z. Chen, P. M. Singer, M. C. Puerto, H. Grier, R. Z. Kamarul Bahrim, S. Vincent-Bonnieu, R. Farajzadeh, S. L. Biswal, and G. J. Hirasaki. Probing the Effect of Oil Type and Saturation on Foam Flow in Porous Media: Core-Flooding and Nuclear Magnetic Resonance (NMR) Imaging. *Energy & Fuels*, 32(11):11177–11189, November 2018. ISSN 0887-0624. doi: 10.1021/acs.energyfuels.8b02157.

P. Arias, N. Bellouin, E. Coppola, R. Jones, G. Krinner, J. Marotzke, V. Naik, M. Palmer, G. Plattner, J. Rogelj, et al. Climate change 2021: the physical science basis. contribution of working group i to the sixth assessment report of the intergovernmental panel on climate change; technical summary, 2021.

E. Ashoori, D. Marchesin, and W. R. Rossen. Roles of transient and local equilibrium foam behavior in porous media–traveling wave. In *ECMOR XII-12th European Conference on the Mathematics of Oil Recovery*, pages cp–163. European Association of Geoscientists & Engineers, 2010.

H. Bazargan, M. Christie, A. H. Elsheikh, and M. Ahmadi. Surrogate accelerated sampling of reservoir models with complex structures using sparse polynomial chaos expansion. *Advances in Water Resources*, 86:385–399, December 2015. ISSN 0309-1708. doi: 10.1016/j.advwatres.2015.09.009.

J. Bear and Y. Bachmat. *Introduction to Modeling of Transport Phenomena in Porous Media*. Springer Science & Business Media, December 2012. ISBN 978-94-009-1926-6.

A. Bello, A. Ivanova, and A. Cheremisin. A Comprehensive Review of the Role of CO2 Foam EOR in the Reduction of Carbon Footprint in the Petroleum Industry. *Energies*, 16(3):1167, January 2023a. ISSN 1996-1073. doi: 10.3390/en16031167.

A. Bello, A. Ivanova, and A. Cheremisin. Foam EOR as an Optimization Technique for Gas EOR: A Comprehensive Review of Laboratory and Field Implementations. *Energies*, 16(2):972, January 2023b. ISSN 1996-1073. doi: 10.3390/en16020972.

A. Bello, A. Ivanova, A. Rodionov, A. aand Rodionov, T. Aminev, A. Mishin, A. Mishin, D. Bakulin, P. Grishin, P. Belovus, A. Penigin, K. Kyzyma, and A. Cheremisin. An Experimental Study of High-Pressure Microscopy and Enhanced Oil Recovery with Nanoparticle-Stabilised Foams in Carbonate Oil Reservoir. *Energies*, 16(13):5120, January 2023c. ISSN 1996-1073. doi: 10.3390/en16135120.

S. Berg, E. Unsal, and H. Dijk. Non-uniqueness and uncertainty quantification of relative permeability measurements by inverse modelling. *Computers and Geotechnics*, 132: 103964, 2021a.

S. Berg, E. Unsal, and H. Dijk. Sensitivity and uncertainty analysis for parameterization of multiphase flow models. *Transport in Porous Media*, 140(1):27–57, 2021b.

S. Berg, H. Dijk, E. Unsal, R. Hofmann, B. Zhao, and V. Raju Ahuja. Simultaneous determination of relative permeability and capillary pressure from an unsteady-state core flooding experiment? *Computers and Geotechnics*, 168:106091, 2024. ISSN 0266-352X. doi: https://doi.org/10.1016/j.compgeo.2024.106091. URL `https://www.sciencedirect.com/science/article/pii/S0266352X24000272`.

G. G. Bernard and L. Holm. Effect of foam on permeability of porous media to gas. *Society of Petroleum Engineers Journal*, 4(03):267–274, 1964. doi: 10.2118/983-PA.

G. G. Bernard and W. L. Jacobs. Effect of Foam on Trapped Gas Saturation and on Permeability of Porous Media to Water. *Society of Petroleum Engineers Journal*, 5(04): 295–300, December 1965. ISSN 0197-7520. doi: 10.2118/1204-PA.

H. J. Bertin, O. G. Apaydin, L. M. Castanier, and A. R. Kovscek. Foam Flow in Heterogeneous Porous Media: Effect of Cross Flow. *SPE Journal*, 4(02):75–82, June 1999. ISSN 1086-055X. doi: 10.2118/56009-PA.

M. Betancourt. A Conceptual Introduction to Hamiltonian Monte Carlo, July 2018.

M. J. Betancourt and Mark Girolami. Hamiltonian Monte Carlo for Hierarchical Models, December 2013.

D. M. Blei, A. Kucukelbir, and J. D. McAuliffe. Variational inference: A review for statisticians. *Journal of the American statistical Association*, 112(518):859–877, 2017.

C. S. Boeije and W. R. Rossen. Fitting foam simulation model parameters to data. In *IOR 2013-17th European Symposium on Improved Oil Recovery*, pages cp–342. European Association of Geoscientists & Engineers, 2013.

D. C. Bond and O. C. Holbrook. Gas drive oil recovery process. US Patent, No. 2866507, December 1956.

S. Borazjani, N. Hemmati, A. Behr, L. Genolet, H. Mahani, A. Zeinijahromi, and P. Bedrikovetsky. Simultaneous determination of gas–water relative permeability and capillary pressure from steady-state corefloods. *Journal of Hydrology*, 598:126355, July 2021. ISSN 00221694. doi: 10.1016/j.jhydrol.2021.126355.

G. E. P. Box and G. C. Tiao. *Bayesian inference in statistical analysis*, volume 40. John Wiley & Sons, 1992.

R. H. Brooks and A. T. Corey. *Hydraulic properties of porous media and their relationship to drainage design*. PhD thesis, Colorado State University. Libraries, 1963.

S. Brooks. Markov chain monte carlo method and its application. *Journal of the royal statistical society: series D (the Statistician)*, 47(1):69–100, 1998.

R. E. Caflisch. Monte carlo and quasi-monte carlo methods. *Acta numerica*, 7:1–49, 1998.

F. Campolongo, A. Saltelli, and J. Cariboni. From screening to quantitative sensitivity analysis. a unified approach. *Computer physics communications*, 182(4):978–988, 2011. doi: https://doi.org/10.1016/j.cpc.2010.12.039.

B. Carpenter, A. Gelman, M. D. Hoffman, D. Lee, B. Goodrich, M. Betancourt, M. A. Brubaker, J. Guo, P. Li, and A. Riddell. Stan: A Probabilistic Programming Language. *Journal of statistical software*, 76:1, 2017. ISSN 1548-7660. doi: 10.18637/jss.v076.i01.

A. Caticha and R. Preuss. Maximum Entropy and Bayesian Data Analysis: Entropic Priors. *Physical Review E*, 70(4):046127, October 2004. ISSN 1539-3755, 1550-2376. doi: 10.1103/PhysRevE.70.046127.

J. S. A. Cavalcante Filho, M. Delshad, and K. Sepehrnoori. Estimation of Foam–Flow Parameters for Local Equilibrium Methods by Use of Steady-State Flow Experiments

and Optimization Algorithms. *SPE Reservoir Evaluation & Engineering*, 21(01):160–173, October 2017. ISSN 1094-6470. doi: 10.2118/179597-PA.

J. B. Cedro and G. Chapiro. Traveling wave solutions for a realistic non-newtonian foam flow model. *Geoenergy Science and Engineering*, 232:212478, 2024.

J. B. Cedro, F. F. de Paula, and G. Chapiro. On the modeling of the foam dynamics in heterogeneous porous media. *Advances in Water Resources*, 196:104882, February 2025. ISSN 03091708. doi: 10.1016/j.advwatres.2024.104882.

M. Chabert, M. Morvan, and L. Nabzar. Advanced Screening Technologies for the Selection of Dense CO2 Foaming Surfactants. In *SPE Improved Oil Recovery Symposium*, pages SPE–154147. OnePetro, April 2012. doi: 10.2118/154147-MS.

S. H. Chang and R. Grigg. Foam Displacement Modeling in CO2 Flooding Processes. In *SPE/DOE Improved Oil Recovery Symposium*. OnePetro, April 1996. doi: 10.2118/35401-MS.

H. Chen, A. S. Elhag, Y. Chen, J. A. Noguera, A. M. AlSumaiti, G. J. Hirasaki, Q. P. Nguyen, S. L. Biswal, S. Yang, and K. P. Johnston. Oil effect on CO2 foam stabilized by a switchable amine surfactant at high temperature and high salinity. *Fuel*, 227:247–255, September 2018. ISSN 0016-2361. doi: 10.1016/j.fuel.2018.04.020.

Q. Chen, M. Gerritsen, and A. R. Kovscek. Modeling foam displacement with the local-equilibrium approximation: theory and experimental verification. *SPE Journal*, 15(01): 171–183, 2010.

Z. Chen, G. Huan, and Y. Ma. *Computational methods for multiphase flows in porous media*. SIAM, 2006.

L. Cheng, S. I. Kam, M. Delshad, and W. Rossen. Simulation of dynamic foam-acid diversion processes. In *SPE European Formation Damage Conference and Exhibition*, pages SPE–68916. SPE, 2001.

M. A. Christie and M. J. Blunt. Tenth SPE Comparative Solution Project: A Comparison of Upscaling Techniques. In *SPE Reservoir Simulation Symposium*. OnePetro, February 2001. doi: 10.2118/66599-MS.

Computer Modeling Group. CMG. Stars users manual; version 2019.10, 2019.

A. T. Corey. The interrelation between gas and oil relative permeabilities. *Producers monthly*, pages 38–41, 1954.

Katalin Csill'e, ry, Michael GB Blum, Oscar E Gaggiotti, and Olivier François. Approximate bayesian computation (abc) in practice. *Trends in ecology & evolution*, 25(7):410–418, 2010.

John H. Cushman and Daniel M. Tartakovsky, editors. *The Handbook of Groundwater Engineering*. CRC Press, Boca Raton, 3 edition, November 2016. ISBN 978-1-315-37180-1. doi: 10.1201/9781315371801.

C. Da, G. Jian, S. Alzobaidi, J. Yang, S. L. Biswal, G. J. Hirasaki, and K. P. Johnston. Design of CO2-in-Water Foam Stabilized with Switchable Amine Surfactants at High Temperature in High-Salinity Brine and Effect of Oil. *Energy & Fuels*, 32(12):12259–12267, December 2018. ISSN 0887-0624. doi: 10.1021/acs.energyfuels.8b02959.

T. Danelon, P. Paz, and G. Chapiro. The mathematical model and analysis of the nanoparticle-stabilized foam displacement. *Applied Mathematical Modelling*, 125:630–649, 2024.

C. Daniel. One-at-a-time plans. *Journal of the American Statistical Association*, 68(342): 353–360, 1973. doi: 10.1080/01621459.1973.10482433. URL `https://www.tandfonline.com/doi/abs/10.1080/01621459.1973.10482433`.

G. B. de Miranda, L. S. Ribeiro, J. M. da Fonseca Façanha, A. Pérez-Gramatges, B. M. Rocha, G. Chapiro, and R. W. Dos Santos. Characterization of Foam-Assisted Water-Gas Flow via Inverse Uncertainty Quantification Techniques. In *Computational Science – ICCS 2022*, pages 310–322, Cham, 2022a. Springer International Publishing. ISBN 978-3-031-08760-8. doi: 10.1007/978-3-031-08760-8_26.

G. B. de Miranda, L. S. Ribeiro, B. M. Rocha, J. M. D. F. Façanha, A. Pérez-Gramatges, R. W. Dos Santos, and G. Chapiro. An Improved Approach for Uncertainty Quantification Based on Steady-State Experimental Data in Foam-Assisted Enhanced Oil Recovery. In *ECMOR 2022*, volume 2022, pages 1–14. European Association of Geoscientists & Engineers, September 2022b. doi: 10.3997/2214-4609.202244048.

G. B. de Miranda, R. W. dos Santos, G. Chapiro, and B. M. Rocha. Uncertainty Quantification on Foam Modeling: The Interplay of Relative Permeability and Implicit-texture Foam Parameters. *Transport in Porous Media*, 152(1):8, December 2024. ISSN 1573-1634. doi: 10.1007/s11242-024-02137-1.

G. B. de Miranda, G. Chapiro, R. W. dos Santos, and B. M. Rocha. On the mobility reduction factor for the quantification of foam strength in porous media. *(Submitted))*, 2025a.

G. B. de Miranda, A. M. Ribeiro, R. W. dos Santos, G. Chapiro, and B. M. Rocha. Modeling foam flow in porous media influenced by oil: A computational framework for improved parameter estimation. *(Submitted))*, 2025b.

A. de Moura Ribeiro, L. F. Lopes, B. M. Rocha, R. Weber dos Santos, J. M. F. Façanha, A. Pérez-Gramatges, and G. Chapiro. Quantifying experimental impacts

on non-newtonian foam characterization for flow modeling in porous media: Insights from foam-quality and flow rate scan experiments. *Water Resources Research*, 61(9): e2024WR039536, 2025. ISSN 1944-7973. doi: 10.1029/2024WR039536.

F. F. de Paula, T. Quinelato, I. Igreja, and G. Chapiro. A Numerical Algorithm to Solve the Two-Phase Flow in Porous Media Including Foam Displacement. In *Computational Science extendash ICCS 2020*, Lecture Notes in Computer Science, pages 18–31, Cham, 2020. Springer International Publishing. ISBN 978-3-030-50436-6. doi: 10.1007/978-3-030-50436-6_2.

F. F. de Paula, I. Igreja, T. O. Quinelato, and G. Chapiro. Numerical simulation of foam displacement impacted by kinetic and equilibrium surfactant adsorption. *Advances in Water Resources*, 188:104690, June 2024. ISSN 0309-1708. doi: 10.1016/j.advwatres.2024.104690.

E. del Campo Estrada. *Ecoulements de mousse pour la d'epollution d'aquifères.* PhD thesis, Universit'e de Bordeaux, 2014.

M. Delshad, G. A. Pope, and K. Sepehrnoori. A compositional simulator for modeling surfactant enhanced aquifer remediation, 1 formulation. *Journal of Contaminant Hydrology*, 23(4):303–327, August 1996. ISSN 01697722. doi: 10.1016/0169-7722(95)00106-9.

Z. F. Dholkawala, H. Sarma, and S. Kam. Application of fractional flow theory to foams in porous media. *Journal of Petroleum Science and Engineering*, 57(1-2):152–165, 2007.

L. Ding, L. Cui, S. Jouenne, O. Gharbi, M. Pal, H. Bertin, M. A. Rahman, C. Romero, and Dominique Gu'e, rillot. Estimation of Local Equilibrium Model Parameters for Simulation of the Laboratory Foam-Enhanced Oil Recovery Process Using a Commercial Reservoir Simulator. *ACS Omega*, 5(36):23437–23449, September 2020a. ISSN 2470-1343, 2470-1343. doi: 10.1021/acsomega.0c03401.

L. Ding, Q. Wu, L. Zhang, and Dominique Gu'e, rillot. Application of Fractional Flow Theory for Analytical Modeling of Surfactant Flooding, Polymer Flooding, and Surfactant/Polymer Flooding for Chemical Enhanced Oil Recovery. *Water*, 12(8):2195, August 2020b. ISSN 2073-4441. doi: 10.3390/w12082195.

V. G. Eck, W. P. Donders, J. Sturdy, J. Feinberg, T. Delhaas, L. R. Hellevik, and W. Huberts. A guide to uncertainty quantification and sensitivity analysis for cardiovascular applications. *International journal for numerical methods in biomedical engineering*, 32 (8):e02755, 2016.

A. A. Eftekhari and R. Farajzadeh. Effect of foam on liquid phase mobility in porous media. *Scientific reports*, 7(1):1–8, 2017.

O. G. Ernst, A. Mugler, H. Starkloff, and E. Ullmann. On the convergence of generalized polynomial chaos expansions. *ESAIM: Mathematical Modelling and Numerical Analysis*, 46(2):317–339, 2012.

A. H. Falls, G. J. Hirasaki, T. W. Patzek, D. A. Gauglitz, D. D. Miller, and T. Ratulowski. Development of a Mechanistic Foam Simulator: The Population Balance and Generation by Snap-Off. *SPE Reservoir Engineering*, 3(03):884–892, August 1988. ISSN 0885-9248. doi: 10.2118/14961-PA.

R. Farajzadeh, A. Andrianov, R. Krastev, G. J. Hirasaki, and W. R. Rossen. Foam–oil interaction in porous media: Implications for foam assisted enhanced oil recovery. *Advances in Colloid and Interface Science*, 183–184:1–13, November 2012. ISSN 0001-8686. doi: 10.1016/j.cis.2012.07.002.

R. Farajzadeh, A. A. Eftekhari, H. Hajibeygi, J. M. van der Meer, S. Vincent-Bonnieu, and W. R. Rossen. Simulation of instabilities and fingering in surfactant alternating gas (sag) foam enhanced oil recovery. In *SPE Reservoir Simulation Conference?*, page D011S001R005. SPE, 2015a.

R. Farajzadeh, M. Lotfollahi, A. A. Eftekhari, W. R. Rossen, and G. J. Hirasaki. Effect of Permeability on Foam-model Parameters and the Limiting Capillary Pressure. In *IOR 2015 - 18th European Symposium on Improved Oil Recovery*, page cp. European Association of Geoscientists & Engineers, April 2015b. ISBN 978-94-6282-141-5. doi: 10.3997/2214-4609.201412134.

R. Farajzadeh, M. Lotfollahi, A. A. Eftekhari, W. R. Rossen, and G. J. H. Hirasaki. Effect of Permeability on Implicit-Texture Foam Model Parameters and the Limiting Capillary Pressure. *Energy & Fuels*, 29(5):3011–3018, May 2015c. ISSN 0887-0624. doi: 10.1021/acs.energyfuels.5b00248.

S. A. Faroughi, A. J. J. Pruvot, and J. McAndrew. The rheological behavior of energized fluids and foams with application to hydraulic fracturing: Review. *Journal of Petroleum Science and Engineering*, 163:243–263, April 2018. ISSN 0920-4105. doi: 10.1016/j.petrol.2017.12.051.

J. Feinberg and H. P. Langtangen. Chaospy: An open source tool for designing methods of uncertainty quantification. *Journal of Computational Science*, 11:46–57, 2015.

A. N. Fried. Foam-drive process for increasing the recovery of oil. Technical report, Bureau of Mines, San Francisco, Calif.(USA). San Francisco Petroleum Research Lab., 1960.

G. C. Fritis, P. S. Paz, L. F. Lozano, and G. Chapiro. On the riemann problem for the foam displacement in porous media with linear adsorption. *SIAM Journal on Applied Mathematics*, 84(2):581–601, 2024.

G. C. Fritis, P. S. Z. Paz, and G. Chapiro. Modeling the optimal foam injection slug in porous medium accounting adsorption effects. *International Journal of Non-Linear Mechanics*, 178:105199, November 2025. ISSN 0020-7462. doi: 10.1016/j.ijnonlinmec.2025.105199.

O. Gassara, F. Douarche, B. Braconnier, and B. Bourbiaux. Calibrating and interpreting implicit-texture models of foam flow through porous media of different permeabilities. *Journal of Petroleum Science and Engineering*, 159:588–602, November 2017. ISSN 0920-4105. doi: 10.1016/j.petrol.2017.09.069.

A. Gelman, J. B. Carlin, H. S. Stern, and D. B. Rubin. *Bayesian data analysis*. Chapman and Hall/CRC, 1995.

A. Gelman, J. B. Carlin, H. S. Stern, D. B. Dunson, A. Vehtari, and D. B. Rubin. *Bayesian Data Analysis*. CRC Press, third edition edition, February 2021.

C. J. Geyer. Practical Markov Chain Monte Carlo. *Statistical Science*, 7(4):473–483, November 1992. ISSN 0883-4237, 2168-8745. doi: 10.1214/ss/1177011137.

R. G. Ghanem and P. D. Spanos. Stochastic finite element method: Response statistics. In *Stochastic finite elements: a spectral approach*, pages 101–119. Springer, 1991.

R. B. Gramacy. *Surrogates: Gaussian process modeling, design, and optimization for the applied sciences*. Chapman and Hall/CRC, 2020.

D. M. Hamby. A review of techniques for parameter sensitivity analysis of environmental models. *Environmental monitoring and assessment*, 32:135–154, 1994. doi: 10.1007/BF00547132.

R. D. G. F. Harshini, Ranjith P.g, W. G. P. Kumari, and D. C. Zhang. Innovative applications of carbon dioxide foam in geothermal energy recovery: Challenges and perspectives - A review. *Geoenergy Science and Engineering*, 241:213091, October 2024. ISSN 2949-8910. doi: 10.1016/j.geoen.2024.213091.

W. K. Hastings. Monte carlo sampling methods using markov chains and their applications. *Biometrika*, 57(1):97–109, 1970. ISSN 0006-3444. doi: 10.1093/biomet/57.1.97. URL `https://doi.org/10.1093/biomet/57.1.97`.

H. Hematpur, S. M. Mahmood, N. H. Nasr, and K. A. Elraies. Foam flow in porous media: Concepts, models and challenges. *Journal of Natural Gas Science and Engineering*, 53:163–180, 2018. ISSN 1875-5100. doi: https://doi.org/10.1016/j.jngse.2018.02.017. URL `https://www.sciencedirect.com/science/article/pii/S1875510018300878`.

H. Hematpur, S. Hosseini, S. M. Mahmood, R. Abdollahi, Z. Hamdi, and R. Ghamarpoor. A new approach to foam flooding modelling with novel parameter Estimation techniques.

Scientific Reports, 15(1):22829, July 2025. ISSN 2045-2322. doi: 10.1038/s41598-025-05847-8.

N. Hemmati, S. Borazjani, A. Badalyan, L. Genolet, A. Behr, A. Zeinijahromi, and P. Bedrikovetsky. Determining relative permeability and capillary pressure from mixed-wet core floods. *Geoenergy Science and Engineering*, 239:212885, August 2024. ISSN 2949-8910. doi: 10.1016/j.geoen.2024.212885.

G. J. Hirasaki. The Steam-Foam Process. *Journal of Petroleum Technology*, 41(05): 449–456, May 1989. ISSN 0149-2136. doi: 10.2118/19505-PA.

M. D. Hoffman and A. Gelman. The No-U-Turn Sampler: Adaptively Setting Path Lengths in Hamiltonian Monte Carlo, November 2011.

M. D. Hoffman and A. Gelman. The No-U-Turn sampler: adaptively setting path lengths in Hamiltonian Monte Carlo. *J. Mach. Learn. Res.*, 15(1):1593–1623, 2014.

P. Horgue, C. Soulaine, J. Franc, R. Guibert, and G. Debenest. An open-source toolbox for multiphase flow in porous media. *Computer Physics Communications*, 187:217–226, 2015.

A. A. A. Hussain, S. Vincent-Bonnieu, R. Z. Kamarul Bahrim, R. M. Pilus, and W. R. Rossen. Impact of Different Oil Mixtures on Foam in Porous Media and in Bulk. *Industrial & Engineering Chemistry Research*, 58(28):12766–12772, July 2019. ISSN 0888-5885. doi: 10.1021/acs.iecr.9b01589.

R. L. Iman and W. J. Conover. A distribution-free approach to inducing rank correlation among input variables. *Communications in Statistics - Simulation and Computation*, 11 (3):311–334, January 1982. ISSN 0361-0918. doi: 10.1080/03610918208812265.

B. Iooss and P. Lemaître. A review on global sensitivity analysis methods. *Uncertainty management in simulation-optimization of complex systems: algorithms and applications*, pages 101–122, 2015.

H. Jasak. OpenFOAM: Open source CFD in research and industry. *International journal of naval architecture and ocean engineering*, 1(2):89–94, 2009.

E. T. Jaynes. *Probability theory: The logic of science*. Cambridge university press, 2003.

H. Jia, H. Yu, T. Wang, P. Song, J. Song, and Y. Wang. Investigation of non-chemical CO2 microbubbles for enhanced oil recovery and carbon sequestration in heterogeneous porous media. *Geoenergy Science and Engineering*, 242:213229, November 2024. ISSN 29498910. doi: 10.1016/j.geoen.2024.213229.

G. Jian, L. Zhang, C. Da, M. Puerto, K. P. Johnston, S. L. Biswal, and G. J. Hirasaki. Evaluating the Transport Behavior of CO2 Foam in the Presence of Crude Oil under High-Temperature and High-Salinity Conditions for Carbonate Reservoirs. *Energy & Fuels*, 33(7):6038–6047, July 2019. ISSN 0887-0624. doi: 10.1021/acs.energyfuels.9b00667.

S. A. Jones, G. Laskaris, S. Vincent-Bonnieu, R. Farajzadeh, and W. R. Rossen. Effect of surfactant concentration on foam: From coreflood experiments to implicit-texture foam-model parameters. *Journal of Industrial and Engineering Chemistry*, 37:268–276, May 2016. ISSN 1226-086X. doi: 10.1016/j.jiec.2016.03.041.

S. Kahrobaei and R. Farajzadeh. Insights into Effects of Surfactant Concentration on Foam Behavior in Porous Media. *Energy & Fuels*, 33(2):822–829, February 2019. ISSN 0887-0624. doi: 10.1021/acs.energyfuels.8b03576.

S. I. Kam. Improved mechanistic foam simulation with foam catastrophe theory. *Colloids and Surfaces A: Physicochemical and Engineering Aspects*, 318(1-3):62–77, 2008.

L. Kapetas, S. Vincent-Bonnieu, S. Danelis, W. R. Rossen, R. Farajzadeh, A. A. Eftekhari, S. R. Shafian, and R. Z. Bahrim. Effect of temperature on foam flow in porous media. In *SPE Middle East Oil & Gas Show and Conference*. OnePetro, 2015.

T. Kim, W. S. Han, J. Piao, P. K. Kang, and J. Shin. Predicting remediation efficiency of LNAPLs using surrogate polynomial chaos expansion model and global sensitivity analysis. *Advances in Water Resources*, 163:104179, May 2022. ISSN 0309-1708. doi: 10.1016/j.advwatres.2022.104179.

A. R. Kovscek and C. J. Radke. Fundamentals of Foam Transport in Porous Media. In *Foams: Fundamentals and Applications in the Petroleum Industry*, volume 242 of *Advances in Chemistry*, chapter 3, pages 115–163. American Chemical Society, October 1994. ISBN 978-0-8412-2719-4. doi: 10.1021/ba-1994-0242.ch003.

A. R. Kovscek, T. W. Patzek, and C. J. Radke. A mechanistic population balance model for transient and steady-state foam flow in boise sandstone. *Chemical Engineering Science*, 50(23):3783–3799, 1995.

A. R. Kovscek, T. W. Patzek, and Clayton J. Radke. Mechanistic Foam Flow Simulation in Heterogeneous and Multidimensional Porous Media. *SPE Journal*, 2(04):511–526, December 1997. ISSN 1086-055X. doi: 10.2118/39102-PA.

L. W. Lake. Enhanced oil recovery. *Office of Scientific and Technical Information. U.S. Department of Energy*, 1 1989.

R. G. Larson. Analysis of the Physical Mechanisms in Surfactant Flooding. *Society of Petroleum Engineers Journal*, 18(01):42–58, February 1978. ISSN 0197-7520. doi: 10.2118/6003-PA.

J. Lee, W. Sung, and J. Choi. Metamodel for efficient estimation of capacity-fade uncertainty in li-ion batteries for electric vehicles. *Energies*, 8(6):5538–5554, 2015.

M. Leutbecher and T. N. Palmer. Ensemble forecasting. *Journal of Computational Physics*, 227(7):3515–3539, March 2008. ISSN 0021-9991. doi: 10.1016/j.jcp.2007.02.014.

R. F. Li, W. Yan, S. Liu, G. J. Hirasaki, and C. A. Miller. Foam mobility control for surfactant enhanced oil recovery. *SPE Journal*, 15(04):928–942, 2010.

F. Lomeland, E. Ebeltoft, and W. H. Thomas. A new versatile relative permeability correlation. In *International symposium of the society of core analysts, Toronto, Canada*, volume 112, 2005.

M. Lotfollahi, R. Farajzadeh, M. Delshad, A. Varavei, and W. R. Rossen. Comparison of implicit-texture and population-balance foam models. *Journal of Natural Gas Science and Engineering*, 31:184–197, April 2016. ISSN 18755100. doi: 10.1016/j.jngse.2016.03.018.

L. F. Lozano, R. Q. Zavala, and G. Chapiro. Mathematical properties of the foam flow in porous media. *Computational Geosciences*, 25:515–527, 2021.

S. M. Lundberg and S. Lee. A unified approach to interpreting model predictions. In I. Guyon, U. V. Luxburg, S. Bengio, H. Wallach, R. Fergus, S. Vishwanathan, and R. Garnett, editors, *Advances in Neural Information Processing Systems 30*, pages 4765–4774. Curran Associates, Inc., 2017. URL `http://papers.nips.cc/paper/7062-a-unified-approach-to-interpreting-model-predictions.pdf`.

N. Luthen, S. Marelli, and B. Sudret. Sparse polynomial chaos expansions: Literature survey and benchmark. *SIAM/ASA Journal on Uncertainty Quantification*, 9(2):593–649, 2021.

X. Lyu, D. Voskov, and W. R. Rossen. Numerical investigations of foam-assisted co2 storage in saline aquifers. *International journal of greenhouse gas control*, 108:103314, 2021a.

X. Lyu, D. Voskov, J. Tang, and W. R. Rossen. Simulation of Foam Enhanced-Oil-Recovery Processes Using Operator-Based Linearization Approach. *SPE Journal*, 26 (04):2287–2304, August 2021b. ISSN 1086-055X. doi: 10.2118/205399-PA.

K. Ma, R. Farajzadeh, Jose L. Lopez-Salinas, , Clarence A. Miller, Sibani Lisa Biswal, and George J. Hirasaki. Estimation of Parameters for the Simulation of Foam Flow through Porous Media: Part 3; Non-Uniqueness, Numerical Artifact and Sensitivity. In *All Days*, pages SPE–165263–MS, Kuala Lumpur, Malaysia, July 2013. SPE. doi: 10.2118/165263-MS.

K. Ma, R. Farajzadeh, J. L. Lopez-Salinas, C. A. Miller, S. L. Biswal, and G. J. Hirasaki. Non-uniqueness, numerical artifacts, and parameter sensitivity in simulating steady-state and transient foam flow through porous media. *Transport in porous media*, 102(3): 325–348, 2014a.

K. Ma, G. Ren, K. Mateen, D. Morel, and P. Cordelier. Literature Review of Modeling Techniques for Foam Flow through Porous Media. In *SPE Improved Oil Recovery Symposium*. OnePetro, April 2014b. doi: 10.2118/169104-MS.

K. Ma, G. Ren, K. Mateen, D. Morel, and P. Cordelier. Modeling Techniques for Foam Flow in Porous Media. *SPE Journal*, 20(03):453–470, February 2015. ISSN 1086-055X. doi: 10.2118/169104-PA.

K. Ma, K. Mateen, G. Ren, H. Luo, G. Bourdarot, and D. Morel. Mechanistic modeling of foam flow through porous media in the presence of oil: Review of foam-oil interactions and an improved bubble population-balance model. In *SPE Annual Technical Conference and Exhibition*. OnePetro, September 2018. doi: 10.2118/191564-MS.

S. Marelli and B. Sudret. Uqlab user manual–polynomial chaos expansions. *Chair of risk, safety & uncertainty quantification, ETH Z"urich, 0.9-104 edition*, pages 97–110, 2015.

O. Martin and T. Wiecki. *Bayesian analysis with Python: introduction to statistical modeling and probabilistic programming using PyMC3 and ArviZ*. Packt Publishing Limited, second edition edition, 2018. ISBN 978-1-78934-165-2.

O. A. Martin, R. Kumar, and J. Lao. *Bayesian Modeling and Computation in Python*. CRC Press, Boca Raton, 2021. ISBN 978-0-367-89436-8.

R. McElreath. *Statistical rethinking: A Bayesian course with examples in R and Stan*. Chapman and Hall/CRC, England, 2020.

M. Mehrabi, K. Sepehrnoori, and M. Delshad. Displacement Theory of Low-Tension Gas Flooding. *Transport in Porous Media*, 142(3):475–491, April 2022. ISSN 1573-1634. doi: 10.1007/s11242-022-01753-z.

N. Metropolis and S. Ulam. The Monte Carlo method. *Journal of the American statistical association*, 44(247):335–341, 1949.

N. Metropolis, A. W. Rosenbluth, M. N. Rosenbluth, A. H. Teller, and E. Teller. Equation of state calculations by fast computing machines. *The Journal of Chemical Physics*, 21(6):1087–1092, 1953. ISSN 0021-9606. doi: 10.1063/1.1699114. URL `https://aip.scitation.org/doi/10.1063/1.1699114`. Publisher: American Institute of Physics.

B. Metz, O. Davidson, H. De Coninck, M. Loos, and L. Meyer. *IPCC special report on carbon dioxide capture and storage*. Cambridge: Cambridge University Press, 2005.

S. Mohammadi, J. Collins, and D. A. Coombe. Field Application and Simulation of Foam for Gas Diversion. In *IOR 1995 - 8th European Symposium on Improved Oil Recovery*, page cp. European Association of Geoscientists & Engineers, May 1995. ISBN 978-94-6282-125-5. doi: 10.3997/2214-4609.201406964.

A. Moradi-Araghi, E. L. Johnston, D. R. Zornes, and K. J. Harpole. Laboratory Evaluation of Surfactants for CO2-Foam Applications at the South Cowden Unit. In *International Symposium on Oilfield Chemistry*, pages SPE–37218. OnePetro, February 1997. doi: 10.2118/37218-MS.

T. J. Myers and C. J. Radke. Transient Foam Displacement in the Presence of Residual Oil: Experiment and Simulation Using a Population-Balance Model. *Industrial & Engineering Chemistry Research*, 39(8):2725–2741, August 2000. ISSN 0888-5885. doi: 10.1021/ie990909u.

M. Namdar-Zanganeh, S. I. Kam, T. C. LaForce, and W. R. Rossen. The Method of Characteristics Applied to Oil Displacement by Foam. *SPE Journal*, 16(01):8–23, August 2010. ISSN 1086-055X. doi: 10.2118/121580-PA.

T. Neumann, K. H. Knuth, A. Caticha, J. L. Center, A. Giffin, and Carlos C. Rodr'i, guez. Bayesian Inference Featuring Entropic Priors. In *AIP Conference Proceedings*, volume 954, pages 283–292. AIP, 2007. doi: 10.1063/1.2821274.

M. J. Oak, L.E. Baker, and D.C. Thomas. Three-Phase Relative Permeability of Berea Sandstone. *Journal of Petroleum Technology*, 42(08):1054–1061, August 1990. ISSN 0149-2136, 1944-978X. doi: 10.2118/17370-PA.

C. J. Okere, L. Zheng, G. Su, H. Liu, Q. Chang, and O. J. Obiafudo. Critical analysis of productivity of well 2l after foam-acid diversion. In *International Conference on Mechanical Engineering and Applied Composite Materials*, pages 21–36. Springer, 2020.

A. Orujov, K. Coddington, and S. A. Aryana. A review of ccus in the context of foams, regulatory frameworks and monitoring. *Energies*, 16(7):3284, 2023.

W. T. Osterloh and M. J. Jante. Effects of Gas and Liquid Velocity on Steady-State Foam Flow at High Temperature. In *SPE/DOE Enhanced Oil Recovery Symposium*, pages SPE–24179. OnePetro, April 1992. doi: 10.2118/24179-MS.

T. W. Patzek. Description of Foam Flow in Porous Media by the Population Balance Method. In *Surfactant-Based Mobility Control*, volume 373 of *ACS Symposium Series*, chapter 16, pages 326–341. American Chemical Society, July 1988. ISBN 978-0-8412-1491-0. doi: 10.1021/bk-1988-0373.ch016.

T. W. Patzek. Field applications of steam foam for mobility improvement and profile control. *SPE Reservoir Engineering*, 11(02):79–86, 1996.

T. W. Patzek and N. A. Myhill. Simulation of the Bishop Steam Foam Pilot. In *SPE California Regional Meeting*. OnePetro, April 1989. doi: 10.2118/18786-MS.

F. F. Paula, I. Igreja, T. Quinelato, and G. Chapiro. A numerical investigation into the influence of the surfactant injection technique on the foam flow in heterogeneous porous media. *Advances in Water Resources*, 171:104358, January 2022. ISSN 0309-1708. doi: 10.1016/j.advwatres.2022.104358.

L. G. Pedroni. *Experimental study of mobility control by foams: potential of a FAWAG process in pre-salt reservoir conditions*. PhD thesis, Université Pierre et Marie Curie-Paris VI, 2017.

G. A. Pope. The Application of Fractional Flow Theory to Enhanced Oil Recovery. *Society of Petroleum Engineers Journal*, 20(03):191–205, June 1980. ISSN 0197-7520. doi: 10.2118/7660-PA.

G. A. Pope and R. C. Nelson. A Chemical Flooding Compositional Simulator. *Society of Petroleum Engineers Journal*, 18(05):339–354, October 1978. ISSN 0197-7520. doi: 10.2118/6725-PA.

K. V. Price. Differential Evolution. In Ivan Zelinka, V. Snasael, and A. Abraham, editors, *Handbook of Optimization: From Classical to Modern Approach*, pages 187–214. Springer, Berlin, Heidelberg, 2013. ISBN 978-3-642-30504-7. doi: 10.1007/978-3-642-30504-7_8.

V. V. Ranade. Multiphase flow processes. In *Computational Flow Modeling for Chemical Reactor Engineering*, volume 5 of *Process Systems Engineering*, pages 85–122. Academic Press, 2002. doi: https://doi.org/10.1016/S1874-5970(02)80005-4. URL `https://www.sciencedirect.com/science/article/pii/S1874597002800054`.

A. Raue, C. Kreutz, T. Maiwald, J. Bachmann, M. Schilling, U. Klingmüller, and J. Timmer. Structural and practical identifiability analysis of partially observed dynamical models by exploiting the profile likelihood. *Bioinformatics*, 25(15):1923–1929, August 2009. ISSN 1367-4803. doi: 10.1093/bioinformatics/btp358.

L. S. Ribeiro, G. B. Miranda, B. M. Rocha, G. Chapiro, and R. Weber dos Santos. On the Identifiability of Relative Permeability and Foam Displacement Parameters in Porous Media Flow. *Water Resources Research*, 60(3):e2023WR036751, 2024. ISSN 1944-7973. doi: 10.1029/2023WR036751.

A. U. Rognmo, S. B. Fredriksen, Z. P. Alcorn, M. Sharma, Tore Fø, yen, Øyvind Eide, Arne Graue, and Martin Fernø. Pore-to-Core EOR Upscaling for CO2 Foam for CCUS. *SPE Journal*, 24(06):2793–2803, July 2019. ISSN 1086-055X. doi: 10.2118/190869-PA.

A. Rosman and S. I. Kam. Modeling Foam-diversion Process Using Three-phase Fractional Flow Analysis in a Layered System. *Energy Sources, Part A: Recovery, Utilization, and Environmental Effects*, 31(11):936–955, June 2009. ISSN 1556-7036. doi: 10.1080/15567030701752875.

W. R. Rossen. Foams in Enhanced Oil Recovery. In *Foams*. Routledge, 1996. ISBN 978-0-203-75570-9. doi: 10.1002/food.19970410116.

W. R. Rossen, S. C. Zeilinger, Jianxin Shi, and M. T. Lim. Mechanistic Simulation of Foam Processes in Porous Media. In *SPE Annual Technical Conference and Exhibition*. OnePetro, September 1994. doi: 10.2118/28940-MS.

W. R. Rossen, S. C. Zeilinger, J. X. Shi, and M. T. Lim. Simplified mechanistic simulation of foam processes in porous media. *SPE Journal*, 4(03):279–287, 1999.

W. R. Rossen, R. Farajzadeh, G. J. Hirasaki, and M. Amirmoshiri. Potential and challenges of foam-assisted CO2 sequestration. *Geoenergy Science and Engineering*, 239:212929, August 2024. ISSN 2949-8910. doi: 10.1016/j.geoen.2024.212929.

A. Sæle, A. Graue, and Z. P. Alcorn. Unsteady-state CO2 foam injection for increasing enhanced oil recovery and carbon storage potential. *Advances in Geo-Energy Research*, 6(6):472–481, December 2022. ISSN 2208-598X. doi: 10.46690/ager.2022.06.04.

A. Saltelli. Making best use of model evaluations to compute sensitivity indices. *Computer physics communications*, 145(2):280–297, 2002. doi: https://doi.org/10.1016/S0010-4655(02)00280-1.

A. Saltelli, M. Ratto, T. Andres, F. Campolongo, J. Cariboni, D. Gatelli, M. Saisana, and S. Tarantola. *Global sensitivity analysis: the primer*. John Wiley & Sons, England, 2008.

J. Salvatier, T. V. Wiecki, and C. Fonnesbeck. Probabilistic programming in python using PyMC3. *PeerJ Computer Science*, 2:e55, apr 2016. doi: 10.7717/peerj-cs.55. URL `https://doi.org/10.7717/peerj-cs.55`.

Schlumberger. *ECLIPSE Technical Description 2014.2*. Schlumberger, 2014. ECLIPSE Reservoir Simulation Software Reference Manual.

M. Shafiei, Y. Kazemzadeh, M. Escrochi, F. B. Cortés, C. A. Franco, and M. Riazi. A comprehensive review direct methods to overcome the limitations of gas injection during the EOR process. *Scientific Reports*, 14(1):7468, March 2024. ISSN 2045-2322. doi: 10.1038/s41598-024-58217-1.

M. Sharma, Z. P. Alcorn, S. B. Fredriksen, A. U. Rognmo, M. A. Fernø, S. M. Skjæveland, and A. Graue. Model calibration for forecasting CO2-foam enhanced oil recovery

field pilot performance in a carbonate reservoir. *Petroleum Geoscience*, 26(1):141–149, February 2020. ISSN 1354-0793. doi: 10.1144/petgeo2019-093.

M. J. Shojaei, D. Or, and N. Shokri. Localized delivery of liquid fertilizer in coarse-textured soils using foam as carrier. *Transport in Porous Media*, 143(3):787–795, 2022.

M. Simjoo, Y. Dong, A. Andrianov, M. Talanana, and P.L.J. Zitha. Novel Insight Into Foam Mobility Control. *SPE Journal*, 18(03):416–427, June 2013. ISSN 1086-055X, 1930-0220. doi: 10.2118/163092-PA.

R. C. Smith. *Uncertainty quantification: theory, implementation, and applications*. SIAM, 2013.

I. M. Sobol'. On sensitivity estimation for nonlinear mathematical models. *Matematicheskoe modelirovanie*, 2(1):112–118, 1990.

I. M. Sobol. Global sensitivity indices for nonlinear mathematical models and their Monte Carlo estimates. *Mathematics and computers in simulation*, 55(1-3):271–280, 2001.

P. Sochala and OP Maî, L. tre. Polynomial chaos expansion for subsurface flows with uncertain soil parameters. *Advances in water resources*, 62:139–154, 2013.

C. Soize. *Uncertainty quantification: An Accelerated Course with Advanced Applications in Computational Engineering*. Springer, Switzerland, 2017.

P. Spirov and S. Rudyk. Testing of Snorre Field Foam Assisted Water Alternating Gas (FAWAG) Performance in New Foam Screening Model. *Oil & Gas Science and Technology - Revue d'IFP Energies nouvelles*, 70(6):1025–1033, November 2015. doi: 10.2516/ogst/2013193.

A. Sri Hanamertani, S. Saraji, and M. Piri. The effects of *in-situ* emulsion formation and superficial velocity on foam performance in high-permeability porous media. *Fuel*, 306: 121575, December 2021. ISSN 0016-2361. doi: 10.1016/j.fuel.2021.121575.

R. Storn and K. Price. Differential Evolution – A Simple and Efficient Heuristic for global Optimization over Continuous Spaces. *Journal of Global Optimization*, 11(4):341–359, December 1997. ISSN 1573-2916. doi: 10.1023/A:1008202821328.

B. Sudret. Global sensitivity analysis using polynomial chaos expansions. *Reliability engineering & system safety*, 93(7):964–979, 2008.

Q. Sun, Z. Li, J. Wang, S. Li, L. Jiang, and C. Zhang. Properties of multi-phase foam and its flow behavior in porous media. *RSC Advances*, 5(83):67676–67689, August 2015. ISSN 2046-2069. doi: 10.1039/C5RA09686C.

S. H. Talebian, R. Masoudi, I. M. Tan, and P. L. J. Zitha. Foam assisted CO2-EOR: A review of concept, challenges, and future prospects. *Journal of Petroleum Science and Engineering*, 120:202–215, August 2014. ISSN 0920-4105. doi: 10.1016/j.petrol.2014.05.013.

J. Tang, M. Ansari, and W. Rossen. Modelling the Effect of Oil on Foam for EOR. In *ECMOR XV-15th European Conference on the Mathematics of Oil Recovery*, pages cp–494. European Association of Geoscientists & Engineers, August 2016. doi: 10.3997/2214-4609.201601877.

J Tang, M. N. Ansari, and W. R. Rossen. Quantitative Modeling of the Effect of Oil on Foam for Enhanced Oil Recovery. *SPE Journal*, 24(03):1057–1075, 2019a.

J. Tang, P. Castañeda, D. Marchesin, and W. R. Rossen. Three-Phase Fractional-Flow Theory of Foam-Oil Displacement in Porous Media With Multiple Steady States. *Water Resources Research*, 55(12):10319–10339, 2019b. ISSN 1944-7973. doi: 10.1029/2019WR025264.

J. Tang, Sebastien Vincent-Bonnieu, , and William R. Rossen. Experimental Investigation of the Effect of Oil on Steady-State Foam Flow in Porous Media. *SPE Journal*, 24(01):140–157, February 2019c. ISSN 1086-055X. doi: 10.2118/194015-PA.

J. Tang, S. Vincent-Bonnieu, and W. R. Rossen. CT coreflood study of foam flow for enhanced oil recovery: The effect of oil type and saturation. *Energy*, 188:116022, December 2019d. ISSN 0360-5442. doi: 10.1016/j.energy.2019.116022.

J. Tang, P. Castaneda, D. Marchesin, and W. R. Rossen. Foam-Oil Displacements in Porous Media: Insights from Three-Phase Fractional-Flow Theory. In *Day 4 Thu, November 03, 2022*, page D042S195R003, Abu Dhabi, UAE, October 2022. SPE. doi: 10.2118/211467-MS.

D. M. Tartakovsky. Probabilistic risk analysis in subsurface hydrology. *Geophysical Research Letters*, 34(5), 2007. ISSN 1944-8007. doi: 10.1029/2007GL029245.

R. Tripathi, Z. P. Alcorn, A. Graue, and S. D. Kulkarni. Combination of non-ionic and cationic surfactants in generating stable CO2 foam for enhanced oil recovery and carbon storage. *Advances in Geo-Energy Research*, 13(1):42–55, June 2024. ISSN 2208-598X. doi: 10.46690/ager.2024.07.06.

A. R. Valdez, B. M. Rocha, G. Chapiro, and R. W. dos Santos. Uncertainty quantification and sensitivity analysis for relative permeability models of two-phase flow in porous media. *Journal of Petroleum Science and Engineering*, 192:107297, 2020. doi: 10.1016/j.petrol.2020.107297.

A. R. Valdez, B. M. Rocha, Juliana Maria Façanha, Alexandre Vilela Oliveira de Souza, Aurora Perez-Gramatges, Grigori Chapiro, and Rodrigo Weber dos Santos. Foam-assisted water–gas flow parameters: From core-flood experiment to uncertainty quantification and sensitivity analysis. *Transport in Porous Media*, pages 1–21, 2021. doi: 10.1007/s11242-021-01550-0.

A. R. Valdez, B. M. Rocha, G. Chapiro, and R. W. dos Santos. Assessing uncertainties and identifiability of foam displacement models employing different objective functions for parameter estimation. *Journal of Petroleum Science and Engineering*, page 110551, 2022. doi: 10.1016/j.petrol.2022.110551.

A. J. Castrillón Vásquez, L. F. Lozano, W. S. Pereira, J. B. Cedro, and G. Chapiro. The traveling wavefront for foam flow in two-layer porous media. *Computational Geosciences*, 26(6):1549–1561, December 2022. ISSN 1573-1499. doi: 10.1007/s10596-022-10169-z.

A. Vicard, O. Atteia, H. Bertin, and J. Lachaud. Estimation of Local Equilibrium Foam Model Parameters as Functions of the Foam Quality and the Total Superficial Velocity. *ACS Omega*, 7(20):16866–16876, May 2022. doi: 10.1021/acsomega.1c04899.

R. A. M. Vieira, S. S. F. Dos Santos, L. P. T. Do Nascimento, D. M. P. T. De Souza, and C. N. Da Silva. Experimental Characterization to Support a FAWAG Project in an Offshore Pre-Salt Field. In *Day 2 Tue, April 23, 2024*, page D021S005R005, Tulsa, Oklahoma, USA, April 2024. SPE. doi: 10.2118/218195-MS.

T. Wagener and F. Pianosi. What has global sensitivity analysis ever done for us? a systematic review to support scientific advancement and to inform policy-making in earth system modelling. *Earth-science reviews*, 194:1–18, 2019.

Z. Wang, S. Li, Z. Xu, S. A. Aryana, and J. Cai. Advances and challenges in foam stability: Applications, mechanisms, and future directions. *Capillarity*, 15(3):58–73, May 2025. ISSN 2652-3310. doi: 10.46690/capi.2025.06.02.

H. J. Welge. A Simplified Method for Computing Oil Recovery by Gas or Water Drive. *Journal of Petroleum Technology*, 4(04):91–98, April 1952. ISSN 0149-2136. doi: 10.2118/124-G.

N. Wiener. The homogeneous chaos. *American Journal of Mathematics*, 60(4):897–936, 1938.

D. Xiu. *Numerical methods for stochastic computations: a spectral method approach*. Princeton university press, 2010.

D. Xiu and J. S. Hesthaven. High-order collocation methods for differential equations with random inputs. *SIAM Journal on Scientific Computing*, 27(3):1118–1139, 2005.

D. Xiu and G. E. Karniadakis. The wiener–askey polynomial chaos for stochastic differential equations. *SIAM journal on scientific computing*, 24(2):619–644, 2002.

R. Q. Zavala, L. F. Lozano, P. L. Zitha, and G. Chapiro. Analytical solution for the population-balance model describing foam displacement. *Transport in Porous Media*, pages 1–17, 2021.

R. Q. Zavala, L. F. Lozano, and G. Chapiro. Traveling wave solutions describing the foam flow in porous media for low surfactant concentration. *Computational Geosciences*, 28 (2):323–340, 2024.

Y. Zeng, A. Muthuswamy, K. Ma, L. Wang, R. Farajzadeh, M. Puerto, S. Vincent-Bonnieu, A. Eftekhari, Y. Wang, C. Da, et al. Insights on foam transport from a texture-implicit local-equilibrium model with an improved parameter estimation algorithm. *Industrial & Engineering Chemistry Research*, 55(28):7819–7829, 2016.

Z. F. Zhang, Vicky L. Freedman, and Lirong Zhong. Foam Transport in Porous Media - A Review. Technical Report PNNL-18918, Pacific Northwest National Lab. (PNNL), Richland, WA (United States), November 2009.

J. Zhao, Y. He, and J. Yang. Experimental and population balance model interpretation of foam physics in porous media. *Frontiers in Physics*, 10, September 2022. ISSN 2296-424X. doi: 10.3389/fphy.2022.1028414.

K. Zhou, S. Li, X. Zhou, Y. Hu, C. Zhang, and J. Liu. Data-driven prediction and analysis method for nanoparticle transport behavior in porous media. *Measurement*, 172:108869, 2021. doi: 10.1016/j.measurement.2020.108869.

Z. Zhou and W. R. Rossen. Applying fractional-flow theory to foam processes at the limiting capillary pressure. *SPE Advanced Technology Series*, 3(01):154–162, 1995.

Y. Zhu. Ensemble forecast: A new approach to uncertainty and predictability. *Advances in Atmospheric Sciences*, 22(6):781–788, November 2005. ISSN 1861-9533. doi: 10.1007/BF02918678.

P. L. J. Zitha and D. X. Du. A new stochastic bubble population model for foam flow in porous media. *Transport in Porous Media*, 83(3):603–621, 2010.

APPENDIX A – Supplementary Information for Chapter 3

A.1 Comparison of the Prior Selection by Bayesian Diagnostics

In Bayesian statistics, some practitioners support that if there is no prior knowledge of how an event can occur, the event will be equally likely in any way. This is known as the Principle of Insufficient Reason (PIR), enunciated by Jakob Bernoulli Jaynes (2003). A noninformative prior is defined as a prior that provides little information about the studied variable (Box and Tiao, 1992). Gelman et al. (1995) advocates that there is no truly noninformative proper prior, in the sense that any prior includes some information. In order to assess the quality of the proposed strategy against diagnostic tools and investigate the nature of informative choices for priors, a truly uninformative prior is included in the experiments by an improper prior. Improper priors do not follow the traditional rules of probability distributions. They are often used in Bayesian statistics when the prior information available is truly minimal or when it's desirable to let the data dominate the posterior distribution entirely. Improper priors don't integrate to a finite value over their entire support, which means they lack a well-defined probability density function. It indicates no specific beliefs are introduced, allowing the data likelihood to drive the posterior distribution.

Three setups of priors are defined varying the distributions of foam parameters $fmmob$ and $sfbet$: (1) Flat strategy: uninformed priors defined by the half-flat, restricting only to positive real numbers; (2) Uniform strategy: the choices made by Valdez et al. (2021, 2022); (3) Entropic prior: the one proposed in this work using the principle of maximum entropy. Table 14 presents the three different setups. The other randomized parameters follow the same distribution as presented in Table 3 of the manuscript. It is important to notice that a fair mimicking of Valdez's strategy on a synthetic dataset is easy to define, as the boundaries are known. Table 15 summarizes the advantages of each strategy.

Table 14 – Setup of parameters for the different strategies.

Parameter	**Real**	**Flat**	**Uniform**	**Entropic**
$fmmob$	4341	$U(0,\infty)$	$U(10,10^6)$	$Exp\left(\overline{fmmob}^{-1}\right)$
$sfbet$	424	$U(0,\infty)$	$U(1,10^5)$	$Exp\left(\overline{sfbet}^{-1}\right)$

Table 15 – Advantages of each setup of priors.

Criteria/Pros	**Flat Prior**	**Uniform Prior**	**Entropic Prior**
Computational Feasibility		✓	✓
Uninformative / Bias-Free	✓		
Objectivity			✓

The strategies are evaluated in terms of different diagnostic tools in the following subsections.

A.1.1 Gelman-Rubin Statistic

Diagnostics in Bayesian inference involve assessing the convergence and quality of the inferred posterior distribution. A commonly employed method of evaluating convergence is analyzing the concurrence among the autonomous chains, which can be graphically assessed by plotting each chain trace. The Gelman-Rubin statistic (R-hat or $\hat{R}$) is a diagnostic tool that quantifies the ratio of the average variance of within-chain samples to the variance of pooled between-chain samples. Mathematically, it can be represented as:

$$\hat{R} = \sqrt{\frac{\text{var}(\theta|y)}{W}}$$

$\text{var}(\theta|y)$ is the pooled posterior variance, and W is the average within-chain variance. A value of $\hat{R}$ close to 1 indicates convergence and suggests that the multiple chains have adequately explored the parameter space and reached a stable posterior distribution. In contrast, if $\hat{R}$ significantly deviates from 1, it implies there may be issues with the model or sampling algorithm, or further sampling may be required.

Figure 43 presents the Gelman-Rubin statistic for the three strategies. The Entropic strategy presents a better agreement among the four chains. Although not subjected to modifications in the experiments, SF faced more convergence issues than $sfbet$, suggesting the interdependence of parameters and underscoring the significance of defining priors for Bayesian inference.

A.1.2 Autocorrelation Function

The autocorrelation function (ACF) plot is one of the most used diagnostic tools in Bayesian inference to assess its efficiency. The plot illustrates the correlation between a sample and its subsequent samples at different lags or steps. A quick drop in autocorrelation values as you move away from lag zero indicates efficient sampling, meaning the chain is exploring the parameter space well. Conversely, high and sustained autocorrelation suggests poor mixing, implying that the chain is moving slowly through the parameter space and might require more samples or even model reparameterization for reliable inference.

The autocorrelation is evaluated for each chain with a lag of 100 samples. In Figure 44, the ACF plot showcases four chains from the same experiment in a single column, each chain differentiated by color. Once again, the advantages of the Entropic strategy are visible. However, chain number 2 of the Entropic strategy displays values surpassing

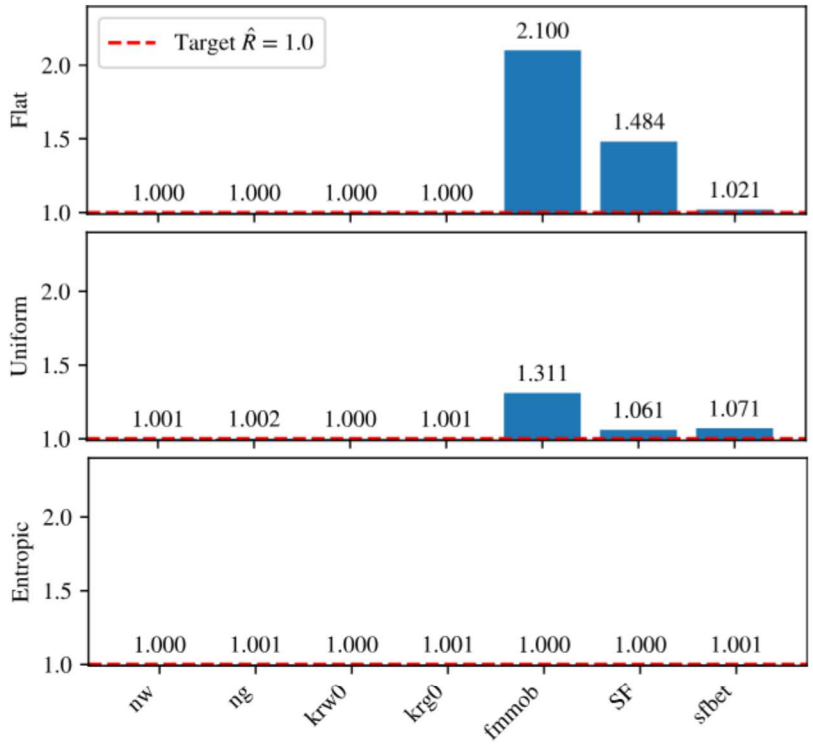

Figure 43 – The Gelman-Rubin statistics for each experiment of prior choices.

the 0.1 threshold for a lag of 100 samples, indicating potential problems with mixing, convergence, or efficiency in exploring the posterior distribution.

A.1.3 Divergent Transitions

Divergences, or divergent transitions, can be employed as a diagnostic tool to compare different choices of priors, as they indicate inadequate parameter adaptation in HMC. They occur when the trajectory deviates from the expected Hamiltonian path due to complex or steep posterior geometry (Betancourt, 2018; Gelman et al., 2021). Persistent or clustered divergences can signal problematic areas in the parameter space that require careful examination. Comparing divergence patterns for different priors offers a quantitative way to assess their impact on the Bayesian regression process (Betancourt and Girolami, 2013; Carpenter et al., 2017). Expanding the dataset in a well-defined Bayesian model can improve the estimation of the posterior distribution. Inadequate models may still show persistent divergences regardless of the size of the data.

The four chains' trace plots are displayed side by side, along with the corresponding distribution approach for each parameter in Figures 45, 46, and 47.

Table 16 presents the estimated values by the proposed approach for initial guesses, the set of distributions for the entropic priors experiment, and the uniform priors.

The results here suggest a huge potential in expanding the application of the maximum entropy principle to consider the knowledge of prior beliefs, more complex

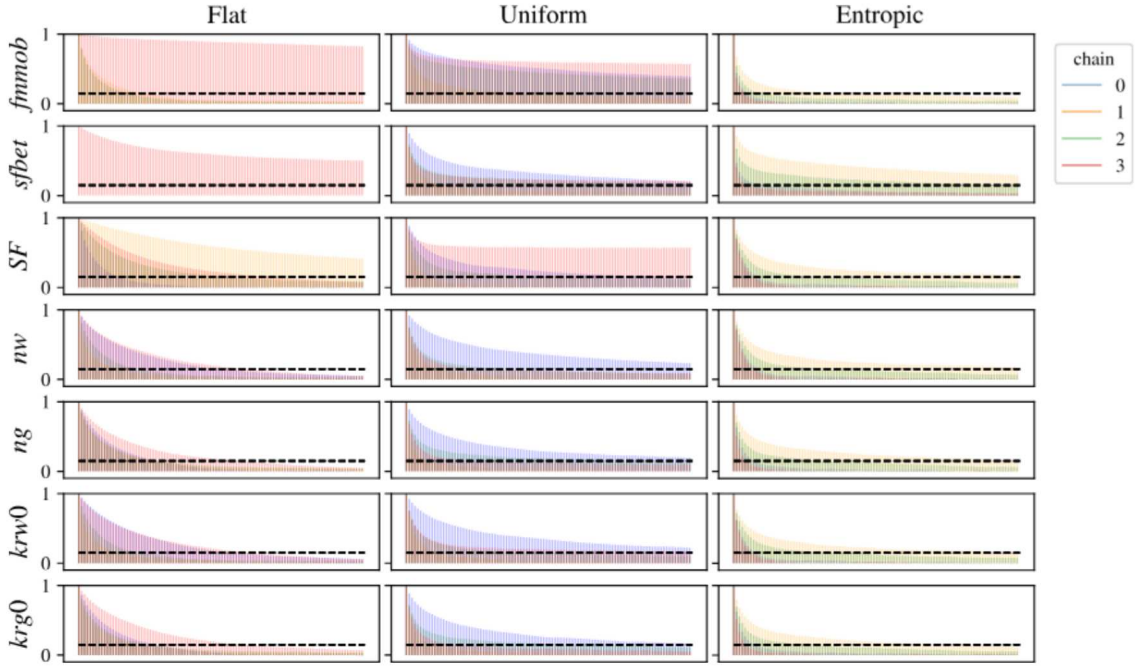

Figure 44 – Plots of autocorrelation function colored by chains, with a maximum lag of 100 samples. The threshold for acceptable autocorrelation is marked by the dashed horizontal line at 0.1.

Table 16 – Comparison of parameters median and standard deviation across different choices for the prior distributions.

		Median ± Standard Deviation		
	Real	**Flat**	**Uniform**	**Entropic**
fmmob	4.341×10^{3}	$(2.720 \pm \infty) \times 10^{17}$	$(6.834 \pm 2.690) \times 10^{5}$	$(4.481 \pm 0.266) \times 10^{3}$
sfbet	4.240×10^{2}	$(1.734 \pm \infty) \times 10^{306}$	$(2.625 \pm 1.680) \times 10^{2}$	$(2.687 \pm 0.917) \times 10^{2}$
SF	3.409×10^{-1}	$(3.321 \pm 2.22) \times 10^{-1}$	$(5.821 \pm 1.120) \times 10^{-1}$	$(3.328 \pm 0.102) \times 10^{-1}$
n_w	4.200×10^{0}	$(3.998 \pm 0.202) \times 10^{0}$	$(4.014 \pm 0.207) \times 10^{0}$	$(4.006 \pm 0.204) \times 10^{0}$
n_g	1.400×10^{0}	$(1.390 \pm 0.054) \times 10^{0}$	$(1.390 \pm 0.054) \times 10^{0}$	$(1.385 \pm 0.053) \times 10^{0}$
k^0_{rw}	5.000×10^{-1}	$(4.809 \pm 0.186) \times 10^{-1}$	$(4.818 \pm 0.192) \times 10^{-1}$	$(4.816 \pm 0.188) \times 10^{-1}$
k^0_{rg}	6.000×10^{-1}	$(5.839 \pm 0.13) \times 10^{-1}$	$(5.836 \pm 0.128) \times 10^{-1}$	$(5.831 \pm 0.127) \times 10^{-1}$

models, and systems, leveraging its honesty and objectivity.

A.2 Effects of Noise on Parameter Estimation

In the process of estimating parameters from a synthetic dataset, experiments reveal distinct outcomes in scenarios with and without noise. Without noise, the model demonstrates a high capability for precise parameter estimation, aligning closely with the ground truth. This is evidenced by accurately matching parameters described in Table 17. Conversely, introducing noise complicates the parameter estimation, leading to deviations from the ground truth despite achieving a statistically good fit between the simulated curve and noisy data. The following tables summarize the results from both experiments:

Notably, parameters n_w, n_g, k^0_{rw}, and k^0_{rg} exhibit slight deviations with reasonable accuracy, yet $fmmob$ and $sfbet$ show larger discrepancies and uncertainties. This

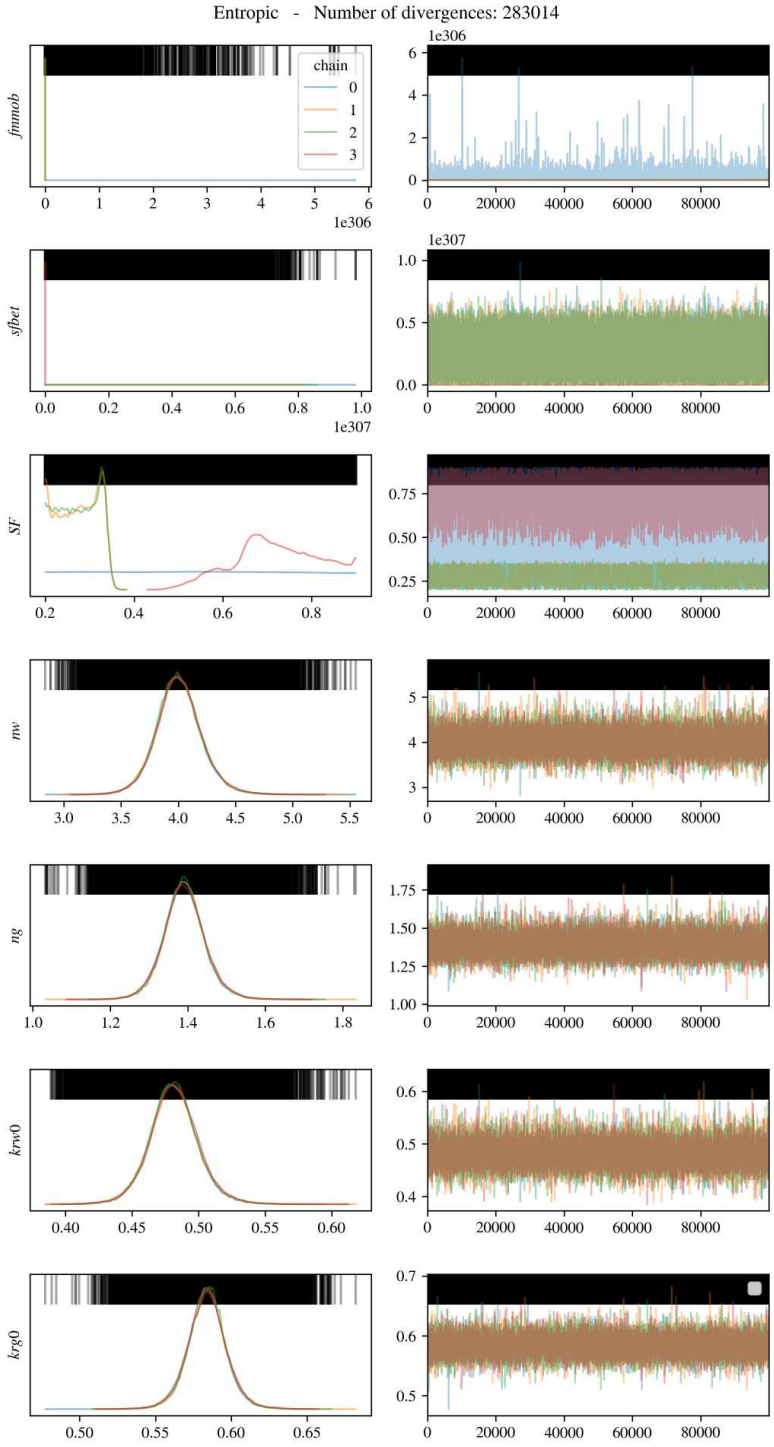

Figure 45 – Trace plot for Flat prior. Number of divergences: 283014

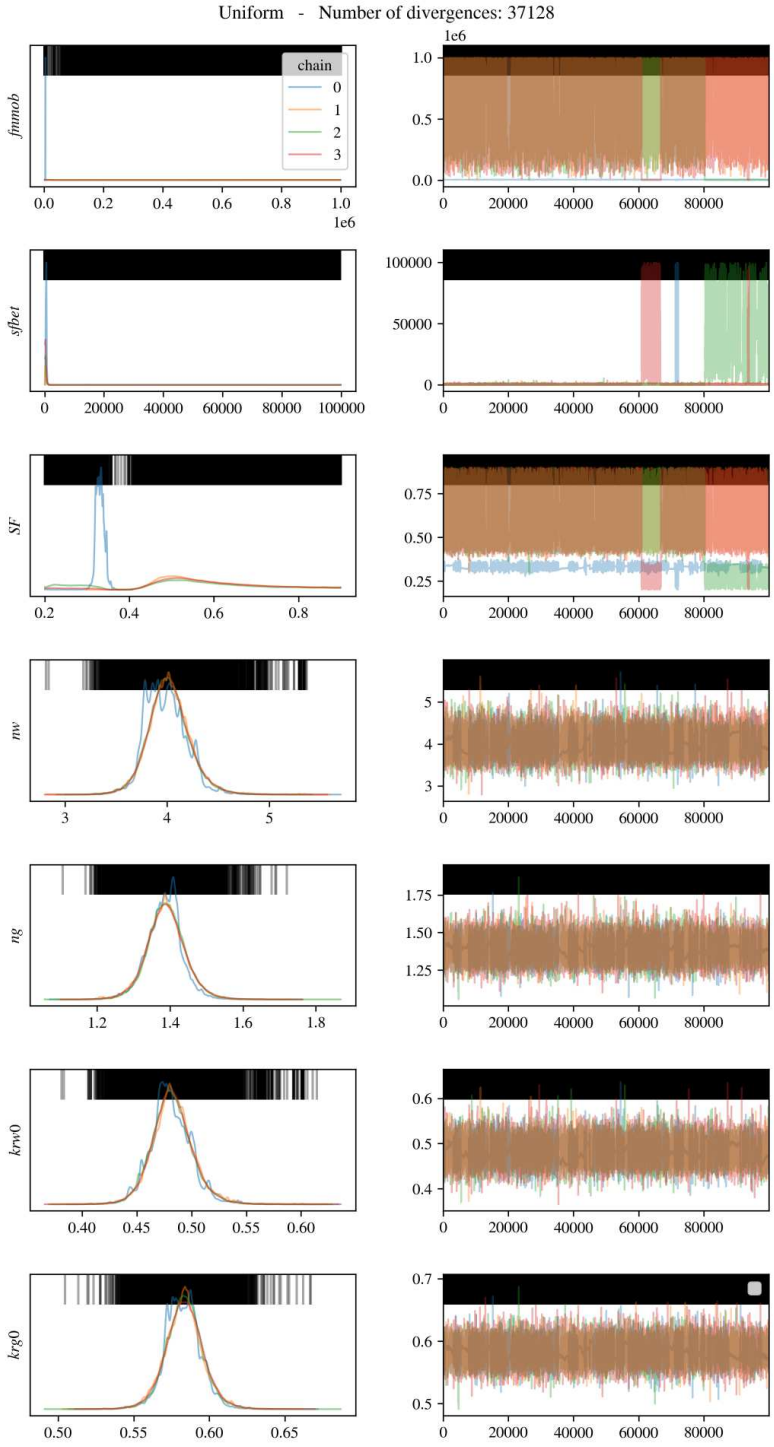

Figure 46 – Trace plot for Uniform prior. Number of divergences: 37128

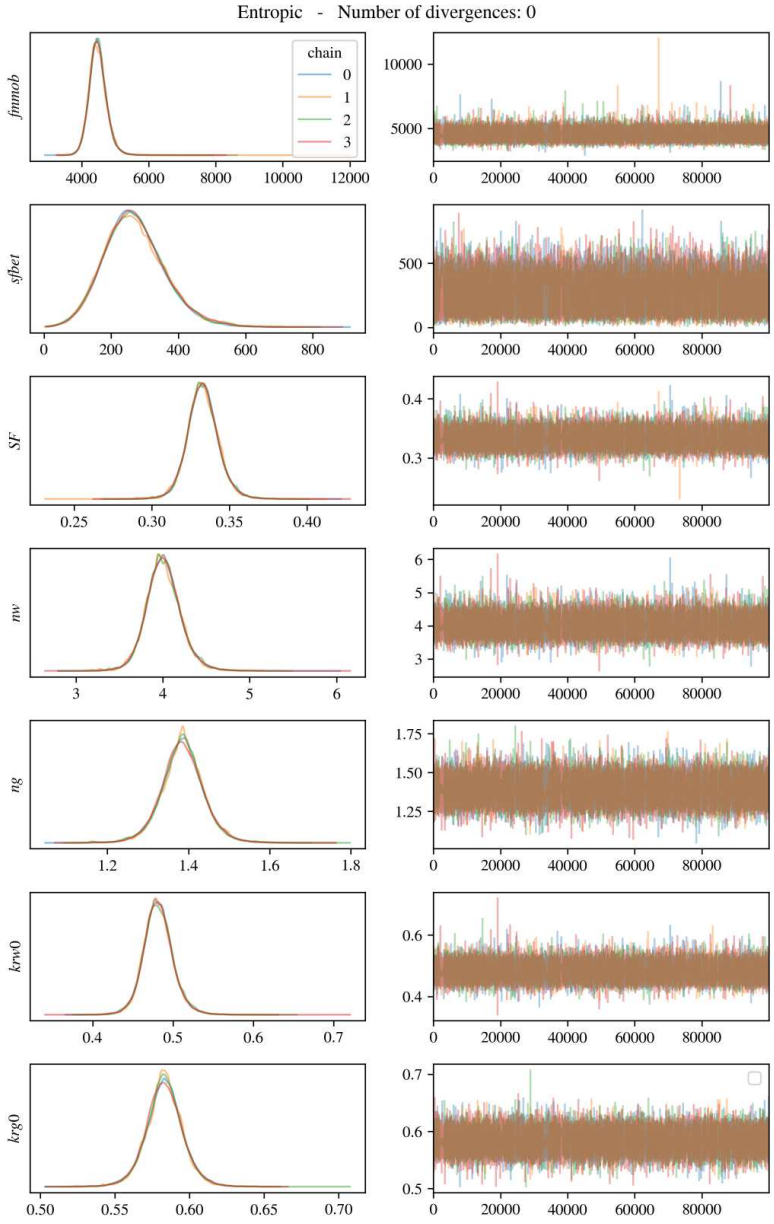

Figure 47 – Trace plot for Entropic prior. Number of divergences: 0

underscores the noise impact on the robustness of parameter estimation, leading to solutions that fit the observed data well but deviate from the actual ground truth. Significant correlation coefficients between parameters found during the optimization, such as $C(n_w, SF) = 0.9862$, $C(n_w, k^0_{rw}) = 0.8316$, $C(k^0_{rw}, SF) = 0.7815$ and $C(n_g, k^0_{rg}) = 0.7567$, indicate interdependencies among parameters, influencing the model's sensitivity to noise and affecting the precision of parameter recovery. Figure 48 compares the optimization runs with and without noise, highlighting the effects of noise in the fitting process.

Table 17 – Comparison between experiments

Parameter	**Ground Truth**	**Fitting Results**	
		w/o noise	**w/ noise**
$fmmob$	4341	4339.821	4670.670 ± 637.715 (**13.65%**)
$sfbet$	424	424.2472	306.7279 ± 166.941 (**54.43%**)
SF	0.3409	0.340924	0.332246 ± 0.00771 (2.32%)
n_w	4.200	4.199071	3.986546 ± 0.15234 (3.82%)
n_g	1.400	1.400099	1.386151 ± 0.04276 (3.08%)
k^0_{rw}	0.5	0.499938	0.480179 ± 0.01401 (2.92%)
k^0_{rg}	0.6	0.600026	0.583317 ± 0.01021 (1.75%)

(a) Optimization with no noise.

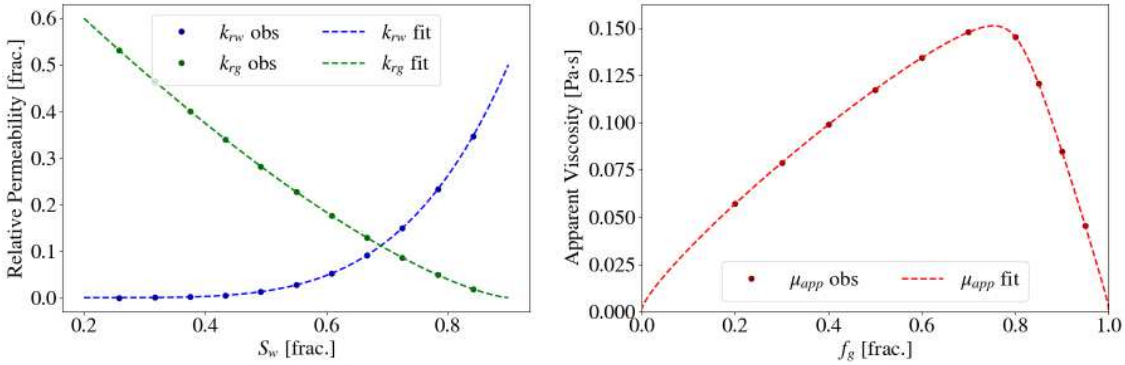

(b) Optimization with noise.

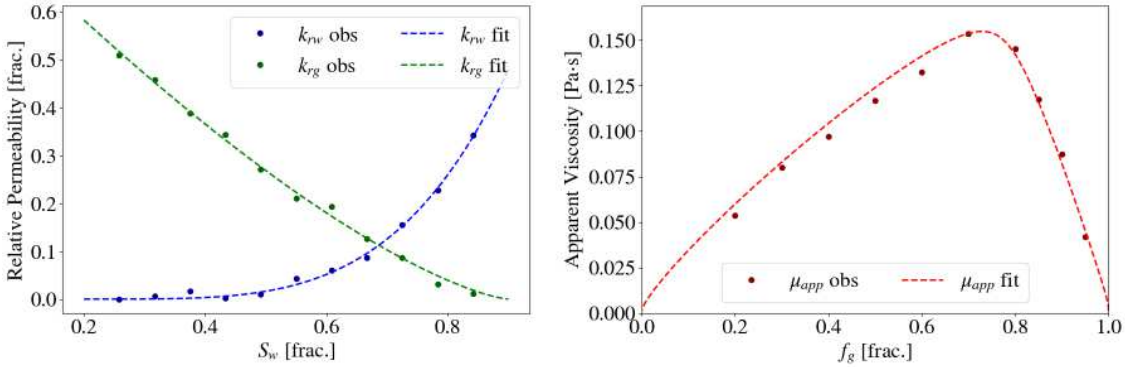

Figure 48 – Comparative optimization results.

A.3 Case Studies

To deepen the analysis of model response via the sensitivity analysis, three case studies with steady-state data from the literature will be evaluated. Datasets for a water-wet case based on Chabert et al. (2012), a gas-wet case based on the Moradi-Araghi et al. (1997), and a mixed-wet case Ma et al. (2013) will be generated considering the real steady-state dataset of foam strength vs. foam quality and its respective relative permeability based on the models presented in Boeije and Rossen (2013).

A.3.1 Water-wet Case

The image shown in Figure 49 supports some of the findings discussed in Section 3 of the manuscript. Specifically, in the low-quality regime, the parameter $fmmob$ rules the sensitivity of the apparent viscosity, while in the high-quality regime, the parameter SF remains one of the most important. However, the parameter n_w does not contribute significantly to the variance response, and its interactions with SF are less important. However, it is important to note that there is a high degree of uncertainty in the sharpness of the transition between the two regimes. This indicates that the parameter $sfbet$ has a distribution with a not well-defined mean value, confirmed in Figure 50, which is reflected in the sensitivity analysis as one of the most influential parameters for this particular case.

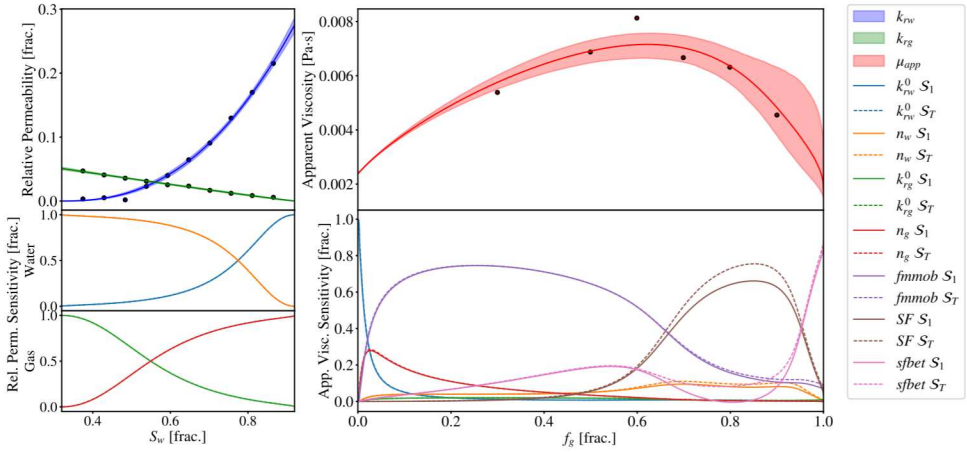

Figure 49 – Propagated uncertainties and Sobol analysis for relative permeability and implicit texture of foam models Chabert et al. (2012) dataset.

Figure 50 shows that the correlation between n_w and SF is not as strong as the synthetic case. It is important to remark that the uncertainties will be greater due to the size of this dataset.

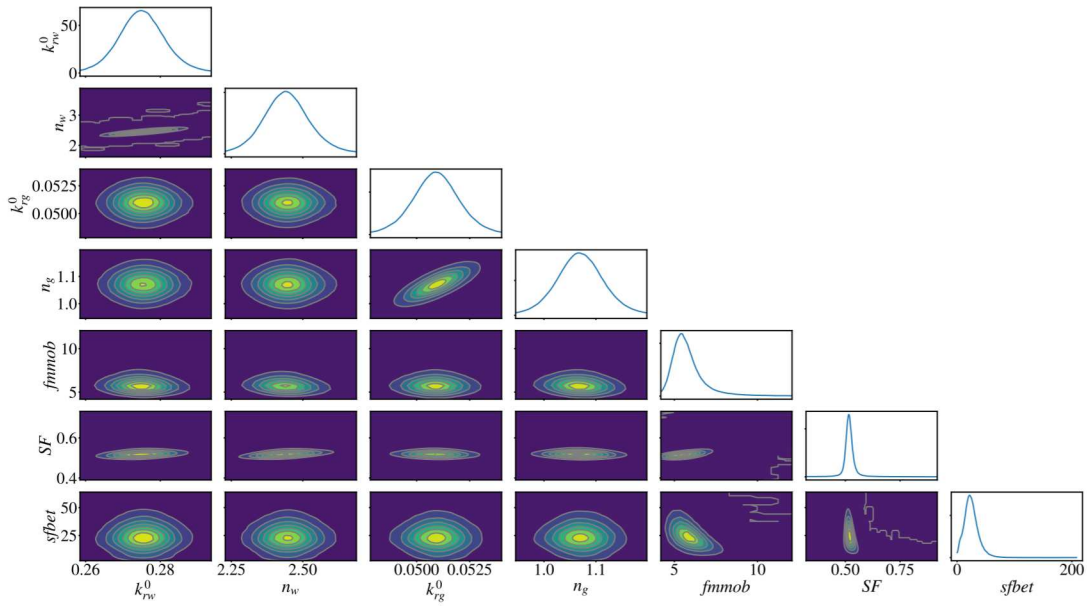

Figure 50 – Joint distribution and correlations analysis for Chabert et al. (2012) dataset.

A.3.2 Gas-wet Case

The sensitivity of the parameters studied is confirmed once again, but now effects from the gas relative permeability parameters, n_g and k^0_{rg} are more notable along the entire low-quality region in Figure 51. The wider range of values for both n_g and k^0_{rg} found in Figure 52 can influence this contribution.

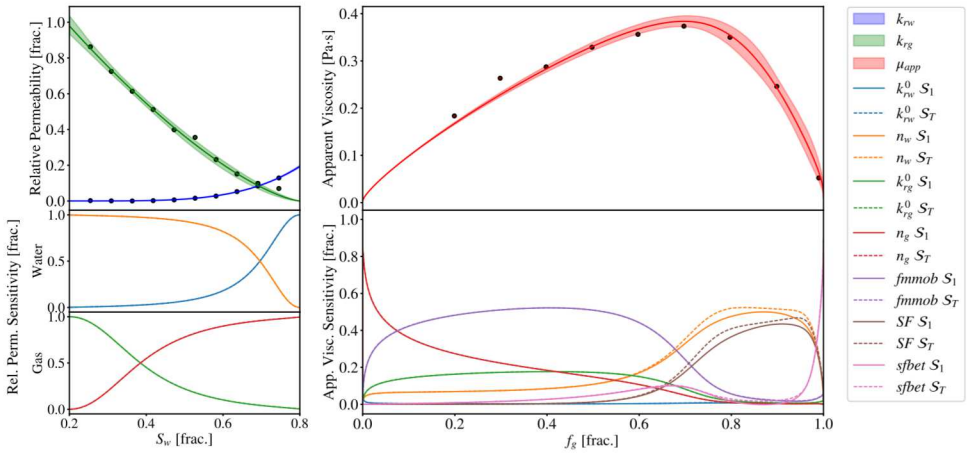

Figure 51 – Propagated uncertainties and Sobol analysis for relative permeability and implicit texture of foam models for Moradi-Araghi et al. (1997) dataset.

A.3.3 Mixed-wet Case

The last experiment shows results similar to those of the synthetic dataset in the paper, with a mixed-wet behavior. Although Figure 53 exhibits an earlier transition between regimes, $fmmob$ still drives variations in low-quality regimes, while SF and n_w interactions govern high-quality. As the transition between regimes is more abrupt,

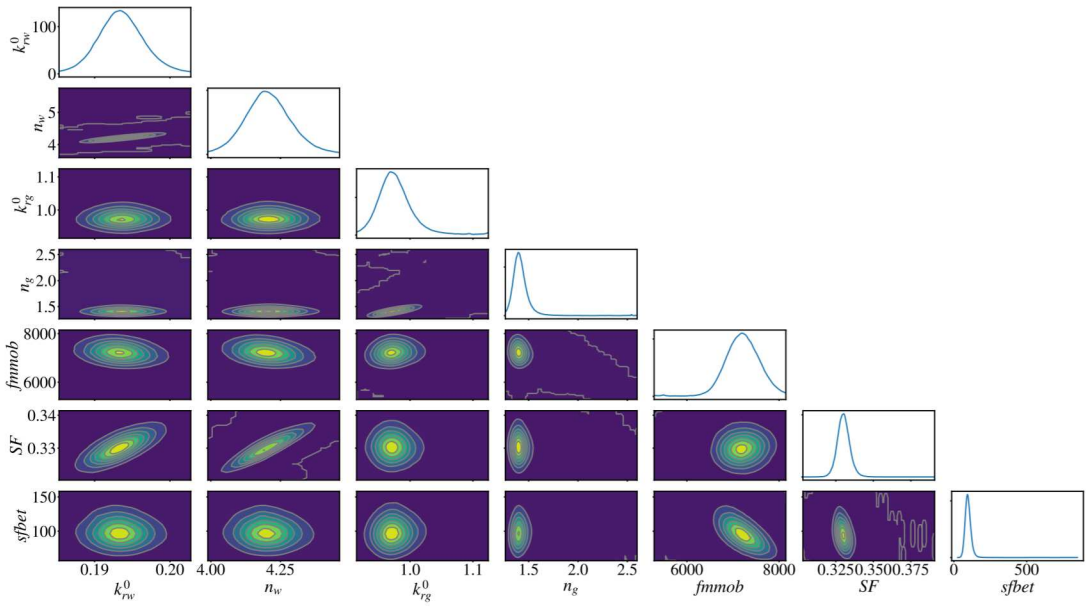

Figure 52 – Joint distribution and correlation analysis for Moradi-Araghi et al. (1997) dataset.

so are the changes in the most influential parameters. Also, as the dataset contains a larger number of foam quality responses, many of which are in the high-quality range, the estimations shown in Figure 54 are more well-defined than in the other two studied cases.

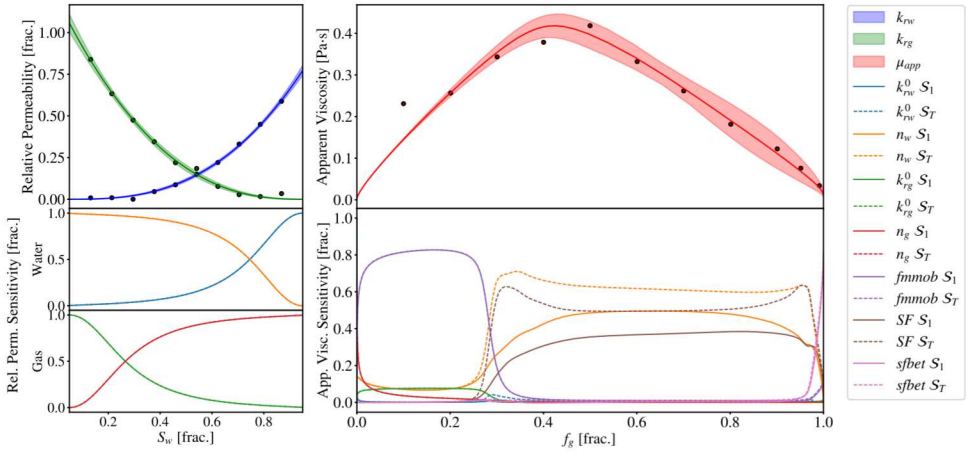

Figure 53 – Propagated uncertainties and Sobol analysis for relative permeability and implicit texture of foam models for Ma et al. (2013) dataset.

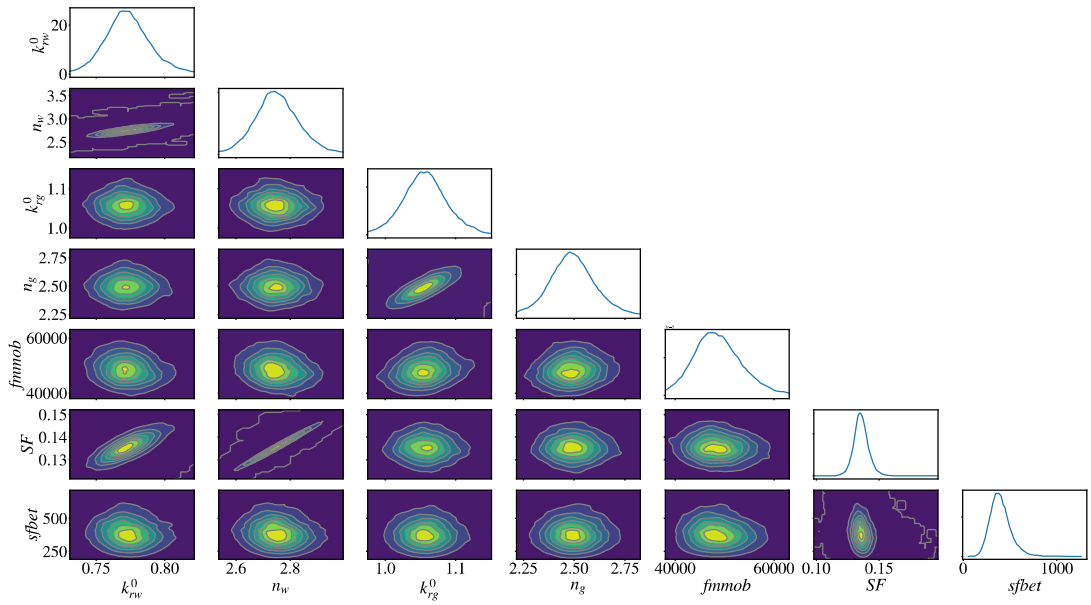

Figure 54 – Joint distribution and correlation analysis for Ma et al. (2013) dataset.

APPENDIX B – Supplementary Information for Chapter 4

B.1 Water and Oil Saturations

A key step in estimating foam parameters from solely foam quality scan data (f_g, μ_{app}) is determining the corresponding phase saturations. We generalize the established method for two-phase (water-gas) flow, which relies on Brooks-Corey relations (Farajzadeh et al., 2015c; Eftekhari and Farajzadeh, 2017; Ribeiro et al., 2024), to the three-phase case at a fixed oil-water injection ratio (u_o/u_w). This extension allows for the direct estimation of steady-state water and oil saturations from the experimental observables, as follows:

$$S_w = \left(\frac{\mu_w}{k_{rw}^0 \mu_{app}} \frac{1 - f_g}{1 + \frac{u_o}{u_w}} \right)^{\frac{1}{n_w}} (1 - S_{wc} - S_{or} - S_{gr}) + S_{wc}, \tag{B.1}$$

$$S_o = \left(\frac{\mu_o}{k_{ro}^0 \mu_{app}} \frac{1 - f_g}{1 + \frac{u_w}{u_o}} \right)^{\frac{1}{n_o}} (1 - S_{wc} - S_{or} - S_{gr}) + S_{or}. \tag{B.2}$$

B.2 Deterministic Calibration

Deterministic optimization methods that yield a single best-fit parameter set can mask significant mismatches, particularly when applied to sparse experimental data. To illustrate this issue, we investigate the full and scarce datasets presented in Figure 12 using the differential evolution (DE) method (Storn and Price, 1997).

Figure 55 shows the fitting results obtained with the full and scarce datasets. For the full dataset, a good agreement with the ground truth is observed, whereas for the scarce dataset, the estimated F_{oil} response deviates significantly. This behavior is also observed when using Bayesian inference methods. However, an additional advantage of the latter is the ability to estimate the posterior distributions of the parameters (see Figures 6, 7, and 12), which enables a more rigorous assessment of uncertainty. This, in turn, supports the evaluation of the fitting quality through the parameters' posterior distributions and the propagation of uncertainties to the simulation outputs.

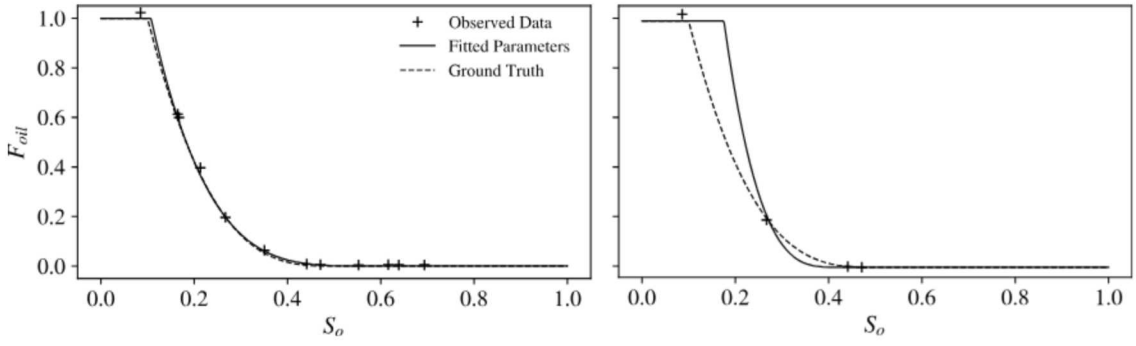

Figure 55 – Deterministic fitting for the full (left) and scarce (right) datasets.

B.3 Parameter Calibration Robustness

This appendix assesses the robustness of the parameter estimation methodology against increased measurement noise. We also analyze the impact of different prior distributions and a model simplification to address parameter identifiability challenges that emerge under high-noise conditions.

B.3.1 Sensitivity to Noise

We evaluated the parameter estimation performance with measurement noise increased from the 2% baseline (main text, Figures 6 and 7) to 5% and 10%.

The results for the addition of 5% noise are shown in Figure 56. The right panel presents the posterior distributions, where the increase in uncertainty is almost negligible. The left panel displays the fitted curve for the F_{oil} function, which begins to deviate from the ground truth.

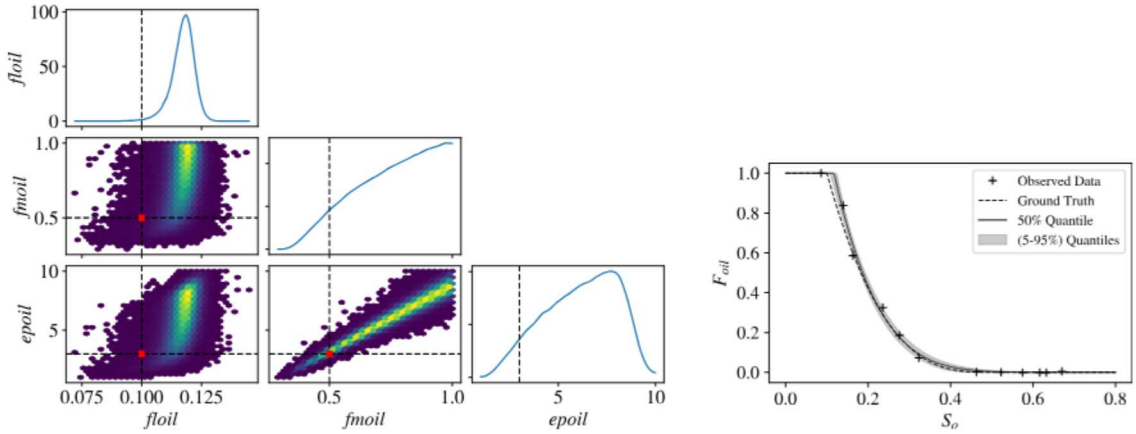

Figure 56 – Parameter posterior distributions (left) and F_{oil} function estimation (right) with 5% measurement noise.

Further increasing the noise level to 10% degrades the recovery of both the ground truth parameters and the F_{oil} function, as shown in Figure 57. The results also show that the posterior distribution of *epoil* becomes truncated at its upper bound, suggesting that the uniform prior is overly restrictive in this case.

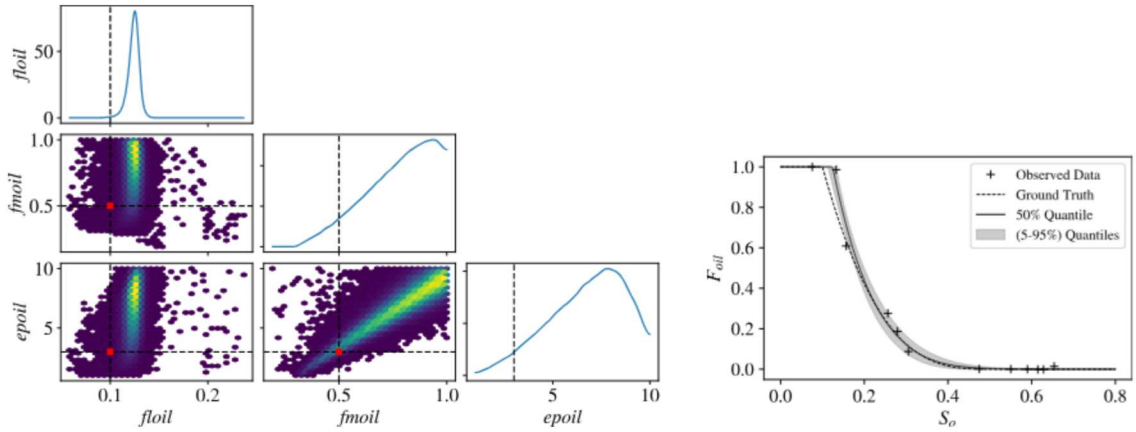

Figure 57 – Parameter posterior distributions (left) and F_{oil} function estimation (right) with 10% measurement noise.

B.3.2 Prior Distribution Comparison

The choice of prior distributions can influence parameter estimation, particularly when data is limited. This interval definition is clear for the parameters defining oil saturation thresholds *floil* and *fmoil*. However, it is not true for the exponent *epoil*. While our original choice sought to illustrate a typical box-constrained search space used in optimization procedures with a sufficiently broad range, this may not be well-constrained for *epoil* that may assume any positive real numbers.

To address the identifiability issues observed at 10% noise, we explore two alternative prior distributions for the exponent parameter *epoil*, while keeping the same physically based uniform priors for *floil* and *fmoil*. The following choices were explored:

1. A wider uniform prior, $epoil \sim \mathcal{U}(10^{-3}, 50)$, to have a less informative specification.
2. An exponential prior, $epoil \sim \text{Exp}(\lambda = 1)$, which assigns higher probability to smaller values but does not impose a strict upper bound (see de Miranda et al. (2024) for more details about this choice for prior distribution).

The wider uniform prior resolves the boundary truncation issue (reported in Fig. 57), as the posterior for *epoil* concentrates well below the new upper limit of 20 (Figure 58). However, the posterior distributions obtained in this case are even less precise, especially for *fmoil* and *epoil*.

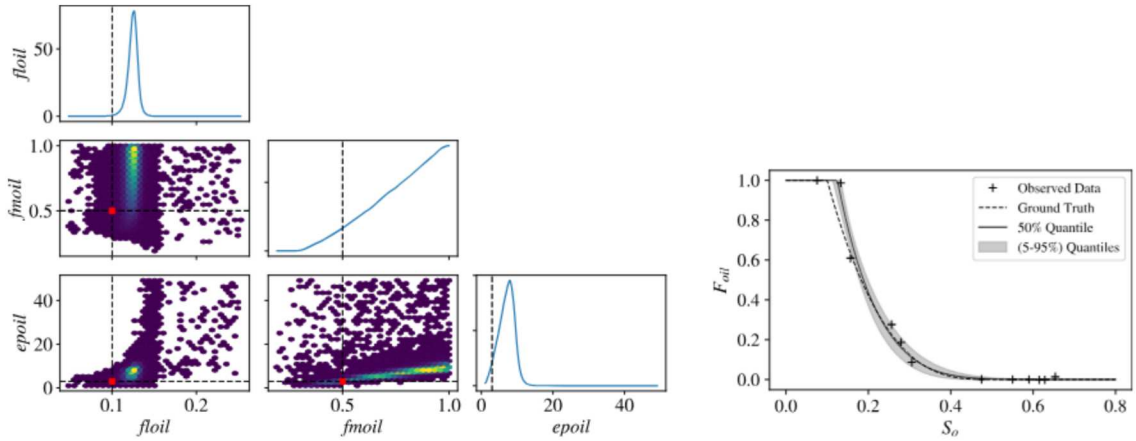

Figure 58 – Parameter posterior distributions (left) and F_{oil} function estimation (right) with 10% measurement noise and and an extended uniform prior for *epoil* up to 50.

In contrast, the results for the exponential prior for *epoil* significantly improve parameter identifiability (Figure 59). The posterior correlation is visibly reduced, and the posterior mode for *fmoil* aligns closely with the ground-truth value. This improvement occurs despite the modification being applied only to the prior for *epoil*. The propagated uncertainty in the estimated F_{oil} function remains comparable to the uniform prior case.

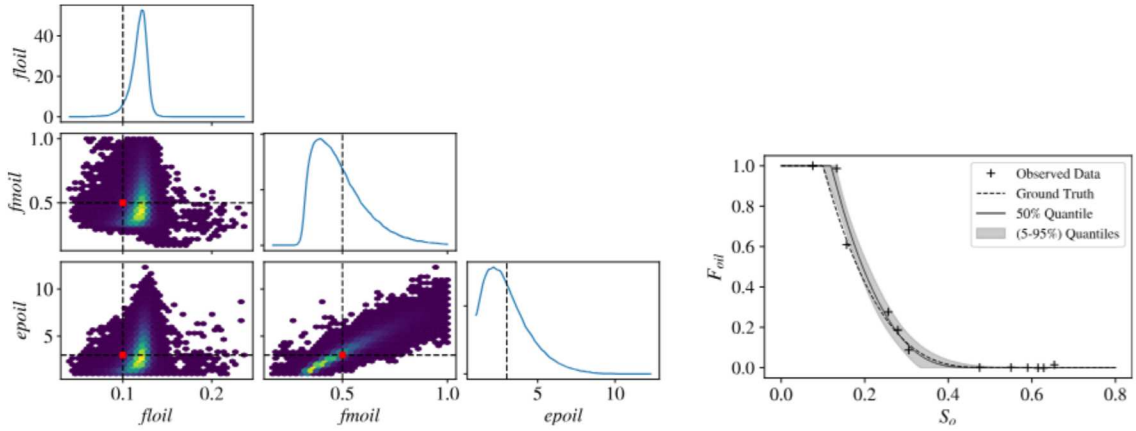

Figure 59 – Parameter posterior distributions (left) and F_{oil} function estimation (right) with 10% measurement noise and exponential prior for *epoil*.

B.3.3 Model Simplification

A core physical assumption of our model is that oil affects foam only at saturations exceeding its residual value (S_{or}). This premise provides direct physical motivation for a model simplification: setting the parameter $floil = S_{or}$. Driven by this, and by the persistent correlation between *fmoil* and *epoil* observed in all cases, a final test was conducted. We evaluated this simplified model under the high-noise scenario using both the uniform and exponential priors.

With a uniform prior for *epoil*, the simplified model's posteriors (Figure 60) align better with the ground-truth. Nevertheless, the distributions of the remaining parameters

are wider, and the correlation between them does not decrease significantly. This results in greater propagated uncertainty to the F_{oil} function for oil saturations near *fmoil*, despite lower near *floil*.

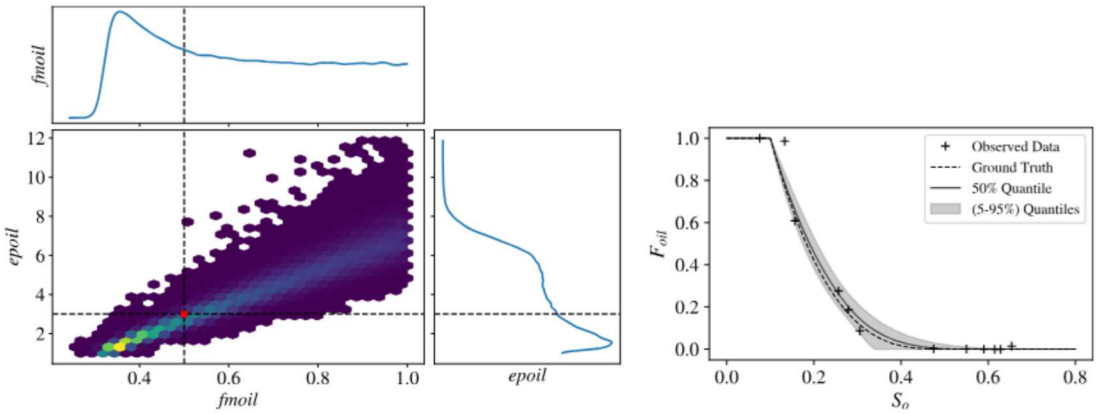

Figure 60 – Parameter posterior distributions (left) and F_{oil} function estimation (right) with 10% measurement noise and exponential prior for *epoil*.

Finally, we evaluate the exponential prior in the simplified model using the exponential prior. Figure 61 (left) shows similar results compared to Figure 59

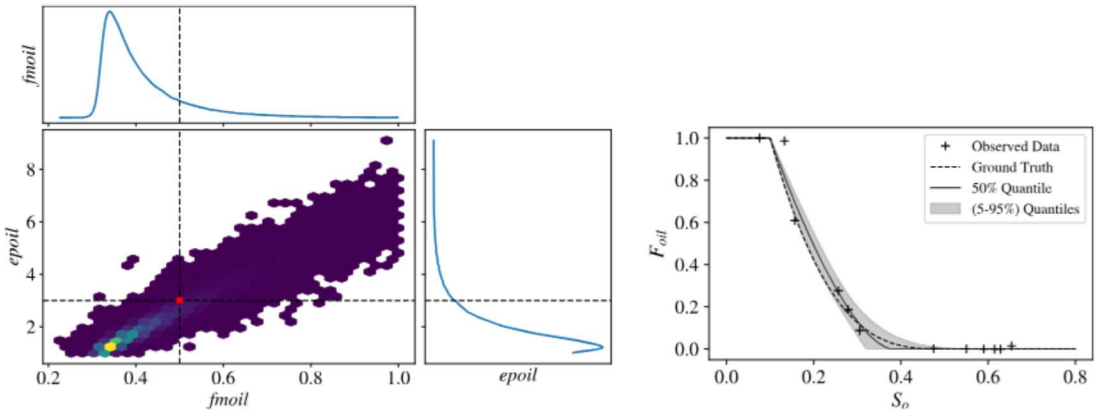

Figure 61 – Parameter posterior distributions (left) and F_{oil} function estimation (right) with 10% measurement noise and exponential prior for *epoil*.

While the constraint $floil = S_{or}$ provides a physically motivated simplification that improves the mathematical conditioning of the inverse problem, the persistent correlation between *fmoil* and *epoil* across all evaluated cases is symptomatic of a structural dependency. This dependency, analogous to collinearity, prevents the data from cleanly distinguishing the individual effects of these two parameters on the model output (McElreath, 2020).

B.3.4 Modified synthetic dataset with a lower *fmoil*

We present additional numerical simulations conducted with a modified oil-related foam parameter $fmoil = 0.3$ (Case 1 from Lyu et al. (2021b)) instead of $fmoil = 0.5$ used

in the main text (Case 2 from Lyu et al. (2021b)). This lower value of *fmoil* represents a case where foam destruction occurs at lower oil saturations, making the system more sensitive to the presence of oil.

The simulations follow the same methodology described in the main text, with all fluid properties and parameters remaining identical except for the modified value of *fmoil*. The computational domain, numerical implementation, and simulation conditions are maintained as described in the main text.

As in the main paper, we employed the same injection protocol with fixed gas fraction $f_g^* = 0.3$ (determined from the foam quality scan) while progressively increasing the oil-water ratio u_o/u_w. Figure 62 illustrates the pressure drop evolution during this procedure and the steady-state values of apparent viscosity as a function of oil fraction. Notice that in this setup, reaching the steady-state configuration may take a much longer time, especially for

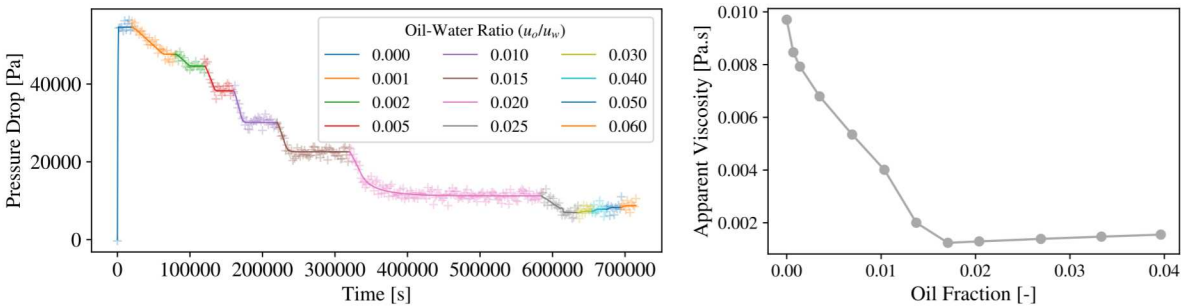

Figure 62 – Simulated pressure drops (left) and steady-state apparent viscosity (right) with increasing oil injection at fixed gas fraction $f_g = 0.3$.

Figure 63 presents the average saturation levels for each phase during the simulation. The results show that the transition from foam-dominated flow to oil-dominated flow occurs at lower oil saturations, consistent with the reduced *fmoil* value. The critical threshold where foam effectiveness begins to diminish is reached significantly earlier in the injection sequence.

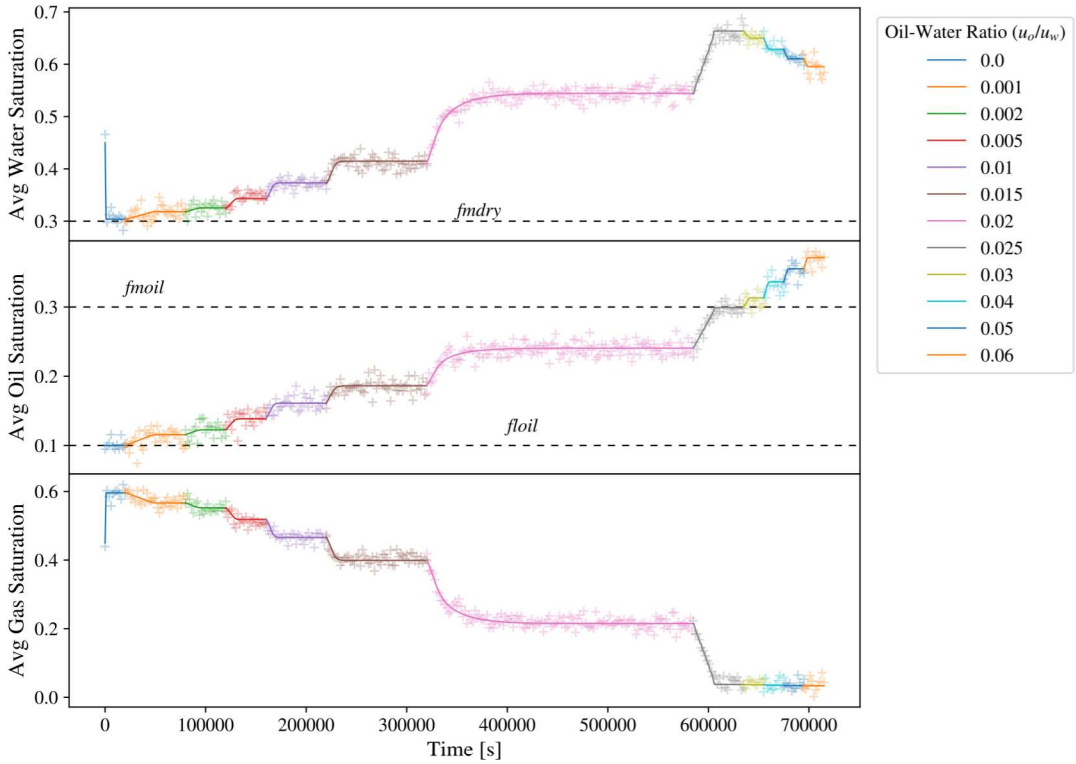

Figure 63 – Simulated saturations with increasing oil injection at $f_g = 0.3$.

Figure 64 illustrates the posterior distribution derived from the Bayesian inference process, along with the associated uncertainties and observed data points. There is a clear agreement with the ground truth, accompanied by minimal propagated uncertainty. This improvement can be attributed to the fact that the modified case provided more representative data points for the F_{oil} curve with low levels of added noise. Consequently, this results in virtually no identifiability issues regarding the F_{oil} function.

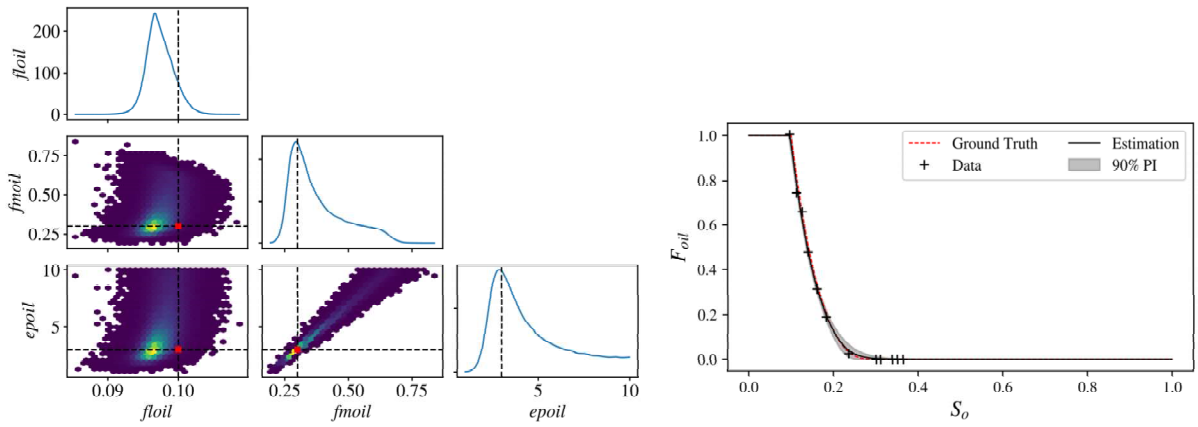

Figure 64 – Left: Posterior probability distributions and estimation of the F_{oil} obtained through Bayesian inference. Right: Propagated uncertainties to the F_{oil} function.

The additional results show a higher sensitivity to increases in oil fraction with $fmoil = 0.3$, where small increases in the oil-water ratio significantly reduce foam effec-